SPECTRAL CHARACTERIZATION AND REDUCED-ORDER MODELING OF INDUSTRIAL SHOT PEENING

by

Langdon Feltner

A Dissertation

Submitted to the Faculty of Purdue University

In Partial Fulfillment of the Requirements for the degree of

Doctor of Philosophy

School of Materials Engineering

West Lafayette, Indiana

December 2025

THE PURDUE UNIVERSITY GRADUATE SCHOOL
STATEMENT OF COMMITTEE APPROVAL

Dr. Paul Mort, Chair

School of Materials Engineering

Dr. David Bahr

School of Materials Engineering

Dr. David Johnson

School of Materials Engineering

Dr. Michael Titus

School of Materials Engineering

Approved by:

Dr. Bryan Huey

To my family, my friends, Paul Mort, Jack Champaigne, Sushrut Karmarkar, and Alexis Bullock. Thank you for your unfaltering belief.

ACKNOWLEDGMENTS

I would like to express my gratitude to Mark Gruninger and the Purdue University School of Materials Engineering's Center for Surface Engineering and Enhancement for their persistent support. I am especially thankful to Bryan Chevrie, Erik Waelchli, and Taylor Bowman of Electronics Inc., as well as Cory Padfield and Jennifer Brown of American Axle & Manufacturing, for their contributions to this work. I am grateful to Brian Lester, Kevin Long, and the entire Materials and Failure Modeling group at Sandia National Laboratories for their guidance and influence. Finally, I would like to thank my lab mates over the years—Kayli Henry, Line Koleiat, Rajeshree Varma, and Donovan Stumpf—for their friendship, support, and mentorship.

TABLE OF CONTENTS

LIST OF TABLES

LIST OF FIGURES

ABSTRACT

We develop a unified framework for understanding and predicting the heterogeneous residual stress fields that emerge from stochastic surface processes, with shot peening serving as a representative system. Although peening has long been recognized for its ability to enhance fatigue performance through near-surface compressive stresses, the underlying stress fields are spatially complex—shaped by random impact sequences, evolving media morphology, and nonlinear material response.

The spectral fabric of residual stress fields is investigated using Eshelby-like inclusions as a reduced-order mechanical basis. Finite element simulations reveal nonlinear overlap effects at increasing impact coverage, which are captured through a power spectral density ratio (PSDR) filter. The PSDR not only reconciles analytical and numerical models but also serves as a statistical descriptor of long-range coherence and local heterogeneity in stochastic stress fields.

High-resolution optical profilometry of peened Almen strips is used to extract three-dimensional surface topographies, from which spatial power spectral densities (PSDs) are computed. These spectra exhibit frequency-dependent amplification and systematic peak shifts with increasing impact velocity and coverage. A normalized PSD metric isolates the most process-sensitive frequency bands, demonstrating that spectral descriptors capture physically meaningful structure beyond conventional scalar roughness parameters.

These insights are integrated into a neural network enabled flowsheet for shot peening. A three-mode degradation model tracks the evolution of media size and shape under repeated recirculation, while a convolutional long short-term memory (ConvLSTM) neural network–trained on finite element data–predicts the evolving residual stress field in real time. This hybrid model enables mechanistically grounded, data-efficient prediction of process outcomes under realistic industrial conditions.

Together, these contributions link analytical elasticity theory, experimental metrology, and data-driven process modeling using statistical frameworks. This approach emphasizes interpretability, showing that even highly stochastic surface processes can be described through reproducible spectral metrics and reduced-order physical models. In doing so, the work pro-

vides a transferable foundation for modeling and monitoring surface treatments where spatial heterogeneity governs performance.

1. Introduction

1.1 Project Background

Purdue University's School of Materials Engineering houses the *Center for Surface Engineering and Enhancement* (CSEE), an industrial consortium consisting of thirteen member companies. Led by Managing Director Mark Gruninger, CSEE serves as Purdue's primary interface between academia and industry in the surface finishing sector, addressing grand challenges in manufacturing and advancing technologies across all levels of technical maturity.

Shot peening is a mechanical surface treatment in which metallic components are bombarded with steel or ceramic media, producing near-surface plastic deformation that induces compressive residual stresses and enhances the fatigue life of structural parts. Owing to this property, shot peening is a critical process within the aerospace and automotive industries. The CSEE community includes a diverse group of companies representing multiple roles

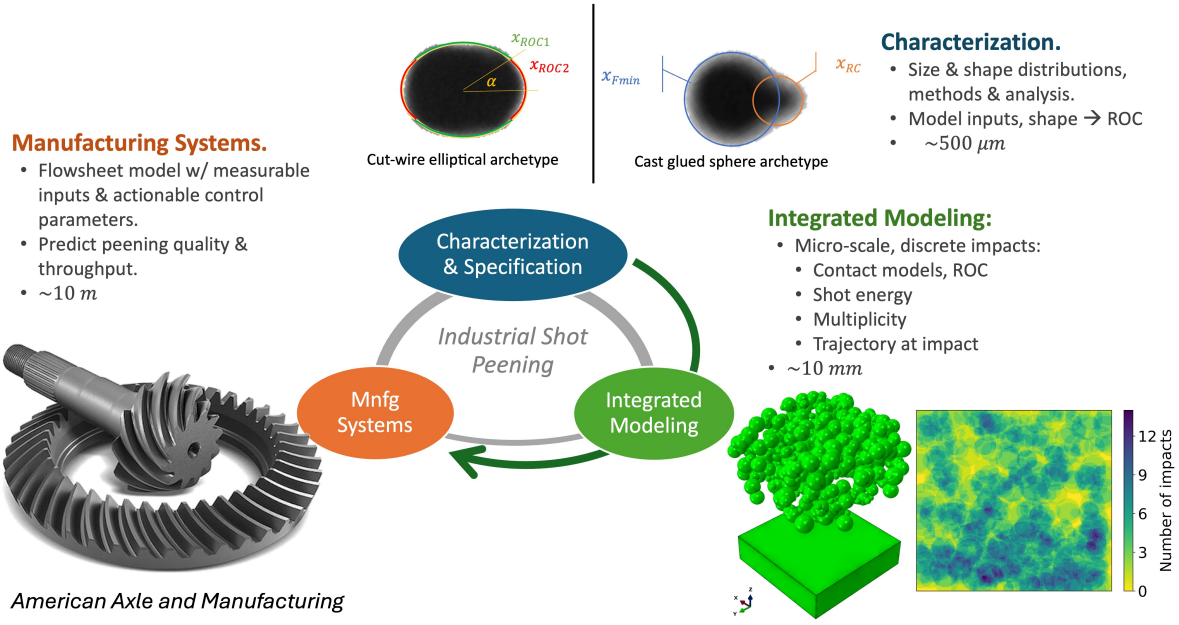

Figure 1.1. Overview of Project 1: integration of media characterization, process modeling, and component-scale simulation to bridge the scale gap between individual shot impacts and full part performance.

within the peening ecosystem, including end users (American Axle & Manufacturing, GE Aerospace, Cummins, Rolls-Royce), machine manufacturers (Engineered Abrasives, Progressive Surface, Sinto America), sensor and process-control developers (Electronics Inc.), and process consumables suppliers (Toyo Seiko North America).

This dissertation is largely the product of two CSEE-funded research projects on industrial shot peening. The first, summarized in Figure 1.1, aimed to connect the characterization and specification of shot peening media to systems-level process stability through an integrated modeling framework that bridges the scale gap between individual shot particles (~ 600 μm) and full-size components.

That project resulted in the development of a process flowsheet for industrial shot peening. The model connects media degradation and recharge dynamics to residual stress field evolution in a reduced-order form suitable for process optimization studies, as detailed in Chapters 5 and 6. Concurrently, Purdue University–through CSEE and the Manufacturing and Materials Research Laboratories (MMRL)–invested in a state-of-the-art experimental facility for shot peening research.

The facility includes the following key systems:

- **ProcessMaster:** laboratory-scale shot peening test stand (sentenso GmbH)
- **Solidsizer:** dynamic image analysis system for media morphology (J.M. Canty Inc.)
- **iXRD Mini:** residual stress measurement system (Proto Manufacturing)
- **VR-6000 Series:** optical profilometer for surface topography (Keyence Corporation)
- **Robotic Shot Peening Unit:** production-scale system for component-level studies (Progressive Surface)

As a result of the momentum established by the first project, CSEE awarded a project extension, summarized in Figure 1.2. The goal of this extension was to build upon the foundation established in the first phase, advancing two complementary pillars: *modeling* and *validation*.

The **modeling pillar** aimed to extend the flexibility of the flowsheet and integrated models to a broader range of material systems, guided by collaborations with CSEE member

companies. In addition, the modeling work sought to capture impact sequencing and the temporal evolution of both residual stress field structure and surface integrity– addressed in Chapters 2 and 3, respectively.

The **validation pillar** focused on leveraging the expanded experimental facilities to perform high-resolution validation of stress fields and surface finishes. This pillar was intentionally forward-looking, designed to establish the groundwork for future research in autonomous process control (i.e., digital twin modeling) enabled by advanced sensing technologies. Optical profilometry serves as the foundation for quantifying the temporal evolution of sub-impact-scale deformations, as discussed in Chapter 4.

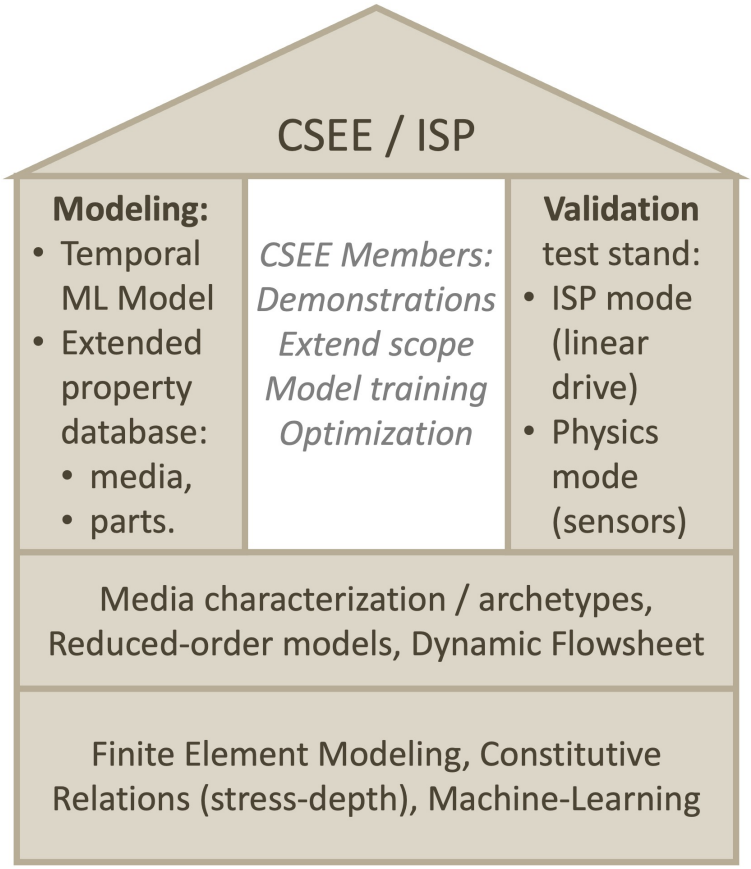

Figure 1.2. Overview of Project 2: dual-pillar framework extending the first project through enhanced modeling and experimental validation, forming the basis for future autonomous control and digital twin development.

1.2 Dissertation Motivation

Although the macroscopic benefits of peening have been recognized for decades, the physical mechanisms by which thousands of discrete impacts interact to produce a global residual stress field remain incompletely understood. This difficulty stems from the inherently stochastic nature of peening. Each particle impact differs in velocity, incidence angle, and local contact geometry. Even under tightly controlled process conditions, superposition of impacts generates heterogeneous stress fields that elude conventional deterministic descriptions.

The goal of this dissertation is to understand stochasticity in shot peening processes. This ranges from lot-to-lot variability in component performance driven by media recharge cycles to localized fluctuations in residual stress fields and surface topography. The central hypothesis is that the apparent complexity of these stress fields reflects a quantifiable fabric–a structured form of variability governed by contact mechanics and the statistical distribution of random impacts. To realize a general modeling architecture, the research is organized around the following specific objectives:

1. **Formulate and characterize the stochastic foundations of shot peening through spectral methods.** Develop analytical, numerical, and experimental frameworks that describe how random impact statistics give rise to spatially heterogeneous residual stress and surface topography. Use Poisson coverage theory, Eshelby-based mechanics, and Fourier-domain spectral analysis of optical profilometry data to reveal the structured variability, or spectral fabric, that governs stochastic deformation.

2. **Develop a flowsheet-based digital twin for stochastic surface processes.** Construct a modular process framework that integrates analytical models, finite-element simulations, and neural-network surrogates with experimentally derived media descriptors from dynamic image analysis (DIA). The resulting architecture predicts process-dependent residual stress evolution, incorporates stochastic variability, and enables scenario testing for industrial shot peening operations.

Collectively, these two threads connect the physics of stochastic surface deformation with data-driven process modeling, establishing a unified framework that links spectral mechanics and digital manufacturing.

1.3 Organization of the Dissertation

This dissertation is organized in a publication-based format and consists of five manuscripts, each presented as a standalone chapter, followed by an integrative conclusion. While each chapter includes the standard scientific sections (e.g., Introduction, Methods, Results, Conclusions), their structure follows the conventions and stylistic guidelines of the target journals. To preserve the integrity of the reading experience, each chapter is presented in its submitted or accepted form, with minor edits for consistency in notation and referencing.

Chapter 2 - Probabilistic Assessment of Shot Peening Impact Coverage Establishes the statistical foundation for modeling shot peening as a stochastic surface process. A Poisson-based framework is developed to describe the random arrival of impacts and its influence on coverage, variability, and process repeatability. The model connects operational parameters to spatial uniformity in impact coverage, providing a basis for subsequent spectral formulations.

Originally published in ***The Shot Peener Magazine****. Langdon Feltner, Paul Mort.[1]*

Chapter 3 - Spectral Fabric of Stochastic Residual Stress Fields Develops the theoretical and computational framework linking Eshelby's inclusion theory to the spatial power spectra of residual stress fields. Through analytical derivations and finite element simulations, the chapter demonstrates that residual stress heterogeneity follows predictable spectral trends, establishing the spectral fabric" as a quantitative descriptor of stochastic deformation.

Submitted to ***npj Advanced Manufacturing****. Langdon Feltner, Paul Mort.[2]*

Chapter 4 - Spectral Fabric of Heterogeneous Surface Finishes Extends the spectral framework to experimental surface measurements, showing how spatial frequency content of peened surfaces encodes process parameters such as media size, velocity,

and coverage. The analysis demonstrates the consistency of spectral descriptors across both simulated and experimental domains.

In preparation. Langdon Feltner, Rajeshree Varma, Paul Mort.

Chapter 5 - Characterization of Particle Size and Shape Distributions for Shot Peening Media Presents a comprehensive experimental study of media size and shape distributions using dynamic image analysis (DIA). Results quantify the evolution of particle morphology across as-manufactured, conditioned, and worn states, establishing statistical descriptors for use in both model calibration and process specification development.

Originally published in ***The Shot Peener Magazine****. Langdon Feltner, Paul Mort, Mark Gruninger.[3]*

Chapter 6 - Neural Network Enabled Process Flowsheet for Industrial Shot Peening Integrates the preceding analytical and experimental components into a modular flowsheet environment. A flowsheet-based architecture couples finite-element simulations, analytical models, and deep-learning surrogates to predict process-dependent stress field evolution. The approach enables efficient scenario testing and uncertainty quantification, forming a generalizable framework for stochastic surface processes.

Submitted to ***Materials****. Langdon Feltner, Paul Mort.[4]*

Chapter 7 - Summary and Future Work Summarizes the principal findings of the preceding chapters, emphasizing the connection between stochastic modeling, spectral characterization, and digital-twin implementation. Future directions include real-time process monitoring, adaptive control, and extension of the framework to other surface treatment and additive manufacturing processes.

Two additional peer-reviewed publications centered on characterization of particulate material morphology are included as appendices. Although distinct from the primary focus on stochastic surface mechanics, these works share a common methodological foundation in dynamic image analysis (DIA), spectral metrology, and statistical modeling of particulate

systems. Each appendix presents a standalone contribution addressing particle morphology and its implications for process modeling in related manufacturing domains.

Appendix A - Particle Size and Shape Analyses for Powder Bed Additive Manufacturing Demonstrates the use of dynamic image analysis (DIA) to quantify particle morphology in metallic additive manufacturing powders. The study applies principal component analysis (PCA) to map multidimensional shape distributions and evaluates sources of uncertainty arising from pixel resolution and descriptor selection. Results highlight opportunities to apply machine learning for improved image resolution and classification of particle form.

Published in ***Particuology*** *(2023). Langdon Feltner, Ethan Korte, David F. Bahr, Paul Mort. [5]*

Appendix B - On the Use of the Fourier Transform to Determine Contact Curvature Distributions in Additive Manufacturing Powders Revisits the application of Fourier transforms for particle shape characterization, introducing a curvature-based metric derived directly from differentiable particle contours. Comparative analyses of gas-atomized and mechanically reduced powders reveal distinct curvature distributions that correlate with manufacturing route and expected spreading behavior in laser powder-bed fusion.

Published in ***Powder Technology*** *(2025). Langdon Feltner, Donovan Stumpf, Paul Mort. [6]*

1.4 Author's Publications

The following publications, conference proceedings, and editorial articles were completed during the author's doctoral studies.

Peer-Reviewed Journal Articles

1. Feltner, L., Stumpf, D., & Mort, P. R. (2025). *On the use of the Fourier transform to determine contact curvature distributions in additive manufacturing powders. Powder Technology.* https://doi.org/10.1016/j.powtec.2025.120618

2. Feltner, L., & Mort, P. R. (In review). *Spectral fabric of stochastic residual stress fields. npj Advanced Manufacturing.*

3. Koleilat, L., Feltner, L., Stumpf, D., & Mort, P. R. (2025). *Mapping process-product relations by ensemble regression: A granulation case study. Chemical Engineering Science.* https://doi.org/10.1016/j.ces.2025.122042

4. Feltner, L., Korte, E., Bahr, D. F., & Mort, P. R. (2023). *Particle size and shape analyses for powder bed additive manufacturing. Particuology.* https://doi.org/10.1016/j.partic.2023.09.001

5. Feltner, L., & Mort, P. R. (In review). *Neural network enabled process flowsheet for industrial shot peening. Materials.*

6. Feltner, L., Varma, R., & Mort, P. R. (In preparation). *Spectral fabric of heterogeneous surface finishes.*

Peer-Reviewed Conference Proceedings

1. Feltner, L., Mort, P. R., et al. (2022). *Size and shape characterization for shot-peening impingement models. Proceedings of the International Conference on Shot Peening (ICSP-14)*, Milan, Italy.

2. Spink, M., Canty, T., Feltner, L., & Mort, P. R. (2025). *The use of a dynamic imaging system to characterize particle size and shape for shot peening media. Proceedings of the International Conference on Shot Peening (ICSP-15)*, West Lafayette, IN.

3. Feltner, L., & Mort, P. R. (2025). *Fourier analyses of optical profilometry as an inferential measurement for impact coverage. Proceedings of the International Conference on Shot Peening (ICSP-15)*, West Lafayette, IN.

4. Feltner, L., & Mort, P. R. (2025). *Reduced-order approach for peening stress field variability. Proceedings of the International Conference on Shot Peening (ICSP-15)*, West Lafayette, IN.

5. Feltner, L., & Mort, P. R. (2025). *Dynamic flowsheet modeling of shot peening processes. Proceedings of the International Conference on Shot Peening (ICSP-15)*, West Lafayette, IN.

6. Gentry, A. N., Feltner, L., & Mort, P. R. (2024). *A scoping review of tools for teaching particle science engineering and technology. ASEE Annual Conference & Exposition*, Portland, OR.

Editorial and Industry Publications

1. Feltner, L., & Mort, P. R. (2022). *Characterization of shot size and shape distributions. Metal Finishing News*, Fall 2022. Reissued Spring 2023 (China Edition).

2. Feltner, L., & Mort, P. R. (2023). *Stress field modeling in context of industrial shot peening. The Shot Peener Magazine*, Fall 2023.

3. Feltner, L., Gruninger, M., & Mort, P. R. (2024). *Characterization of particle size and shape distributions for shot peening media. The Shot Peener Magazine*, Spring 2024.

4. Feltner, L., & Mort, P. R. (2025). *Probabilistic assessment of peening impact coverage. The Shot Peener Magazine*, Spring 2025.

2. Probabilistic Assessment of Shot Peening Impact Coverage

2.1 Introduction

In shot peening, compressive residual stresses are induced through impact events between media and the surface of a component. When designing a shot peening machine and specifying operational parameters, practitioners often aim to achieve full and even coverage through sufficiently long cycle times and careful positioning of the peening nozzle with respect to the treated surface. Mass flow rate, peening time, and blast pressure are particularly important when considering impact coverage on a component. Over a peening cycle, a discrete number of particles leave the nozzle, each with an associated mass. For a given substrate material, particle mass, and media hardness, the size of the surface dimple left by an impact is determined by the particle's velocity, meaning the distribution of dimple coverage is directly related to the uniformity of particle mass flux.

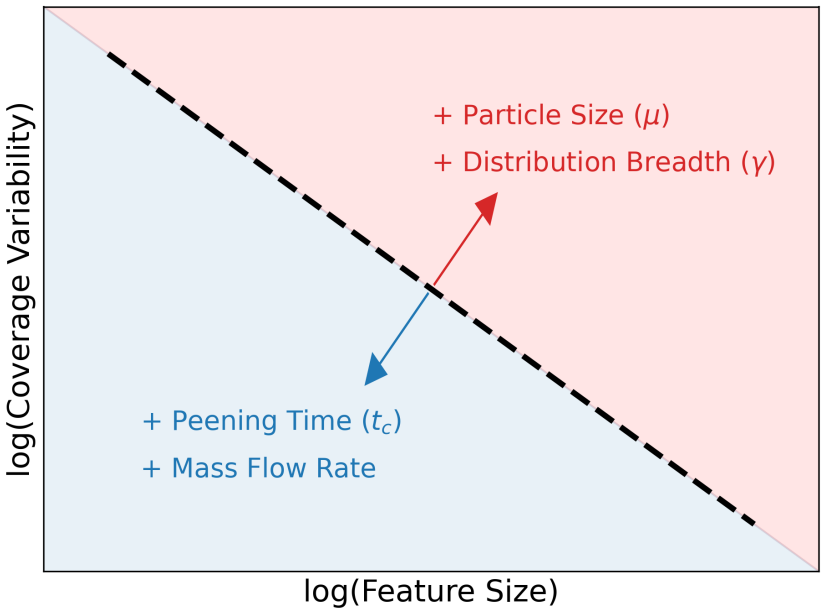

Figure 2.1. Peening time, mass flow rate, and media size distributions contribute to coverage variability across scales of scrutiny.

Considering shot media as point masses with randomly chosen impact locations upon a component of fixed area A_{part}, the average mass flux ($\dot{m}$) is equal to the summation of

all particle mass contributions over a cycle, divided by the peening time (t_c) and A_{part}, or equivalently, the mass flow rate divided by A_{part}. Within control limits, $\dot{m}$ can be considered a constant derived directly from the measured mass flow rate.

Let M_A be the total mass of media that impacts within an arbitrary region of area A, as shown in Eq. 2.1.

$$M_A = \sum_{\text{i}=1}^{n_A} m_p^{\text{i}} \tag{2.1}$$

Here, M_A depends on two distributed quantities: the number of particles that impinge on the region (n_A) and the mass of each particle (m_p^{i}). The expected, or average, value of a random quantity (denoted $E[\cdot]$) is the probability-weighted summation of all possible values the variable can take. Wald's identity [7, 8] enables a simplified calculation of $E[M_A]$, separating the contributions of the independent variables n_A and m_p^{i}. Thus, the expectation of M_A can be expressed as:

$$E[M_A] = E[n_A] \cdot E[m_p^{\text{i}}] \tag{2.2}$$

Variance (denoted $\text{Var}[\cdot]$) is a measure of the breadth of a distribution. Similar to Wald's identity, the Blackwell-Girshick equation [9] allows the separation of contributions from n_A and m_p^{i} with respect to variance. The variance of M_A can thus be expressed as:

$$\text{Var}[M_A] = E[n_A] \cdot \text{Var}[m_p^{\text{i}}] + \text{Var}[n_A] \cdot \left(E[m_p^{\text{i}}]\right)^2 \tag{2.3}$$

The relative standard deviation (denoted $\text{RSD}[\cdot]$) is defined as the ratio of the standard deviation to the mean value of a quantity. It is a dimensionless measure of proportional variability. In this context, $\text{RSD}[M_A]$ is directly related to the variability in the total work imparted onto the surface across repeated components.

The goal of this work is to apply probabilistic reasoning to characterize spatial variations in impact coverage based on cumulative mass flux over the surface of a component. Specifically, we derive expressions for $E[M_A]$, $\text{Var}[M_A]$, and $\text{RSD}[M_A]$ to establish how operational parameters influence surface treatment uniformity across different spatial scales.

2.2 Spatial Uniformity of Mass Flux

In a previous *Shot Peener* report entitled "Characterization of Particle Size and Shape Distributions for Shot Peening Media" [3], we explored volume-weighted distributions in peening media size and shape measured using dynamic image analysis (DIA). That work demonstrated the suitability of a lognormal distribution for describing size in relation to mass sieving. In the current work, DIA is used to calculate number-weighted distributions for probability-based impact coverage modeling.

A lognormal distribution in area-equivalent radius (R) implies that $\ln(R)$ is normally distributed with a dimensionless geometric mean (μ) and standard deviation (γ). To be consistent with the notation used in our previous work, $\mu \equiv \ln(d_{gN}/2)$, the natural log of half the number-weighted geometric mean particle diameter, while $\gamma \equiv \ln(\sigma_{gN})$, the natural log of the number-weighted geometric standard deviation. The expected value of a particle's radius is $\exp(\mu + \gamma^2/2)$. Because particle mass scales with radius cubed, the mass is also lognormally distributed with mean 3μ and standard deviation 3γ. Assuming constant density ρ, the expected mass of a particle is:

$$E[m_p^{\mathrm{i}}] = \frac{4\pi\rho}{3} \exp\left(3\mu + \tfrac{9}{2}\gamma^2\right) \tag{2.4}$$

The average number flux of impacts ($\dot{n}$) is the mass flux divided by the expected mass per particle. Similar to $\dot{m}$, $\dot{n}$ can be treated as constant within control limits. As shown in Eq. 2.5, $\dot{n}$ is inversely proportional to the mean radius cubed, with an additional inverse dependence on γ:

$$\dot{n} = \frac{3\,\dot{m}}{4\pi\rho \exp\left(3\mu + \tfrac{9}{2}\gamma^2\right)} \tag{2.5}$$

To illustrate the consequences of this dependence for the relative uncertainty in impact coverage, consider the case where $n \approx \dot{n}\, t_c\, A_{\mathrm{part}}$ particles are assigned random impact locations within a component of area A_{part}. For a measurement area $A \subseteq A_{\mathrm{part}}$, the probability that a particle is contained within A is $p_0 = A/A_{\mathrm{part}}$, and the probability that it is excluded

is $q = 1 - p_0$. The probability that the number of impacts within A (n_A) equals k is given by the binomial distribution:

$$P(n_A = k) = \frac{n!}{k!(n-k)!}\, p_0^k q^{n-k} \tag{2.6}$$

The binomial distribution describes the number of successes in n independent trials, each with success probability p_0. When the total number of impacts is large, the binomial distribution converges to a Poisson distribution [8]:

$$P(n_A = k) = \frac{\lambda^k \mathrm{e}^{-\lambda}}{k!}, \qquad \lambda = \dot{n}\, A\, t_c \tag{2.7}$$

The Poisson distribution has both expected value and variance equal to λ, i.e., $E[n_A] = \mathrm{Var}[n_A] = \lambda$. In the context of peening, this provides an exact probability distribution for the number of impacts within any region based on process parameters and media size.

Leveraging this equality, Eq. 2.3 simplifies to:

$$\mathrm{Var}[M_A] = E[n_A]\left(\mathrm{Var}[m_p^{\mathrm{i}}] + E[m_p^{\mathrm{i}}]^2\right) \tag{2.8}$$

Substituting $\mathrm{Var}[m_p^{\mathrm{i}}] = E[(m_p^{\mathrm{i}})^2] - E[m_p^{\mathrm{i}}]^2$ yields:

$$\mathrm{Var}[M_A] = E[n_A]\, E[(m_p^{\mathrm{i}})^2] \tag{2.9}$$

Applying the expected value of the Poisson distribution for n_A and the second moment of the lognormal mass distribution gives:

$$\mathrm{Var}[M_A] = \dot{n}\, A\, t_c \left(\frac{4\pi\rho}{3}\right)^2 \exp\left(6\mu + 18\gamma^2\right) \tag{2.10}$$

Substituting Eq. 2.5 into Eq. 2.10 yields an expression for $\mathrm{Var}[M_A]$ in terms of $\dot{m}$:

$$\mathrm{Var}[M_A] = \frac{4\pi\rho\, \dot{m}\, A\, t_c}{3} \exp\left(3\mu + \tfrac{27}{2}\gamma^2\right) \tag{2.11}$$

Because $E[M_A] = \dot{m}\, A\, t_c$, a closed-form expression for the relative standard deviation follows:

$$\mathrm{RSD}[M_A] = 2\sqrt{\frac{\pi\rho\, \exp\left(3\mu + \frac{27}{2}\gamma^2\right)}{3\,\dot{m}\, A\, t_c}} \tag{2.12}$$

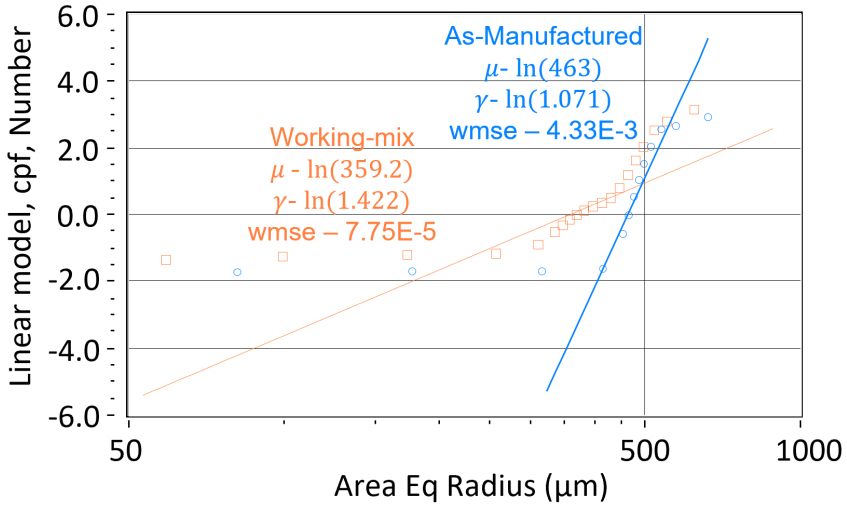

Figure 2.2. Linearized lognormal fits for area-equivalent radius of as-manufactured and working-mix CCW32 media.

To validate the Poisson model's applicability to predicting mass flux uniformity, three CCW32 media size distributions were evaluated: (1) idealized monodisperse ($\mu = \ln(463)$, $\gamma = \ln(1)$), (2) as-manufactured ($\mu = \ln(463)$, $\gamma = \ln(1.071)$), and (3) working mix ($\mu = \ln(359.2)$, $\gamma = \ln(1.422)$). As-manufactured and working-mix samples were measured via DIA as part of a Purdue University senior capstone project [10]. Linearized lognormal fits for both are shown in Fig. 2.2. Most working-mix particles are smaller than as-manufactured ones, but the working mix exhibits a significantly broader distribution.

A Monte Carlo procedure was performed to simulate impact coverage numerically. Assuming a constant mass flow rate of 20 kg/min, $A_{\mathrm{part}} = 0.03$ m^2, and $t_c = 10$ or 50 s, particles were sampled repeatedly from each distribution until the cumulative mass exceeded $\dot{m}\, t_c$. Sampled particles were assigned random (x, y) impact locations within A_{part}. The region was recursively subdivided into smaller grids to compute M_A statistics across scales.

The standard deviation of M_A divided by its mean yielded RSD$[M_A]$ as a function of measurement area. Using number-weighted distributions ensures that all particles have equal probability of impinging the surface, regardless of size.

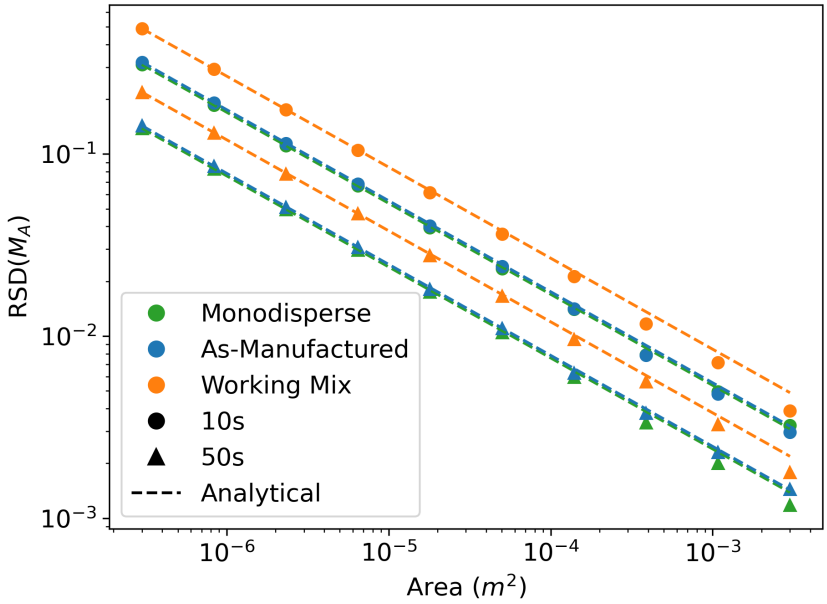

Figure 2.3. Comparison of analytical prediction with Monte Carlo results for relative variability in cumulative mass as a function of area.

Figure 2.3 compares analytical Poisson predictions for RSD$[M_A]$ with Monte Carlo simulations, showing strong agreement. Results indicate that a monodisperse approximation is reasonable for as-manufactured media, whereas the broader working-mix distribution results in lower average number flux and greater variability in impact coverage across scales.

In standard peening operations, with controlled air pressure, feed rate, and working-mix composition, this model provides insight into the effective impact distribution across scales ranging from slightly larger than the media size to full components. Limitations of this Poisson-based approach arise when the total number of impacts is small or when media distributions are extremely broad, potentially violating independence between n_A and m_p^{i}. Furthermore, the model treats particles as point masses, so mass distributions at sub-dimple scales remain ambiguous.

2.3 Conclusions

The Poisson model provides a useful starting point for predicting variability in residual stress fields across peened surfaces. Critical features of many peened components–such as axle gear roots and turbine leading edges–fall between the component scale and an individual dimple diameter, the ideal range for Poisson model validity. Because the Poisson model describes impact coverage as a counting process, it is essential to obtain number-based media size distributions, for example using dynamic image analysis (DIA).

Results suggest that peening time, mass flow rate, and media size can be systematically adjusted to control the uniformity of impact coverage. This model will be applied to guide the design of peening processes that achieve desired stress profiles while minimizing variability in critical regions of a component. More broadly, this work represents an initial step toward the development of advanced statistical frameworks linking operational parameters and transient particle size and shape distributions to spatial and temporal uniformity in both surface topography and residual stress fields.

Acknowledgements

The authors gratefully acknowledge the support of Purdue University's Center for Surface Engineering and Enhancement (CSEE). This study was motivated by valuable discussions with technical staff at American Axle & Manufacturing and Electronics Incorporated, whose open-minded collaboration contributed significantly to this work.

3. Spectral Fabric of Stochastic Residual Stress Fields

3.1 Introduction

Heterogeneous residual stress fields link microstructure to properties in materials whose internal state is shaped by both inherent heterogeneity (e.g., particle-reinforced composites) and process-induced features (e.g., mechanical surface treatments, thermal gradients, or phase transformations). Predicting the evolution and mechanical consequences of these fields requires models that bridge fine-scale plasticity with macroscopic behavior. Classical micromechanical homogenization has a rich legacy of connecting localized stress/strain distributions to continuum response [11]. Widely used approaches such as Mori-Tanaka [12, 13] and generalized self-consistent schemes [14] typically emphasize mean-field response and downplay the spatial fluctuations and correlations that govern fatigue and damage initiation.

To make these spatial organizations explicit, we adopt the language of fabric. Kanatani's formulation shows that fabric tensors provide a general tool for representing directional quantities in heterogeneous systems [15]. We extend this viewpoint to residual stress fields by defining a spectral fabric, where low-frequency content encodes the extent of long-range spatial coherence, and high-frequency content replicates the geometry of localized, process-induced features. Thus, fabric quantifies both the extent of spatial coherence and the geometry of the coherent structures themselves. The purpose of this paper is to understand the micro-scale structure of heterogeneous residual stress fields from a statistical perspective and to relate to performance and process optimization.

Shot peening presents a compelling case study. It is stochastic in nature and has a critical role in extending the fatigue life of aerospace and automotive components. Shot peening is a mechanical surface treatment process in which steel or ceramic particles (≈ 1 mm diameter) impact the surface of metal parts at high velocity (≈ 65 m/s), plasticizing the near-surface region and inducing compressive residual stresses that delay crack propagation [16]. Media flow is regulated by a continuous mass flow rate, while the number and distribution of impacts are stochastic outcomes of operational parameters such as blast pressure, cycle time, stand-off distance, and nozzle angle [17]. These parameters control the flux, velocity, and

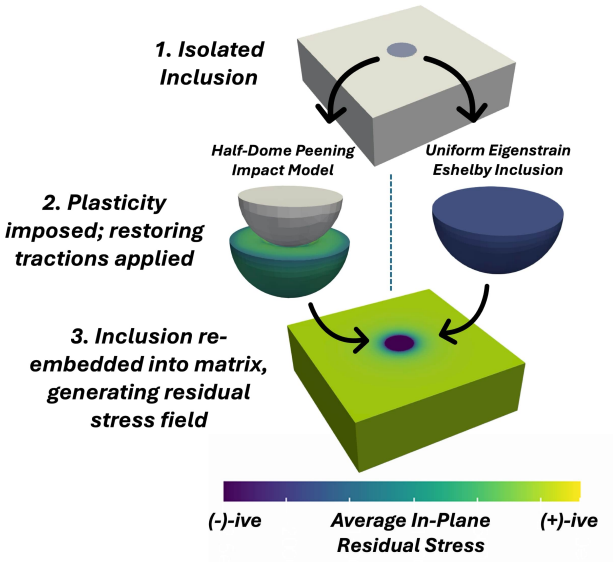

Figure 3.1. Schematic illustration of the Eshelby inclusion framework applied to shot peening impacts, enabling an analytical treatment of average in-plane residual stresses, σ_{avg}. Colorbar indicates stress in MPa.

spatial distribution of impacts, ultimately dictating the mechanical conditions that generate plastic deformation.

Hertzian contact solutions remain a common analytical tool for modeling peening, providing mean stress–depth profiles consistent with diffraction-based measurements [18–22]. They neglect stochastic overlap, plastic deformation, nonlinear material behavior, and cannot account for surface changes such as nanocrystallization [23]. As a result, analytical approaches are often supplanted by finite element simulations (FEM), which resolve nonlinear contact and predict residual stress evolution with high fidelity [24]. However, the fine discretization and small time increments required for convergence make FEM computationally expensive. While strategies such as statistically representative volume element (RVE) analysis have been used in academic studies, computational cost has limited the direct use of FEM in digital manufacturing frameworks.

We previously developed a probabilistic framework to characterize impact statistics over arbitrary surface regions [1]. Modeling impact locations as a spatial Poisson point process and particle mass as a lognormally distributed variable, we derived closed-form ex-

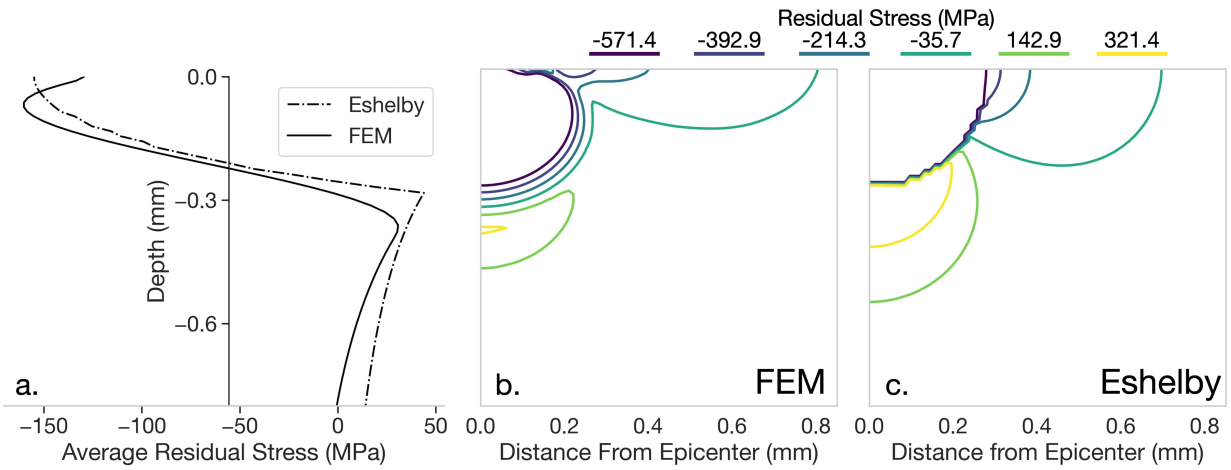

Figure 3.2. (a) Depth-resolved average residual stress profiles comparing Eshelby-based analytical predictions and finite element method (FEM) results. (b) Unfilled contour plot of the FEM-predicted residual stress field. (c) Eshelby-based residual stress contours in the same plane, with levels indicated in the legend. The boundary between plasticized and unplasticized regions appears stepped due to the discrete mesh resolution.

pressions for the mean, variance, and relative standard deviation (RSD) of impact count and cumulative mass within a sampling area, A. These metrics provide a statistically grounded alternative to traditional coverage definitions, directly linking to operational parameters.

In this work, we extend impact statistics to residual stress fields, which are central to predicting structural performance and fatigue life. To this end, we develop a micromechanical framework that integrates Eshelby's inclusion theory with spectral decomposition and a data-driven correction through the Power Spectral Density Ratio (PSDR). This framework reconciles inclusion-based predictions with finite element simulations by systematically correcting frequency bands that are over- or under-represented, enabling physically interpretable prediction of residual stress mean, variance, correlation length, and fabric. In doing so, we establish a scalable, physics-based method for quantifying and correcting residual stress heterogeneity, with direct applicability to shot peening and other manufacturing processes governed by localized, stochastic events.

3.2 Results

3.2.1 Micromechanical Foundation

Eshelby's embedded inclusion problem is a foundational result in micromechanical theory, where an imposed eigenstrain inside a bounded region induces a residual elastic stress field in the surrounding material [25]. Applied to peening, each impact can be similarly conceptualized as a localized eigenstrain, or permanent deformation, interacting with the surrounding elastic matrix. Figure 3.1 illustrates this analogy.

We propose the use of the classical solutions of Eshelby [25] and Goodier [26] for the stress fields inside and outside a spherical inclusion as a surrogate for the residual stress induced by a single peening impact normal to the treated surface, detailed in Section 3.4.2. To validate the Eshelby model as a phenomenological substitute for explicit impact modeling, we performed a series of two-dimensional axisymmetric finite element simulations of single-particle impacts. The details of these simulations are provided in Section 3.4.1.

Our FEM simulations employed a Johnson–Cook J_2 isotropic hardening material model, with properties calibrated by Ghanbari et al. [27] for Almen strips, industry-standard shot peening test specimens composed of tempered martensitic SAE 1070 steel [28, 29]. Simulations assumed spherical media with a particle radius of 0.440 mm, representative of nominal conditioned cut-wire 32 media (CCW32), and were conducted at four impact velocities (45, 65, 85, and 105 m/s) spanning a practical range of operating conditions.

We then evaluated Equations 3.4 and 3.7 on the undeformed FEM mesh coordinates, treating the FEM-predicted residual stress field as ground truth. We chose to use average in-plane residual stress as the reference stress quantity due to its translational and rotational invariances, as discussed in Section 3.4.2. Inclusion radius (a) and eigenstrain magnitude (ϵ^*) were adjusted to minimize the mean absolute error between the analytical and FEM stress fields. Mean absolute error was weighted based on the absolute magnitude of the FEM-predicted residual stress, so that the fit would not be dominated by low-stress values far from the surface. Observed best fits for ϵ^* and a and mean absolute prediction errors across all tested velocities are shown in Table 3.1. Both parameters increase monotonically with velocity and were positively correlated (R^2: 0.9765) across the tested range.

A visual comparison of the resultant stress fields from the 65 m/s impact case is shown in Figures 3.2b and 3.2c. The depth-dependent average residual stress is depicted in Figure 3.2a. Within the Eshelby inclusion domain, uniform compressive stress maps to a range of compressive values in the FEM output. As a result, the Eshelby model predicts a sharp transition between plasticized (intrainclusion) and non-plasticized (extrainclusion) regions, manifesting as a pronounced peak at a depth of approximately -0.3 mm in Figure 3.2a. Additionally, the free surface and associated traction-free boundary condition in the FEM model lead to a relaxation of near-surface stresses (between depths of -0.1 and 0 mm in Figure 3.2a), an effect not captured by the Eshelby model. This contributes to a stronger tensile region beneath the Eshelby inclusion in comparison to the FEM.

Table 3.1. Fitted Eshelby parameters and mean absolute error (MAE) for each impact velocity.

Impact Velocity (m/s)	a (mm)	ϵ^*	MAE (MPa)
45	0.2274	0.00305	74.05
65	0.2822	0.00335	113.33
85	0.3326	0.00350	151.87
105	0.3706	0.00379	189.19

Despite the differences in boundary conditions, namely the lack of a free surface and associated stress-relaxation, the Eshelby model captures the basic structure of the FEM-predicted stress fields. Henceforth, "inclusion domain" will refer to the plasticized regions of both models.

3.2.2 Ensemble Stress Fields

We conducted 16 three-dimensional finite element simulations on RVEs subjected to randomly distributed impacts. Each simulation used identical spherical particles (radius 440 μ m) impacting a 25 mm^2 domain. Impact counts of 10, 50, 100, and 500 (chosen based on the Poisson process model of impact coverage described in Section 3.4.1) were paired with velocities of 45, 65, 85, and 105 m/s. The full simulation methodology is described in Section 3.4.1.

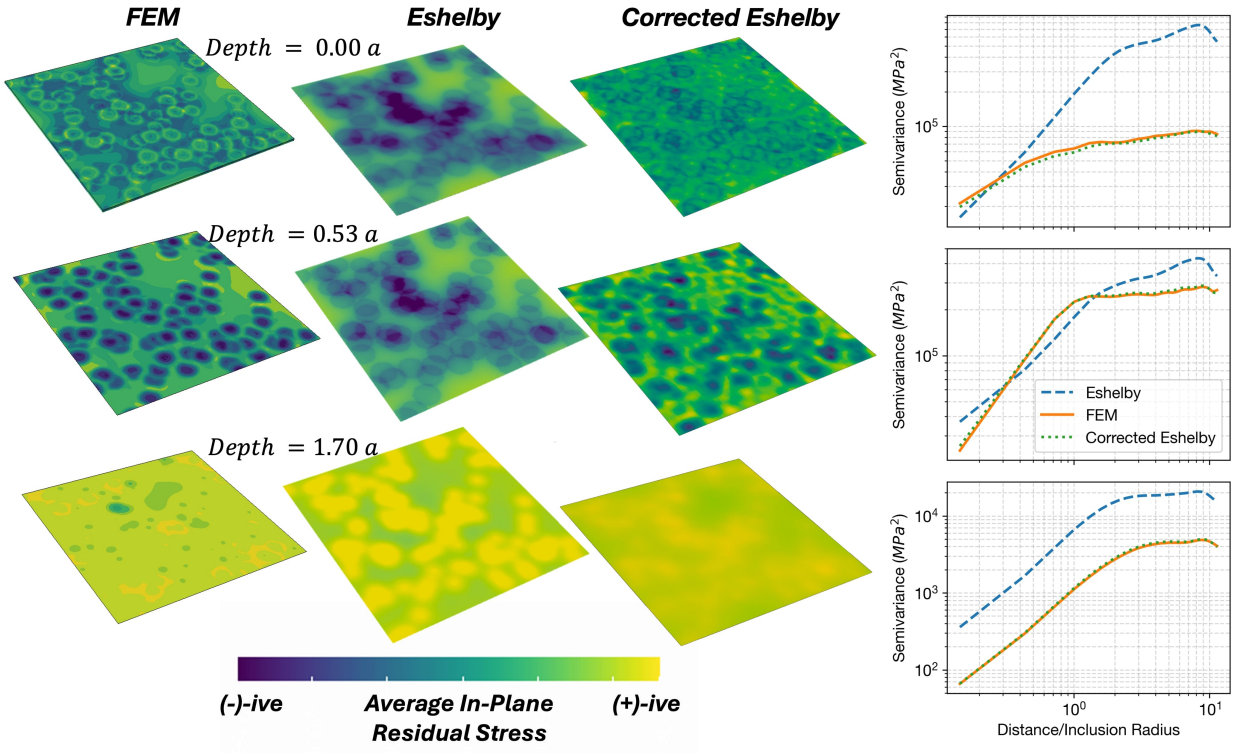

Figure 3.3. Comparison of FEM, Eshelby superposition, and PSD corrected Eshelby residual stress field across depths in units of inclusion radii. Variograms encode both scaling and the correlation structure of stresses at each depth.

We used the same sets of impact coordinates along with the eigenstrain and inclusion radius determined for the corresponding velocity of a single impact (see Table 3.1) to generate stress fields via linear superposition of Eshelby inclusions. Figure 3.3 illustrates the resulting comparison between FEM and Eshelby-based predictions for the 100 impact, $65m/s$ trial at selected depths (in units of inclusion radii). The variograms on the right side of Figure 3.3 depict the semivariance (mean squared difference between points) as a function of separation distance, normalized by the inclusion radius.

Linear superposition neglects strain hardening and cannot capture the stress saturation observed in FEM. Power-law hardening models (e.g., JohnsonCook) increase yield stress during progressive plasticity, producing vertical shifts in semivariance. Aside from vertical scaling differences, the shape of the variogram curve demonstrates the spatial correlation structure of the stress field. The semivariance typically increases monotonically at short separation distances, meaning stresses at nearby nodes typically have similar magnitudes. At larger separations, the semivariance plateaus, indicating the characteristic length scale beyond which stresses are uncorrelated and appear stochastic.

Below the plastically deformed zone (Figure 3.3, $1.70a$), the Eshelby model reproduces the FEM-predicted correlation structure, suggesting linear scaling is sufficient to reconcile the Eshelby model with the FEM results at depths below about 1 particle radius.

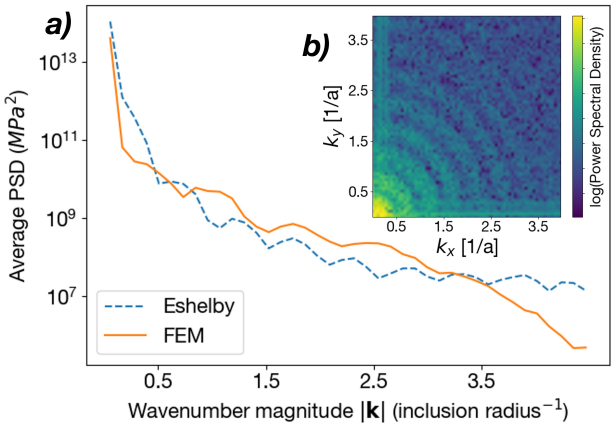

Figure 3.4. a) Comparison of Eshelby and FEM average power spectral density as a function of distance. Surface stresses, 100 impact, 65 m/s case. b) Power spectral density for Eshelby model (Surface stresses, 100 impact, 65 m/s case) showing radial symmetry about [0,0] entry.

At shallower depths, i.e., within the plastic zone (Figure 3.3, $0.00a$ and $0.53a$), the Eshelby model diverges significantly from the FEM predictions. While semivariance scaling is roughly aligned at the mid-inclusion depth ($0.53a$), the Eshelby prediction exhibits a stronger short-range correlation extending to approximately one inclusion radius. A secondary long-range correlation structure beyond one inclusion radius, signified by the sustained increase in semivariance at a shallower slope, is additionally present in the Eshelby model and is not observed in the FEM simulations. At the free surface ($0.00a$), FEM semivariance profiles are flatter than Eshelby predictions, indicating largely uncorrelated surface stresses. The Eshelby model predicts both stronger local correlations and a secondary long-range feature.

To mechanistically assess and correct these differences, we decompose the stress fields into their depth-wise spectral representations by computing their two-dimensional Fourier transforms, as described in Section 3.4.3. For a field of size $N \times N$ with domain length L, the spectral representation yields a complex array where entry $[\mathrm{i}, \mathrm{j}]$ corresponds to the harmonic with frequencies $k_x = \mathrm{i}/L$ and $k_y = \mathrm{j}/L$.

These two frequency components can be expressed compactly as a wavevector, $\mathbf{k} = (k_x, k_y)$, which specifies both the magnitude and orientation of each harmonic in frequency space. Taking the magnitude squared of each complex entry provides the relative energy contribution of each harmonic (each $\mathbf{k}$) to the overall stress field, known as the Power Spectral Density (PSD) [30]. Among these harmonics, only the $(0, 0)$ component, representing the spatial mean, has a nonzero integral over the domain; all higher-frequency components integrate to zero due to their oscillatory nature.

As a result of the isotropic nature of deformation induced by a normal impact, the PSD maps exhibited radial symmetry about the $[0, 0]$ entry of the array. Spectral energy therefore depends only on the magnitude of the wavevector $|\mathbf{k}|$, shown in Figure 3.4b. Accordingly, we analyzed the average PSD as a function of radial distance from the origin. Figure 3.4a compares the Eshelby and FEM radial PSD distributions for the surface stresses of the 100 impact, 65 m/s case.

The ratio of the FEM-derived PSD to the Eshelby-derived PSD compares the relative energy content of each spatial harmonic between the two models. Applying this ratio as a

spectral filter (PSDR) adjusts the Eshelby model to reproduce the FEM's spatial correlation structure, as shown in Figure 3.3.

Figure 3.5 shows the PSDR across wavevectors for the four tested impact counts. Following Kanatani's classification [15], harmonics with periods longer than one inclusion diameter ($|\mathbf{k}| < 0.5\,a^{-1}$) govern the long-range coherence of the stress field and are identified here as the "Macro-Fabric" (fabric tensors of the first kind). Conversely, harmonics with shorter periods ($|\mathbf{k}| \geq 0.5\,a^{-1}$) encode directional distributions of microstructural features and are referred to as the "Micro-Fabric" (fabric tensors of the second kind).

To illustrate the frequency-domain effects with real-space behavior, we separated the PSDR map into Macro-Fabric and Micro-Fabric tensors by masking the opposing frequencies before applying inverse Fourier transforms (Figure 3.5). Sub-region insets illustrate the resulting stress fields, which exhibit distinct patterns associated with both macro- and micro-scale structures.

Macro-scale frequencies (below $0.5\,a^{-1}$) contribute to the stress field surrounding each inclusion and modify the long-range correlation structure. The Macro-Fabric also contains the $[0, 0]$ entry of the frequency-space representation and therefore incorporates the mean stress, making it asymmetric. At high impact counts (≥ 100), these frequencies are attenuated at both depths, disrupting long range coherence. At low impact counts—when inclusion interactions are rare—little adjustment to the Macro-Fabric is required. Overall, the degree of attenuation increases with impact count, reflecting the nonlinear hardening response of the finite element substrate.

The Micro-Fabric, on the other hand, is symmetric by construction. Peaks in the PSDR emerge at frequencies between $0.5\,a^{-1}$ and $3\,a^{-1}$ at intervals of $0.5\,a^{-1}$, corresponding to harmonic wavelengths $[2a, a, 2a/3, a/2, 2a/5, a/3]$. On the surface, the amplification of these frequencies captures localized plasticity effects that the Eshelby model does not resolve. Consequently, the brightest yellow regions of Figure 3.5a occur in the interstices between impacts, where local interactions are most likely to produce tensile concentrations. In the subsurface region (Figure 3.5b), a single amplified frequency peak is observed, while the rest are attenuated. This combination smooths the transition between plasticized and unplasticized regions, indicating a weaker micro-scale fabric.

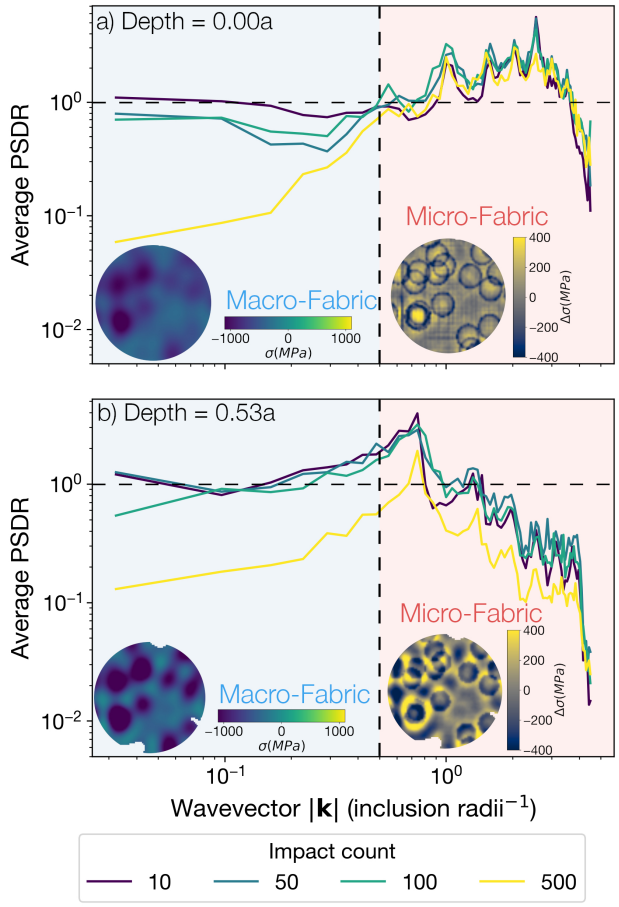

Figure 3.5. Construction of residual stress field micro- and macro-fabric at a) surface and b) mid-inclusion depths. Radial PSD filter for impact counts. Impingement graphics illustrate stress adjustments on the 50-impact case.

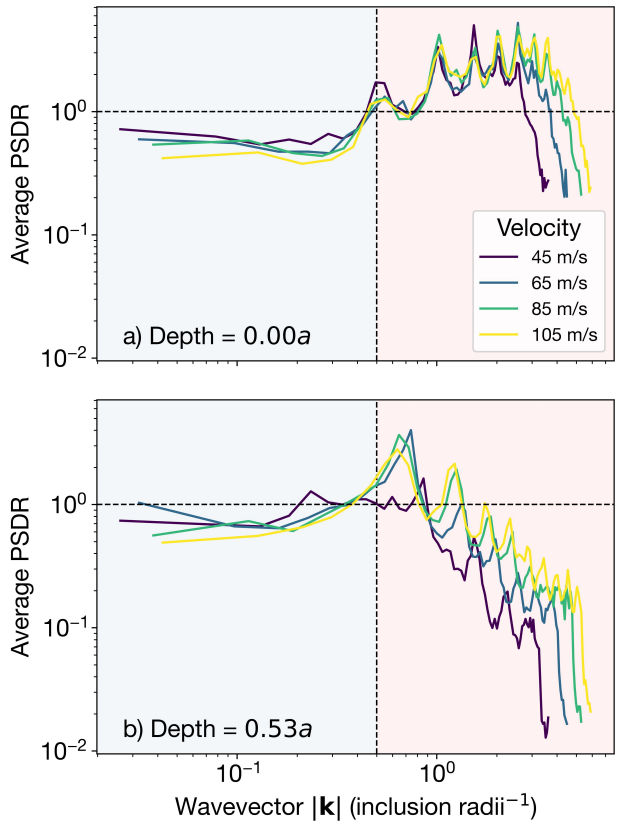

Figure 3.6. Average PSDR across wavevectors, comparing the effect of impact velocity averaged across impact counts.

Figure 3.6 extends the comparison of PSDRs (averaged across impact counts) across different impact velocities. Increasing impact velocity primarily enhances the prominence of high-frequency harmonics, although these components typically exhibit low PSD magnitudes and contribute minimally to the overall stress field structure.

At both depths, neither the locations nor the magnitudes of the frequency peaks appear to depend strongly on impact count. The stability of the Micro-Fabric filter across operational conditions supports its use as an unbiased descriptor of localized residual stress fluctuations.

Table 3.2 summarizes parity statistics between the corrected Eshelby model (Macro- and Micro-Fabric combined) and the FEM benchmark, expressed in terms of R^2. At low

coverages, both fabrics remain largely intact, and the corrected Eshelby model compares favorably with FEM predictions.

Table 3.2. R^2 as a descriptor for parity between FEM and corrected Eshelby predictions

Depth	**Velocity (m/s)**	**10**	**50**	**100**	**500**
Surface	45	0.881	0.737	0.323	0.072
	65	0.906	0.586	0.058	0.046
	85	0.861	0.400	0.003	0.038
	105	0.820	0.227	0.002	0.030
Subsurface	45	0.995	0.929	0.910	0.548
	65	0.958	0.856	0.782	0.225
	85	0.835	0.705	0.536	0.076
	105	0.790	0.617	0.353	0.041

As coverage increases, the impact-order-agnostic nature of the correction causes successive impacts to progressively weaken the Macro-Fabric while rearranging and partially erasing the Micro-Fabric. Consequently, R^2 drops sharply, approaching zero under the most aggressive conditions.

This process diminishes the ability to resolve impact-order-dependent micro-features without substantially altering the global stress magnitude distribution. The resulting field retains the overall distribution and correlation structure of FEM, but its pointwise correlations decay toward those of a stochastic field.

This trend is reflected in the normalized Wasserstein distances in Table 3.3, defined as the 2-Wasserstein metric [31] between two distributions, divided by the mean of the FEM-predicted field at the corresponding depth. The normalization produces a dimensionless measure of distributional similarity, with zero indicating identical distributions. Distances decrease with increasing coverage and velocity, demonstrating that the global statistical structure of the stress field is maintained even as pointwise coherence diminishes.

In this way, the hybrid statisticalmechanical framework remains valid across a broad range of process parameters, capturing both spatial structure and stochastic variability through spectral correction. The model adapts to the evolving nature of the system, provid-

Table 3.3. Normalized Wasserstein distances between FEM and corrected Eshelby predictions.

Depth	Velocity (m/s)	10	50	100	500
Surface	45	0.165	0.027	0.023	0.023
	65	0.087	0.025	0.034	0.027
	85	0.068	0.038	0.044	0.037
	105	0.050	0.053	0.055	0.045
Subsurface	45	0.058	0.100	0.059	0.026
	65	0.238	0.113	0.059	0.020
	85	0.444	0.141	0.062	0.027
	105	0.436	0.118	0.045	0.023

ing physically interpretable predictions where structure persists and statistically consistent degradation where it does not.

3.3 Discussion

These results demonstrate the decomposition of heterogeneous residual stress fields into fabrics that quantify both long-range coherence and local variability. Such fabrics provide a direct link between local point-of-contact deformation mechanisms and spatially-averaged performance metrics. Fabric quantification establishes a basis for predicting variability in manufacturing processes where localized, stochastic events (e.g., particle impacts, laser scans, deposition passes) accumulate into complex stress patterns. This advances reduced order residual stress modeling from deterministic superposition to a statistically aware, scalable paradigm.

In the context of digital twins for surface treatments such as shot peening, the capability to predict not only the mean residual stress profile but also its spatial variance and correlation length enables new modes of in-situ decision-making, flaw mitigation, and closed-loop control. This insight not only guides model refinement but also informs sensor design by identifying the spatial scales most critical to monitor.

Looking forward, this framework is positioned for experimental validation and process integration. In-process sensing approaches such as high-speed impact velocimetry and digital image analysis of peening media provide real-time measurements of media mass flow rate along with distributions of particle velocity, size, and shape (i.e., impact curvature). Incorporating these process-level data streams into the present model would enable adaptive calibration of spectral filters during operation, directly linking observed process fluctuations to predicted changes in residual stress statistics. Such integration would create a pathway toward autonomous process control, maintaining consistent product performance under variable operating conditions.

3.4 Methods

3.4.1 RVE Finite Element Modeling

We leveraged ABAQUS 2021 [32] to simulate representative volume elements (RVEs) of shot peening and to evaluate the applicability of the residual stress field induced by Eshelby's embedded inclusion model to both single-impact and ensemble peening conditions.

In the single-impact case, the axisymmetric nature of the deformation enabled a simplified two-dimensional model: a single half-circle representing the spherical shot particle (440 μm radius), with a reference point at its center, was positioned above a rectangular substrate block (1 mm $\times$ 1.25 mm). For ensemble simulations, spherical particles of the same radius were assigned central reference points and randomly distributed (x, y) impact coordinates within a 5 mm $\times$ 5 mm domain on a 2 mm-thick substrate. To manage overlapping impacts, particle z-heights were staggered such that adjacent particles would not strike the same location simultaneously, assuming a nominal impact duration of 1 μs. In both the 2D and 3D cases, infinite elements (CINAX4 and CIN3D8, respectively) were used along the lateral and bottom boundaries of the substrate, and out-of-plane rotation was constrained.

The shot particles were modeled as rigid bodies in both configurations. RAX2 elements were used in the axisymmetric model and R3D3 elements in the 3D model, with an approximate element size of 50 μm. A point mass of 2.801×10^{-6} kg was assigned to the

particle reference point, based on a nominal steel density of 7850 kg/m^3. A finite-sliding, node-to-surface contact algorithm was employed, and friction was neglected.

$$p_{\text{overlap}} = 1 - \exp\left(-\frac{n \cdot A_{\text{inclusion}}}{A_{\text{RVE}}}\right) \tag{3.1}$$

Impact counts were selected according to Poisson coverage theory for uniformly distributed point processes, as described by Chiu et al. [33]. Using the effective inclusion radii in Table 3.1, we computed the expected surface overlap probability p_{overlap} (Equation 3.1), with results shown in Table 3.4. The 10-impact case exhibits sparse coverage and largely independent stress contributions, whereas the 500-impact case is highly saturated, with nearly the entire surface deformed by overlapping dimples. The 50- and 100-impact cases represent intermediate regimes, allowing us to observe the transition and saturation dynamics of the induced stress field.

Table 3.4. Poisson-model coverage probabilities ($A_{\text{RVE}} = 25\,\text{mm}^2$).

Velocity (m/s)	Impact count 10	50	100	500
45	0.063	0.277	0.478	0.961
65	0.095	0.394	0.632	0.993
85	0.130	0.501	0.751	0.999
105	0.159	0.578	0.822	1.000

For the substrate, depth-wise biased meshing was applied, with surface elements sized at $\approx$ 35 μm $\times$ 35 μm $\times$ 35 μm (3D) and $\approx$ 35 μm $\times$ 35 μm (2D). Element dimensions increased linearly with depth, reaching maximum sizes of $\approx$ 35 μm $\times$ 35 μm $\times$ 175 μm and $\approx$ 35 μm $\times$ 175 μm, respectively, at the bottom boundary. C3D8R elements were used in 3D models, while CAX4R elements were used in axisymmetric models. Although element size was not adjusted based on impact velocity or coverage, grid independence was confirmed in both cases based on cumulative residual strain energy in the substrate. These mesh dimensions are consistent with the guidelines of Wang et al. [34], who reported grid independence for surface elements sized at approximately one-tenth the dimple diameter.

The substrate was modeled using a Johnson–Cook J_2 isotropic, power-law hardening material model with strain rate dependence, specifically the formulation proposed by Ghanbari et al. [27] for SAE 1070 tempered martensitic steel used in Almen test strips. Thermal softening and temperature evolution were neglected. Due to the dynamic, high-deformation nature of shot peening, ABAQUS's explicit solver was employed.

Table 3.5. Elasto-plastic material properties for the Johnson–Cook hardening model of SAE 1070 steel [27].

Parameter	**Value**
Elastic modulus, E (MPa)	210000
Poisson's ratio, ν	0.31
Yield strength, A (MPa)	1408
Hardening modulus, B (MPa)	600
Hardening exponent, n	0.234
Strain rate coefficient, C	0.0134
Thermal softening exponent, m	1
Reference strain rate, $\dot{\varepsilon}_0$ (s^{-1})	1
Room temperature, T_0 (K)	298
Melting temperature, T_M (K)	1793

3.4.2 Eshelby's Embedded Inclusion Residual Stress Field

In the context of shot peening, the geometry of the inclusion used to model a single impact should reflect the symmetry of the local plastic deformation zone generated during contact. A normal (perpendicular) impact produces an axisymmetric plastic zone centered at the contact point, which can be reasonably approximated by a spherical inclusion. This idealization preserves radial symmetry and is consistent with classical Hertzian contact mechanics. While oblique impacts introduce tangential momentum and sliding, leading to asymmetric plastic zones that are more accurately modeled by ellipsoidal inclusions, the axisymmetric stress field surrounding a spherical inclusion is advantageous for analytical development. Specifically, when the impact plane coincides with the first and second principal directions, the average in-plane residual stress,

$$\sigma_{\text{avg}} = \frac{1}{2}(\sigma_{11} + \sigma_{22}), \tag{3.2}$$

represents a rotationally invariant measure of the residual stress state within the treated plane. σ_{avg} corresponds directly to the average normal stress acting parallel to the treated surface, and therefore can be interpreted as the effective residual stress component that contributes to resisting crack initiation and propagation perpendicular to the surface.

In this work, we consider a spherical inclusion of radius a, that has undergone a uniform eigenstrain ($\epsilon_{\text{ii}} = \epsilon^*$). Eshelby showed the stress field within the inclusion is constant and a function of only eigenstrain magnitude, and material elastic constants. Using conventional Einstein indicial notation:

$$\sigma_{\text{ij}}^{(\text{in})} = -\frac{12KG}{3K + 4G}\,\epsilon^*\delta_{\text{ij}} \tag{3.3}$$

Leading to:

$$\sigma_{\text{avg}}^{(\text{in})} = -\frac{12KG}{3K + 4G}\,\epsilon^* \tag{3.4}$$

Where K and G are bulk and shear moduli respectively, and δ_{ij} is Kronecker's delta.

Goodier's solution [26] employs an Airy stress function to derive an exact expression for the residual elastic stress field outside a spherical inclusion subjected to a uniform eigenstrain:

$$\sigma_{\text{ij}}^{(\text{out})} = -4G\epsilon^* a^3 \left(\frac{\delta_{\text{ij}}}{r^3} - \frac{3x_{\text{i}}x_{\text{j}}}{r^5}\right), \tag{3.5}$$

where $r = \sqrt{x_1^2 + x_2^2 + x_3^2}$, G is the shear modulus, and a is the radius of the inclusion.

For the average in-plane residual stress, Goodier's solution becomes:

$$\sigma_{\text{avg}}^{(\text{out})} = -2G\epsilon^* a^3 \left(\frac{2}{r^3} - \frac{3(x_1^2 + x_2^2)}{r^5}\right). \tag{3.6}$$

Due to its rotational invariance within the 12 plane, σ_{avg} depends only on radial distance from the impact center in that plane. Introducing a cylindrical coordinate system with $r_\perp = \sqrt{x_1^2 + x_2^2}$ and $r^2 = r_\perp^2 + x_3^2$, the expression becomes:

$$\sigma_{\text{avg}}^{(\text{out})} = -2G\epsilon^* a^3 \frac{2x_3^2 - r_\perp^2}{(r_\perp^2 + x_3^2)^{5/2}}. \tag{3.7}$$

Denoting $a_z = \sqrt{a^2 - x_3^2}$ as the depth-resolved cross sectional radius of the inclusion, the residual stress field within and surrounding a spherical inclusion can be summarized in piecewise form:

$$\sigma_{\text{avg}}(r_\perp, x_3) = \begin{cases} -\dfrac{12KG}{3K+4G}\,\epsilon^* & r_\perp \le a_z \\ -2G\epsilon^* a^3 \dfrac{2x_3^2 - r_\perp^2}{(r_\perp^2 + x_3^2)^{5/2}} & r_\perp > a_z \end{cases} \tag{3.8}$$

3.4.3 Power Spectral Ratio Construction

Consider two ensemble residual stress fields, $\sigma_{\text{FEM}}(x, y, z)$ and $\sigma_{\text{Eshelby}}(x, y, z)$, corresponding respectively to finite element model predictions and Eshelby inclusion superposition predictions. Rather than analyzing the full three-dimensional field at once, each depth layer $z = z_{\text{i}}$ is treated independently.

First, each layer is transformed into the frequency domain via a two-dimensional Fourier transform:

$$\hat{\sigma}_{\text{FEM}}(k_x, k_y, z_{\text{i}}) = \mathcal{F}_{2D}\left\{\sigma_{\text{FEM}}(x, y, z_{\text{i}})\right\}, \tag{3.9}$$

$$\hat{\sigma}_{\text{Eshelby}}(k_x, k_y, z_{\text{i}}) = \mathcal{F}_{2D}\left\{\sigma_{\text{Eshelby}}(x, y, z_{\text{i}})\right\}. \tag{3.10}$$

Next, the magnitudes of these frequency-space representations are used to define a spectral transfer function for each layer (with small denominators regularized to avoid singularities):

$$\Psi(k_x, k_y; z_{\text{i}}) = \frac{\left|\hat{\sigma}_{\text{FEM}}(k_x, k_y, z_{\text{i}})\right|^2}{\left|\hat{\sigma}_{\text{Eshelby}}(k_x, k_y, z_{\text{i}})\right|^2}. \tag{3.11}$$

The corrected stress field for each layer, $\sigma_{\text{corr}}(x, y, z_{\text{i}})$, is obtained by applying this transfer function to the Eshelby model in frequency space, followed by an inverse Fourier transform back to spatial coordinates:

$$\sigma_{\text{corr}}(x, y, z_{\text{i}}) = \mathcal{F}_{2D}^{-1}\left\{\hat{\sigma}_{\text{Eshelby}}(k_x, k_y, z_{\text{i}}) \cdot \Psi(k_x, k_y; z_{\text{i}})\right\}. \tag{3.12}$$

This procedure corrects the Eshelby-derived field so that its spatial correlation structure matches the power spectral characteristics observed in the FEM predictions [30]. Additionally, the spectral transfer function $\Psi(k_x, k_y; z_\mathrm{i})$ can be decomposed into attenuated frequencies ($\Psi(k_x, k_y; z_\mathrm{i}) < 1$), where the Eshelby model overpredicts spectral energy, and amplified frequencies ($\Psi(k_x, k_y; z_\mathrm{i}) > 1$), where the Eshelby model underpredicts spectral energy. Applying each of these sets independently to $\hat{\sigma}_{\mathrm{Eshelby}}$ facilitates the identification and assessment of the underlying physical mechanisms responsible for structural differences between the FEM and Eshelby fields.

3.5 Data Availability

The simulation codes used in this study are openly available on GitHub at: https://github.com/feltner515/EshelbyFabric.

4. Spectral Fabric of Heterogeneous Surface Finishes

4.1 Introduction

Heterogeneous surface finishes frequently arise in manufacturing processes characterized by stochastic dynamics. For example, in powder-based additive manufacturing, surface topography emerges from the combined effects of powder spreading, particle packing, and melt-pool solidification [35]. Surface finish is not merely cosmetic; it mediates performance pathways in engineering systems. In the most severe cases, surface irregularities act as precursors for crack initiation, accelerating propagation and driving premature failure [36]. Conversely, in well-engineered multi-component systems, controlled texturing can enhance lubrication retention, reduce friction, and prolong durability—a principle exploited in gear transmissions and sliding interfaces [37]. Areal roughness metrics (e.g., S_A, S_Z) remain the industrial standard, but they collapse rich spatial structure into scalar values. While these scalars are sensitive to processing changes, they cannot uniquely recover the underlying process conditions: different paths often lead to identical roughness values.

To address these limitations, recent work has explored frequency-domain approaches to surface characterization. Rodríguez et al. examined how to robustly determine surface roughness power spectra, identifying sources of error in optical profilometry and clarifying relationships between one- and two-dimensional spectra [38]. Gong et al. demonstrated that power spectral density (PSD) derived from AFM measurements captures correlation lengths and spatial heterogeneity missed by conventional parameters [39]. Podulka et al. further used spectral filtering to evaluate high-frequency roughness components and separate true topographic features from measurement noise [40], while autocorrelation-based spectral approaches have been applied to detect periodic features in turned composite surfaces [41]. These studies establish PSD as a valuable metrological tool, yet they primarily treat spectra as measurement objects rather than as process-informed structural descriptors.

In our previous work, we introduced the concept of spectral fabric to describe heterogeneous residual stress fields generated by stochastic impact processes, using shot peening as the motivating case study [2]. There, we showed that the power spectrum of stress fields encodes both nonlinear hardening behavior (macro-fabric) and the geometry of localized plas-

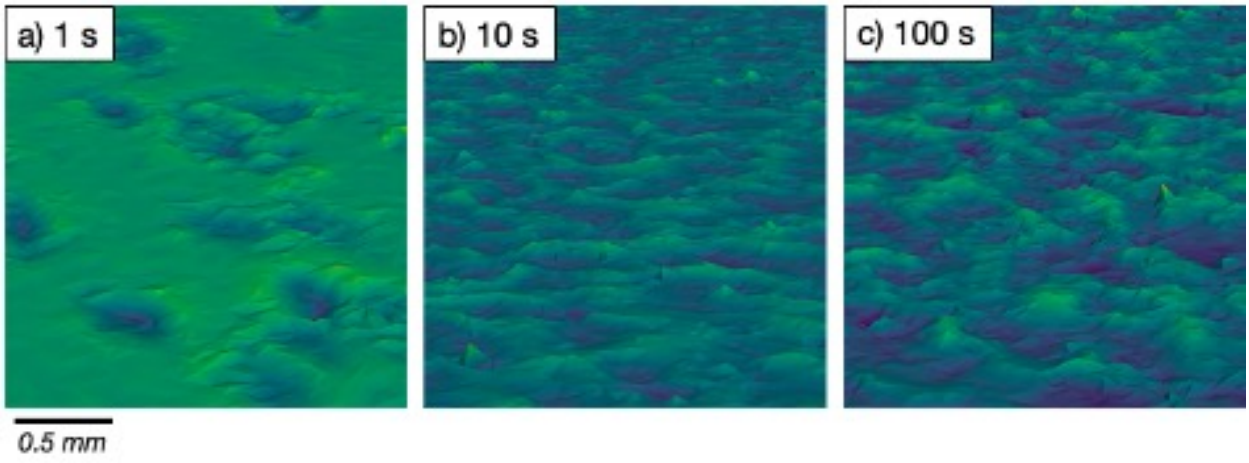

Figure 4.1. Optical profilometry scans of Almen strips peened with CCW 32 media at 62 m/s for 1, 10, and 100 s, showing the transition from discrete to fully overlapped impact coverage.

tic zones (micro-fabric), with the latter remaining invariant to impact coverage. This result suggested that fundamental process signatures—particle size, velocity, and morphology—are directly embedded in frequency content.

Here, we present an experimental follow-up to that work by extending spectral fabric analysis from stress fields to surface finishes, again using shot peening as the test case. Leveraging optical profilometry and Fourier-based decomposition, we demonstrate that PSD features of peened surfaces encode coherent structures reflecting media morphology and nonlinear hardening behavior. In this formulation, spectral fabric is both physics-informed, grounded in the mechanics of impact and plastic deformation, and experimentally measurable with standard surface metrology. This dual role bridges modeling and measurement, positioning spectral fabric as a process-sensitive descriptor that links operational parameters to observable surface morphology in a physically interpretable way.

4.2 Results

4.2.1 Principal Radii of Curvature

As described in Section 4.4.1, eighteen Almen strip specimens were peened, representing a full factorial combination of three cycle times, three impact velocities, and two media types. Their surface finishes were subsequently characterized using optical profilometry.

Figure 4.1 shows optical profilometry scans for the 1 s, 10 s, and 100 s trials, all peened with CCW 32 media at an impact velocity of 62 m/s. The 1 s surface exhibits sparse coverageindividual dimples are largely discrete, overlap is rare, and a substantial portion of the area remains unaffected by impacts. In contrast, the 10 s and 100 s surfaces are more uniformly deformed: both appear fully covered, and the boundaries of individual dimples are difficult to discern.

As described in Section 4.4.2, each surface was partitioned into 2 mm $\times$ 2 mm subregions, and the two-dimensional Fourier transform of each subregion was computed to obtain its power spectral density (PSD) map. These maps quantify the contribution of individual spatial harmonics to the measured surface profile.

Normalized power spectral density ratio (PSDR) maps were then constructed by dividing the PSD of each peened region by that of the corresponding unpeened reference surface. To capture both mean spectral behavior and spatial variability, 100 subregions were randomly sampled from each surface using a bootstrap procedure, as detailed in Section 4.4.2.

Figure 4.2 shows average PSDR maps for the 1, 10, and 100 s cycle times for CCW 32 media at an impact velocity of 62 m/s. The colormap represents $\log(1 + \text{magnitude})$. The red ellipses denote the principal radii of curvature, extracted from the second-moment tensor representation, as described in Section 4.4.3. PSD magnitudes increase with cycle time as a result of more extensive surface deformation, while the 76° impact angle produces elongation in the dimple geometry that manifests as anisotropy in the PSD maps.

Figure 4.3 summarizes the trends in major radius ($\ell_{\max}$), aspect ratio (α), and misorientation angle (θ) for all 18 peening conditions (Section 4.4.3).

The orientation θ defines the angle of the major principal radius of curvature (the long axis of the spectral ellipse) relative to the k_x-axis of the Fourier plane. Because the

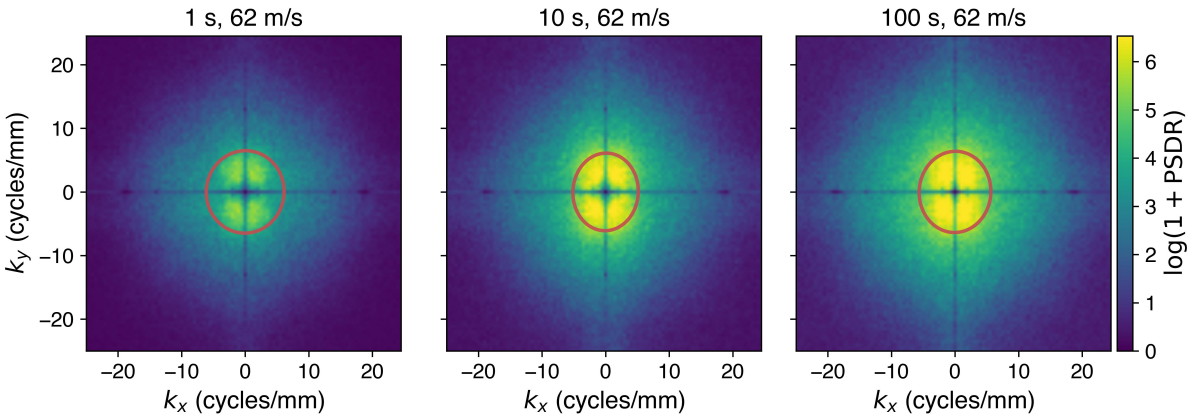

Figure 4.2. Two-dimensional PSD maps for the 1, 10, and 100 s cycle times of CCW 32 media peened at 62 m/s and a 76° impact angle. The colormap shows log(1 + magnitude), highlighting increasing spectral power with cycle time and anisotropy associated with oblique impact geometry.

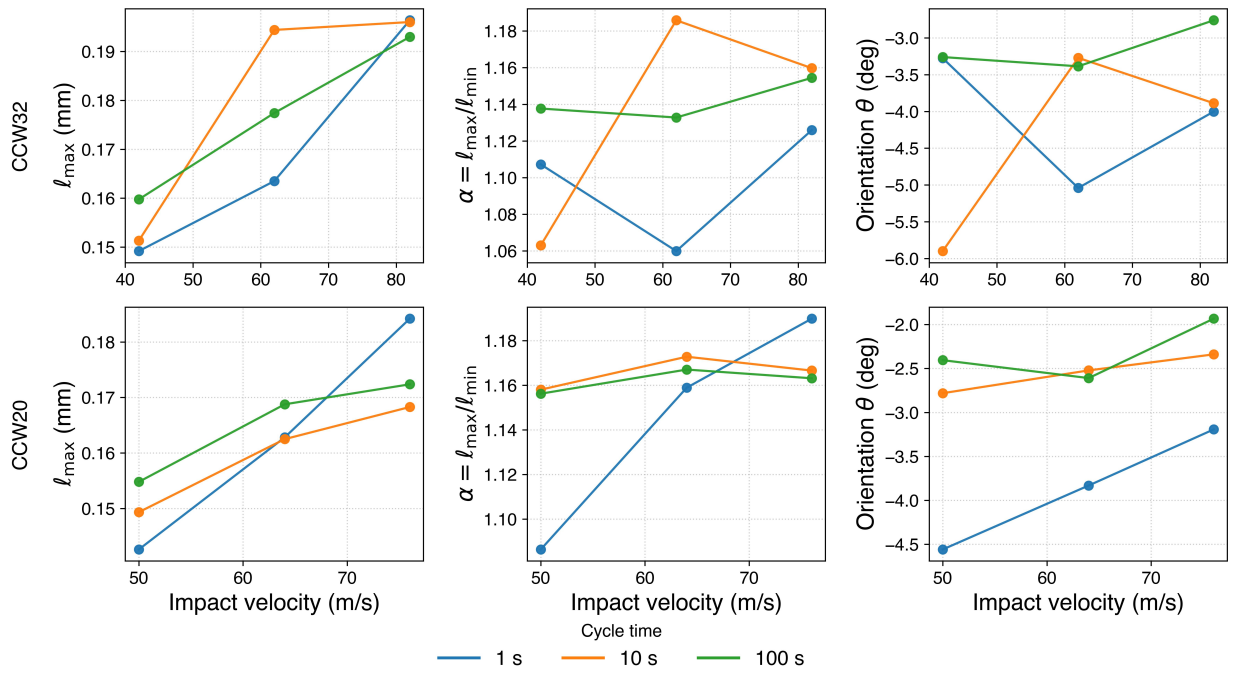

Figure 4.3. Principal spectral metrics from two-dimensional PSDR analysis. Shown are the major wavelength ($\ell_{\max}$), aspect ratio (α), and misorientation angle (θ) for all peening conditions. Curves are colored by cycle time and separated by media type (CCW32, CCW20).

curvature tensor $\mathbf{C}$ is symmetric, the two principal radii are strictly orthogonal; however, their collective orientation may deviate from the coordinate system of the Fourier transform. Small variations in θ therefore quantify directional bias or anisotropy in the spectral field induced by oblique impact geometry and serve as an additional measure of process variability.

The dominant wavelength $\ell_{\max}$ increases monotonically with impact velocity, and the larger CCW32 media produce correspondingly larger surface features than CCW20. By contrast, $\ell_{\max}$ shows no clear dependence on cycle time for either media type.

Neither α nor θ vary appreciably with impact velocity or cycle time. Both remain within narrow bounds: all principal axes are within 6° of orthogonal alignment, and all aspect ratios fall within approximately 0.1, indicating that surface anisotropy remains low across all tested conditions.

4.2.2 Spectral Invariants and Self-Similar Scaling

In addition to the principal radii of curvature, the spectral invariants J_1 and J_2 provide a compact means to characterize how the PSDR field evolves with peening severity (Section 4.4.3). The first invariant, J_1, defined as the trace of the PSDR map, provides a scalar measure of spectral amplification along isotropic harmonics in frequency space, and it increases monotonically with deformation intensity. The second invariant, J_2, measures the variance of tensor components about their isotropic mean, quantifying the portion of spectral energy stored in anisotropic modes.

In the case of perfect self-similarity–when increased peening produces geometrically identical distortions differing only in amplitude–the proportions of isotropic and anisotropic components remain fixed. Scaling the PSDR tensor by a constant factor $\Phi' = \lambda\Phi$ therefore yields

$$J_1' = \lambda J_1, \qquad J_2' = \lambda^2 J_2, \tag{4.1}$$

implying that an ideally self-similar field satisfies

$$J_2 \propto J_1^2. \tag{4.2}$$

Any deviation from this quadratic relationship indicates that increasing peening severity alters not only the magnitude but also the internal organization of the spectral field–for example, through progressive isotropization or coalescence of surface features.

Figure 4.4 shows that J_2 scales nearly quadratically with J_1 ($J_2 \propto J_1^{1.86}$, $R^2 = 0.996$), confirming that the anisotropic spectral energy grows almost self-similarly with overall spectral amplification. A slope of exactly two would correspond to geometric self-similarity, while the observed sub-quadratic exponent indicates mild structural evolution toward isotropy at higher deformation levels.

Together, the invariants J_1, J_2, and the characteristic length $\ell_{\max}$ form a concise, physically interpretable triad of descriptors:

- J_1: total isotropic (deformation) energy,

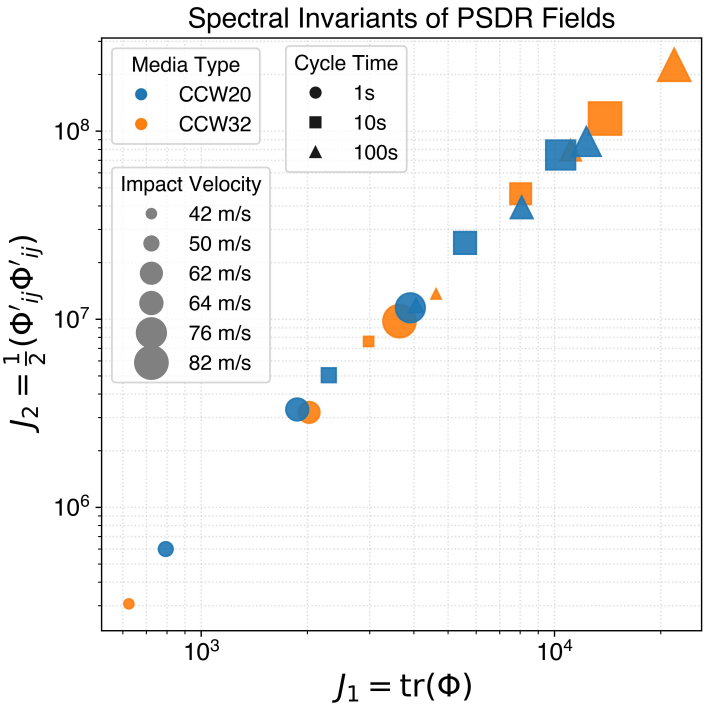

Figure 4.4. Relationship between the first and second spectral invariants across all media types and process velocities.

- J_2: anisotropic spectral energy,
- $\ell_{\max}$: dominant surface wavelength (feature spacing).

These quantities collectively define the spectral fabric of the peened surface, encapsulating both the intensity and organization of the deformation field across process conditions.

4.3 Discussion

The experimental results demonstrate that the spectral organization of peened surfaces follows reproducible, process-dependent patterns that are well described by the invariant framework previously developed for residual stress fields. The near-quadratic scaling between the anisotropic and total spectral energies ($J_2 \propto J_1^{1.86}$) implies that increasing peening severity amplifies the full spectral field in a nearly self-similar manner. The slightly

sub-quadratic exponent observed here indicates mild structural evolution toward isotropy as coverage increases: overlapping dimples progressively erase directional bias introduced by oblique impact geometry. This interpretation aligns with the modest decline in anisotropy metrics (α, θ) across cycle times (Figure 4.3) and the rotationally symmetric growth of PSD power at higher deformation levels (Figure 4.2).

Future work should consider whether this scaling exponent can be generalized into a self-similarity modulus—a material-dependent quantity that links constitutive response to spectral organization. If the exponent reflects how a material redistributes plastic work across spatial modes, then differences in strain-hardening behavior, elastic modulus, or yield strength should systematically alter the J_2–J_1 slope. Establishing such a relationship would extend the current geometric–kinematic framework into a constitutive one, enabling prediction of spectral evolution across alloys and heat treatments from first-principles material properties.

From a manufacturing-analytics perspective, these spectral descriptors provide a compact yet physically interpretable basis for process monitoring. Because $\Phi(k_x, k_y)$ acts as a spectral transfer function linking unpeened to peened surfaces, its invariants can be computed directly from optical profilometry data in near real time. Embedding J_1, J_2, and $\ell_{\max}$ into data pipelines enables quantitative mapping between machine settings and measurable surface states, offering a path toward adaptive control of shot-peening intensity or media condition. More broadly, the same invariant framework can extend to any stochastic impact or deposition process—abrasive blasting, cold spray, or powder spreading—where heterogeneous surface structure arises from ensembles of localized plastic events. In this sense, spectral fabric serves as a unifying language between modeling and metrology, translating the physics of deformation into directly observable spectral signatures.

4.4 Methods

4.4.1 Experimental Procedure

Surface finishes were characterized on eighteen Almen strip samples treated with a laboratory-scale shot peening system (sentenso GmbH, Datteln, Germany). Two media

types were investigated: G1 grade conditioned cut wire 32 (CCW32, nominal diameter ∼0.8 mm) and conditioned cut wire 20 (CCW20, nominal diameter ∼0.5 mm).

For CCW32 media, a full factorial design of three impact velocities (42, 62, and 82 m/s) and three cycle times (1, 10, and 100 s) was tested. For CCW20 media, the same cycle times and impingement angle were used, but the achievable media velocities naturally shifted to approximately 50, 64, and 76 m/s due to the smaller particle size under equivalent machine settings. In all experiments, the impingement angle was fixed at 76°, and the mass flow rate was maintained at 2 kg/min. Particle velocities were measured using the sentenso VelocityEasy high-speed camera system. The complete matrix of process parameters is summarized in Table 4.1.

Three-dimensional topographies were acquired using a Keyence VR-6000 optical profilometer, producing high-density point clouds subsequently resampled onto uniform grids with 20 ţm spacing via linear interpolation.

4.4.2 Normalized Power Spectral Density Ratio (PSDR)

To isolate the spectral contribution of peening from baseline surface texture and instrument noise, a normalized power spectral density ratio (PSDR) was constructed using unpeened strips as references. For each peened surface $h_{\mathrm{p}}(x, y)$ and the baseline surface $h_{\mathrm{b}}(x, y)$, two-dimensional Fourier transforms were computed[42]:

$$\hat{h}_{\mathrm{p}}(k_x, k_y) = \mathcal{F}_{2D}\{h_{\mathrm{p}}(x, y)\}, \tag{4.3}$$

$$\hat{h}_{\mathrm{b}}(k_x, k_y) = \mathcal{F}_{2D}\{h_{\mathrm{b}}(x, y)\}. \tag{4.4}$$

Table 4.1. Shot peening process parameters used in laboratory-scale experiments (18 total cases).

Media Type	Velocity (m/s)	Cycle Time (s)
CCW32 (0.8 mm)	42, 62, 82	1, 10, 100
CCW20 (0.5 mm)	50, 64, 76	1, 10, 100

To quantify spatial variability and anisotropy across heterogeneous surfaces, we employed a two-dimensional bootstrap resampling approach. Each surface height field was partitioned into square windows of size $2 \times 2\ mm^2$. For each randomly selected window, a two-dimensional Fourier transform was computed, and the squared magnitude yielded a local power spectrum $P_{\mathrm{i}}(k_x, k_y)$.

A baseline spectrum $P_0(k_x, k_y)$ was generated by averaging 100 windows from the unpeened strip. Each peened surface was then sampled at 100 random locations to form an ensemble of local PSDR maps:

$$\Phi_{\mathrm{i}}(k_x, k_y) = \frac{P_{\mathrm{i}}(k_x, k_y)}{P_0(k_x, k_y)}. \tag{4.5}$$

The resulting ensemble $\{\Phi_{\mathrm{i}}\}_{\mathrm{i}=1}^{100}$ represents a statistical distribution of the local spectral response. Median and percentile maps (e.g., 1090%) derived from this ensemble quantify uncertainty in spectral amplification. In contrast to one-dimensional radial averages, the two-dimensional PSDR retains information about anisotropy and directional coupling between orthogonal frequency components.

The ensemble-averaged PSDR field is then defined as

$$\Phi(k_x, k_y) = \frac{|\hat{h}_{\mathrm{p}}(k_x, k_y)|^2}{|\hat{h}_{\mathrm{b}}(k_x, k_y)|^2}. \tag{4.6}$$

This ratio acts as a spectral transfer function, emphasizing frequency bands where peening introduces new roughness or periodicity relative to the baseline surface. Small denominators in the baseline spectrum were regularized to suppress numerical instabilities. By construction, $\Phi = 1$ corresponds to unaffected frequencies, $\Phi > 1$ to amplified bands, and $\Phi < 1$ to attenuated ones.

4.4.3 Tensorial Representation and Spectral Invariants

Each bootstrapped PSDR realization was reduced to a second-moment tensor representation[43],

$$\mathbf{C} = \frac{1}{\langle \Phi \rangle} \int \Phi(k_x, k_y) \begin{bmatrix} k_x^2 & k_x k_y \\ k_x k_y & k_y^2 \end{bmatrix} dk_x\, dk_y, \tag{4.7}$$

where the normalization term $\langle \Phi \rangle = \int \Phi(k_x, k_y)\, dk_x\, dk_y$ represents the total spectral energy. The tensor $\mathbf{C}$ thus corresponds to the normalized second spatial moment of the spectral energy distribution in the Fourier domain, analogous to a covariance matrix in probability theory. It is symmetric, positive semidefinite, and its eigenvalues and eigenvectors describe the principal directions and relative spread of energy in wavenumber space. The corresponding spectral length scales are defined as $\ell_{\mathrm{i}} = 1/\sqrt{c_{\mathrm{i}}}$, where c_{i} are the eigenvalues of $\mathbf{C}$. The aspect ratio $\alpha = \ell_{\max}/\ell_{\min}$ quantifies the degree of anisotropy, while the orientation θ denotes the angle of the major principal axis relative to the k_x-axis of the Fourier plane.

The full-field PSDR maps enable the definition of spectral invariants analogous to those used in continuum mechanics [44]:

$$J_1 = \mathrm{tr}(\mathbf{\Phi}), \qquad J_2 = \tfrac{1}{2}\Phi'_{\mathrm{ij}}\Phi'_{\mathrm{ij}}, \qquad \Phi'_{\mathrm{ij}} = \Phi_{\mathrm{ij}} - \tfrac{J_1}{n}\delta_{\mathrm{ij}}. \tag{4.8}$$

Here, Einstein summation over repeated indices is implied. The operator $\mathrm{tr}(\,\cdot\,)$ denotes the tensor trace, δ_{ij} is the Kronecker delta (the identity tensor $\mathbf{I}$), and n is the tensor dimension. The first invariant, J_1, represents the isotropic component of the PSDR field–capturing the mean spectral amplification along nominally isotropic harmonics–while the second invariant, J_2, quantifies the magnitude of anisotropic deviation about that mean.

Together with the characteristic wavelength $\ell_{\max}$, these invariants form a compact tensorial basis for describing how peening modifies the spatial organization of surface roughness. This framework enables direct, physically interpretable comparison across media types, velocities, and cycle times while preserving both amplitude and directional information in the spectral domain.

5. Characterization of Particle Size and Shape Distributions for Shot Peening Media

5.1 Introduction

The relationship between the size distribution of steel shot and the residual stress field generated by shot peening is a critical aspect of the process. The residual stress field is a key factor in determining the mechanical properties and performance of treated parts such as springs, axles, and gears. Size and shape distributions of shot media directly affect the impact energy and contact stress in the peening process. This paper discusses measurement and specification of size and shape characteristics as they apply to as-manufactured and in-use media. Further, we consider the use of size and shape descriptors in model-based process control and optimization.

In addition to the support of the Purdue Center for Surface Engineering and Enhancement (CSEE), the work covered in this paper includes the efforts of several teams of students who participated in Materials Processing and Design, a capstone course for MSE Seniors at the Purdue University School of Materials Engineering. Samples of as-manufactured and in-use media used in these studies were provided by Toyo Seiko NA, Ervin Industries, and American Axle Manufacturing. The objective was to establish a robust statistical basis for size and shape characterization and specification. Dynamic image analysis (DIA) was used to collect large numbers of particle images comprising randomly oriented two-dimensional projections of three-dimensional shot particles, as illustrated in Figures 5.1 and 5.2.

Detailed analysis and graphical representation of the image data was done at Purdue using specialized software for analysis of size and shape distributions (PD23). The software is suitable for size and shape analysis of image data collected over a range of applications, i.e., it is not specific to particle scale, material, or method of dispersion. A statistical approach to characterization using geometric means and standard deviations, d_g and σ_g, along with distribution moments (number, area, volume), is described in [45]. Other recent publications discuss DIA in the context of shot peening [46] and metal powder additive manufacturing [5]. More broadly, industrial adoption of DIA continues to expand, for example ranging from pharmaceutics to geotechnics.

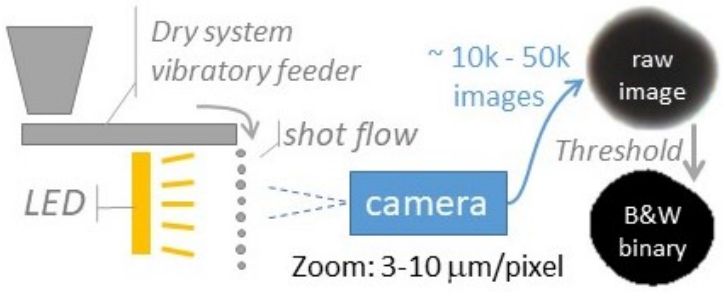

Figure 5.1. Dynamic Image Analysis (DIA) schematic.

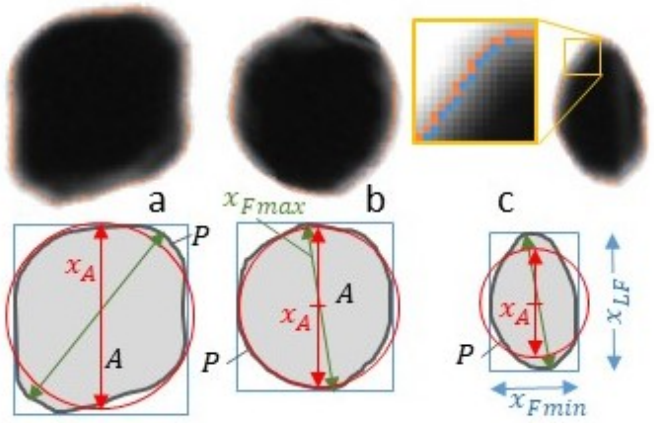

Figure 5.2. Analysis of images representing modes in the working mix: (a) sub-conditioned CW; (b) conditioned CW; (c) worn media. Orange pixels in grayscale images show thresholding. Bounding boxes (blue) and equivalent-area circles (red) illustrate size features.

Many studies on particle image analysis are available in the literature. With advances in digital imaging technologies, size and shape analyses are becoming more routine for many applications. However, given the long history of the field, there is some ambiguity in the terminology of shape descriptors and analysis methodologies for same. For example, there is considerable ambiguity associated with “sphericity”, “roundness”, and “circularity”.

As a starting point, this study references the guidance and terminology of the International Standards Organization [47], including Feret lengths ($x_{F\min}$, x_{LF}, $x_{F\max}$), area-equivalent diameter,

$$x_A = \sqrt{\frac{4A}{\pi}}, \tag{5.1}$$

and form factor,

$$FF = \frac{4\pi A}{P^2}, \tag{5.2}$$

where A is the projected area and P is the perimeter.

5.2 Distributed Variability in Peening Media

In the current study, we consider a combined dataset having a mix of as-manufactured, conditioned, and worn media, all using CW32 media. The wear threshold was determined using a multi-modal analysis of in-use media sampled at three different times (Figure 5.3). A transition from conditioned to worn media was consistently observed at about 780 μm. Above this threshold, media are in states of conditioning or preliminary wear, initially increasing sphericity with peening, and then gradually decreasing in size by surface erosion. Below the threshold, media have a distribution of shapes including a portion that is evenly worn and well-rounded, and a portion having more severe wear with breakage and shape degradation (e.g., Figure 5.2c).

A factor analysis of size and shape variables reveals two critical features, one describing size (x_A), and the other shape (form factor, FF), together explaining about 73% of the sample variance (Figure 5.4). The grayscale contours representing the volume-based density of the working mix are overlaid by a quadrant grid that illustrates the media lifecycle (I through IV) in the peening process. Combining statistical, graphical, and mechanistic perspectives provides a path toward updated size and shape specifications proposed in Section 5.3.

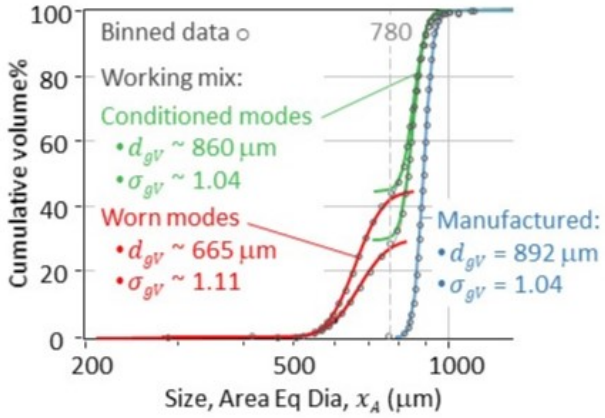

Figure 5.3. Size distributions of as-manufactured and working-mix CW32 samples. Bimodal working-mix data show the range of three samples: conditioned modes > 780 μm, worn modes < 780 μm.

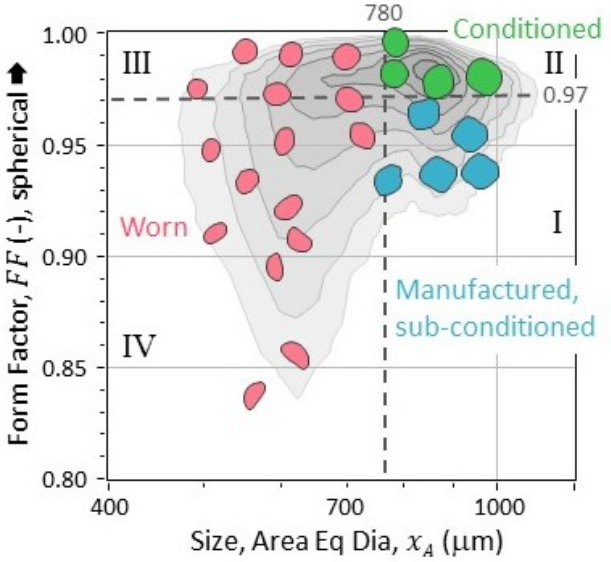

Figure 5.4. Size/shape quadrant map: (I) as-manufactured, sub-conditioned; (II) conditioned; (III) worn and well-rounded; (IV) worn with shape distortion. Quadrant boundary thresholds ($x_A = 780$ μm, $FF = 0.97$) are based on multimodal size and shape analyses.

5.3 Media Size and Shape Specifications – DIA

A definitive step has been taken to create a guideline for media size and shape specification using Dynamic Image Analysis (DIA) as an alternative to existing sieving and manual inspection procedures. Example guidelines are illustrated using DIA data for as-manufactured S110 and CW14 media.

Figure 5.5 illustrates the equivalent area diameter (most relevant to peening) in context of two-sided specification limits based on SAE J2441 [48]. Note that the size distribution considers the full two-dimensional projection area of the media rather than the minimum dimension obtained by sieving.

Shape archetypes that are provided for the purpose of visual inspection in AMS2431 [49] were quantified using orthogonal image-analysis shape factors, AR_{box} and EFF, with the form factor contours overlaid. Figure 5.6 provides an illustrative reference between legacy shape specifications–which required manual inspection–and proposed shape specifications using automated image analysis.

Figure 5.7 illustrates form factor limits using the same two examples of as-manufactured media that are shown in Figure 5.5. The form factor provides a quantitative measure of shape that combines the effects of elongation and angularity illustrated in Figure 5.6.

Compared to the CW32 working-mix media discussed in the body of the paper, shape control of finer media (e.g., CW14 and S110) is more challenging. In this example, the Q_{50} limit is a challenge for conditioning of as-manufactured CW, and the Q_5 limit is a challenge for shape characterization of cast media. Further refinement of form-factor quantile limits can be developed for specific peening applications.

5.4 Conclusion

Dynamic Image Analysis (DIA) has proven to be a viable technology to measure the size and shape of particulate matter including, for the purpose of this paper, a variety of commercially relevant shot types. Two of the most developed and promising uses of DIA in shot peening are: (1) as an alternative to conventional manual measurement techniques for

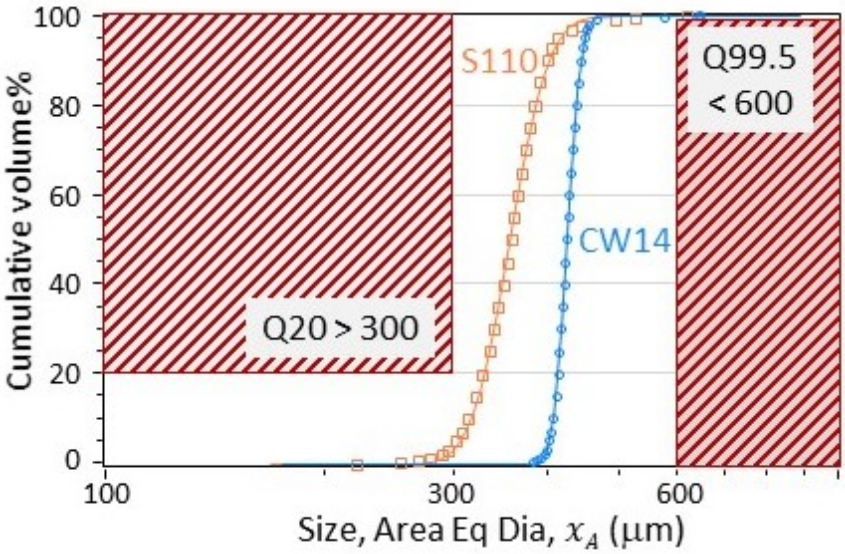

Figure 5.5. Size specification using J2441 adapted to equivalent area diameter. Quantile specifications (Q) describe the allowable size range (non-shaded).

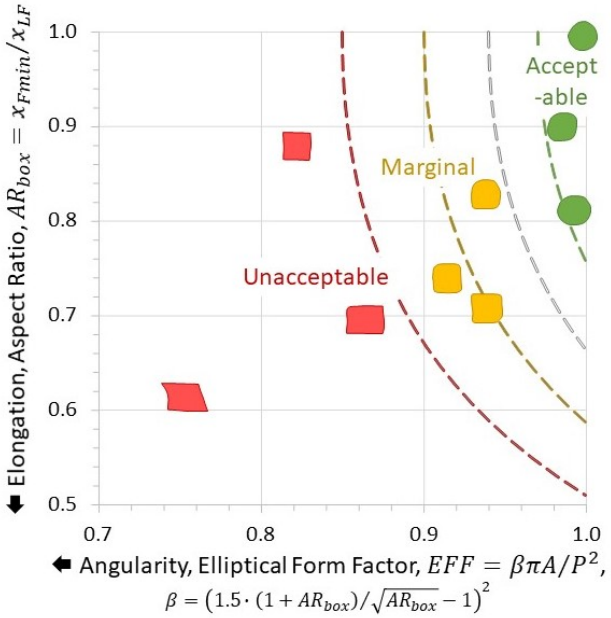

Figure 5.6. Mapping of legacy shape archetypes using orthogonal shape factors. Form factor contours (dashed lines) relate to the proposed limits shown in Figure 5.7.

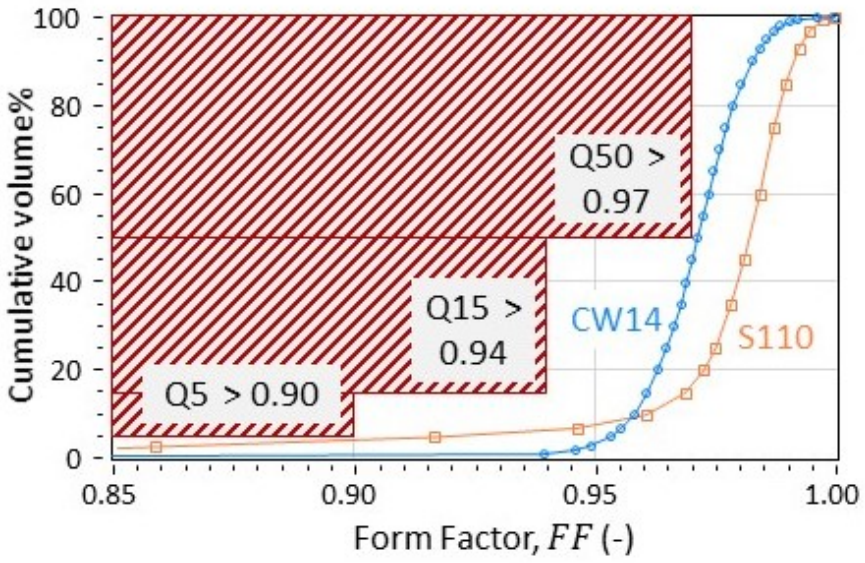

Figure 5.7. Proposed one-sided shape specification format using form factor as a lumped-sum parameter. Quantile specifications (Q) describe the allowable shape range (non-shaded).

analysis and specification of as-manufactured and working-mix media; and (2) as input data to simulate the effects of working-mix dynamics over a variety of shot peening processes.

Acknowledgements

The authors of this paper would like to acknowledge the invaluable contributions made by several individuals and companies, including the efforts of students from the Purdue School of Materials Engineering (MSE) and industrial sponsors of their senior-year projects:

- **Shot characterization (2019–2020)** sponsored by JM Canty: Adrian Gentry, Anna Giesler, Chengyang Zhang, Travis Ziegler.
- **Shot characterization (2020–2021)** sponsored by Electronics Inc., Ervin Inc., Toyo Seiko NA, Saint-Gobain, JM Canty: Michael Thoenen, Torie Lichti, Nikole McPheron, Andrew Babiuk-Murray.

- **Shot Media Characterization and Finite Element Modeling of Peening Operations for Automotive Driveline System Components (2020–2021)** sponsored by American Axle Manufacturing, Engineered Abrasives, JM Canty: Brynna Keelin Kelly, Brandon Keuneke, Genevieve McLaughlin, Haydn Schroader.
- **Specification Development of Shot Media using Image Analysis (2021–2022)** sponsored by Electronics Inc., American Axle Manufacturing, Toyo Seiko NA, JM Canty: Erin McCarthy, Bradley Nance, Sui Xiong Tay, Andrew Thoman.

Finally, the member companies of the Center for Surface Engineering & Enhancement (CSEE), which is operated by Purdue MSE: https://engineering.purdue.edu/MSE/CSEE.

6. Neural Network Enabled Process Flowsheet for Industrial Shot Peening

6.1 Introduction

6.1.1 Artificial Intelligence and Machine Learning for Material Design, Discovery, and Optimization

The development of advanced sensing technologies has opened new avenues for manufacturing process control, enabling dynamic systems that adapt to evolving process conditions. Digital twin frameworks have become central to the vision of Industry 4.0, with the potential to prevent the production of defective components in fatigue-critical applications[50].

Digital twins link process measurements, physics-based models, and control strategies in real time. Within this hierarchy, process flowsheets serve as the organizing structure: they capture the logical and physical sequence of process stages, enabling direct mapping between inputs, underlying deformation mechanisms, and performance outcomes.

Unlike implementations that rely primarily on sensor fusion and data-driven models, flowsheet-based twins emphasize mechanistic understanding of the process. They provide a scalable and interpretable foundation that can be augmented by statistical or physics-based corrections, ensuring that essential processphysics interactions are retained while remaining compatible with real-time monitoring and control[51].

The purpose of this paper is to introduce a reduced-order process flowsheet model of shot peening, a mechanical surface treatment widely used in the aerospace and automotive industries to extend the fatigue life of structural metallic components. A deep learning architecture combining convolutional neural networks with convolutional long short-term memory layers is used to predict residual stress fields from media recycle loop tracking. The model captures the stochastic, multiscale character of the process in a form suitable for integration into digital twin frameworks.

6.1.2 Shot Peening Overview

In shot peening, steel or ceramic particles (typically ∼1 mm in diameter) are propelled at high velocities (∼65 m/s) to bombard metallic components. This process plasticizes the near-surface region and induces compressive residual stresses, which enhance fatigue performance by increasing the applied tensile stress required to initiate or propagate cracks.

The stochastic nature of impact locations and media morphology in shot peening necessitates a careful balance of process parameters to achieve optimal residual stress states and fatigue performance. Świetlicki et al. [52] provide a detailed review of shot peening methodologies and materials effects. These results underscore that shot peening efficacy hinges on a nonlinear, material-specific interplay between blast pressure, media characteristics, and surface coverage.

6.1.3 Opportunities for Media Characterization

Industrial specifications for peening media are rooted in the traditional methods of sieve analysis (size) and qualitative visual inspection (shape), for example MIL-S-13165 originally issued in 1953 [53]. Since then, digital imaging technologies for size and shape characterization have advanced significantly and are now routine for many applications.

Steel shot peening media are commonly either cast or cut-wire, where cast media are made via gas atomization while cut-wire particles are cut from a drawn wire. Both types of media come in multiple grades (often defined by the roundness and hardness of the particles), but have significantly different archetypal shapes, microstructures, and therefore degradation mechanisms. Studies addressing media shape and breakage represent a gap in the literature this report seeks to lay out a reduced order approach for managing. Current work on the dynamic flowsheet employs dynamic image analysis (DIA) (Solidsizer, JM Canty, Lockport, NY) with supplemental data analysis written in LabVIEW (National Instruments, Austin, TX) to fit characteristic distributions for size and shape [3, 46]. Reference Cut-Wire 32 (CW32) working mix media samples were provided by American Axle & Manufacturing (Detroit, MI) and Toyo Seiko North America (South Bend, IN). Shape distributions are

used to calculate an effective radius of curvature on peening impact, while the size affects the mass (i.e., kinetic energy) associated with peening.

6.1.4 Challenges in Numerical Simulation

Finite element analysis is a common tool for modeling of shot peening, where representative volume element approaches simulate a set of particles comprising the average areal mass density impacting a subsection of the surface of a component in a random arrangement[24]. While modern FEM solvers are flexible, including access to contact modules and numerous materials models, the fine mesh necessitated by nonlinear deformation behavior leads to severe computational overhead. In order to accurately capture the full distribution in residual stresses, RVE approaches should ideally scale with operational parameters and the media size. While RVE peening simulations with distributed media sizes have been used in the past[24], each simulation, especially those with sufficient area such that the average mass flux of impacts has reached relative stability, can take hours to run. In contrast, the typical peening process lasts a matter of seconds.

In a recent editorial publication for *The Shot Peener Magazine* [1], we developed a statistical approach for characterizing spatial uniformity in shot peening coverage by modeling impact events as a Poisson point process. This model captured the expected value, variance, and relative standard deviation in impact counts over finite surface regions, incorporating parameters such as media mass flux ($\dot{m}$), part area (A_{part}), peening duration (t_c), and a lognormal media size distribution. However, that treatment focused solely on the statistics of impact placement and did not establish a link between impact field variability and the resulting residual stress fields.

The present work aims to bridge that gap by introducing a computational framework that couples transient process conditions with evolving media morphology and spatial stress predictions. Specifically, we develop:

1. A reduced-order flowsheet model to track media size and shape evolution under wear, breakage, and replenishment cycles.

Table 6.1. Example of size and shape parameters obtained by stretched-exponential fitting of dynamic image analysis data for CW32 media.

Mode	Size: x_A		Shape: AR	
	d_g^*	n	AR^*	n
As-Manufactured	850	15	0.80	10
Conditioned	790	20	0.90	20
Worn	575	10	0.75	6

2. A stochastic coverage simulator that maps operational parameters to spatially distributed impact conditions.

3. A convolutional long short-term memory surrogate trained on high-fidelity FEM data to rapidly predict local residual stresses from sampled impact fields.

Together, these components form a high-speed process flowsheet with potential extensions to a digital twin architecture for process-aware, data-driven prediction of shot peening outcomes.

6.2 Materials and Methods

6.2.1 Flowsheet Architecture

The process flowsheet tracks the circulation of peening media as a dynamic working mix composed of three characteristic modes: (1) as-manufactured, (2) conditioned, and (3) worn. As media are cycled through repeated impacts, they undergo morphological degradation via fracture, abrasion, and plastic deformation. When particles reach a state of excessive wear, they are removed from the system by a classifier and discarded as debris. To maintain system equilibrium, discarded media are replenished with fresh (as-manufactured) particles based on a mass-balance threshold, resulting in a continuous renewal process that stabilizes the working mix distribution over time.

Each mode is further characterized by distinct size and shape distributions, quantified using DIA and parameterized using stretched exponential fits. As shown in Figure 6.1 and

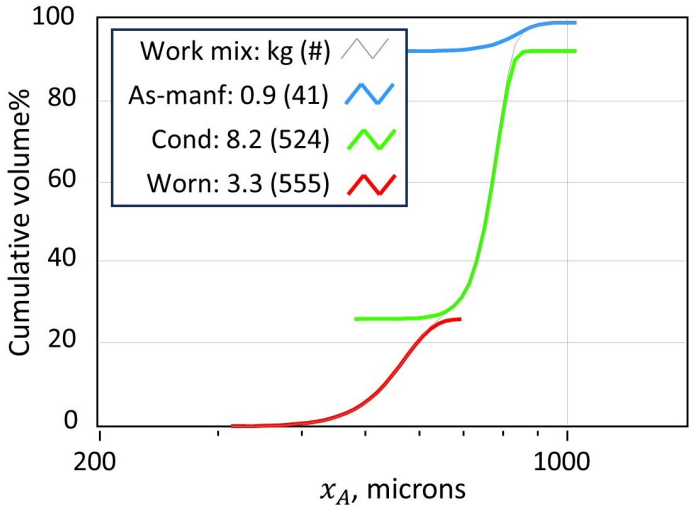

Figure 6.1. Snapshot of the flowsheet simulation showing a mixture of three modes, each with a mass (kg) and average number of impact cycles.

summarized in Table 6.1, the size of media decreases monotonically with wear, while the tightest distributions occur in the conditioned mode. Shape anisotropy, described by aspect ratio (AR), increases in uniformity during the transition from as-manufactured to conditioned media, but becomes broader again in the worn mode due to fracture and distortion.

The working mix model captures this evolving distribution as a three-mode mixture, with the relative contribution of each mode governed by the age of particles in the system. Transitions between modes are described using empirical wear parameters, which may be directly measured using a cyclical-impact apparatus (Ervin Tester, Ervin Inc., Adrian, MI) or inferred through multimodal decomposition of dynamic image analysis (DIA) data from working-mix samples [3]. Each mode is modeled using a Weibull lifecycle function, where the cumulative distribution of transfers, x_T, is given in terms of the characteristic number of impact cycles x^* and a stretching exponent m:

$$x_T = 1 - \exp\left(-\left(\frac{x}{x^*}\right)^m\right).$$

Table 6.2. Example of wear parameters used in the modal transfer function, conditioned CW32 media.

Transfer function	x^*	m
$Manf \rightarrow Cond$	1000	1
$Cond \rightarrow Worn$	4000	4
$Worn \rightarrow Debris$	1600	2

This formulation enables probabilistic modeling of inter-mode transfer, where the likelihood of a particle transitioning out of its current mode increases with cumulative impact exposure.

For example, fresh media introduced into the system begin in the as-manufactured mode. According to the wear parameters in Table 6.2, these particles transition to the conditioned mode with a relatively low characteristic impact count ($x^* = 1000$) and a low stretching exponent ($m = 1$), indicating rapid conditioning of most of the media with a diffuse tail. Once in the conditioned mode, media are more resilient, with a higher durability ($x^* = 4000$). The stretching exponent ($m = 4$) delays the conditioned $\rightarrow$ worn transition, with the effect that conditioned particles tend to remain stable over many impacts before transitioning into the worn state. Worn particles degrade with an intermediate profile before exiting the system as debris, with $x^* = 1600$ and $m = 2$. Overall, the wear parameters define a cycle of degradation, where particles are continuously added, reshaped, and ultimately removed, with the recharge strategy maintaining a dynamic equilibrium across the three modes. This evolving distribution directly influences the impact energy spectrum delivered to the peened surface.

Work Mix Dynamics

The mix of modes is dynamic and depends on the media recharge criteria. The current version of the flowsheet must have a heel of media in a recycle bin. When the mass in that bin drops below a threshold value, a recharge of the as-manufactured media occurs. If the recharge mass is small relative to the total working mix, i.e., frequent and small recharges, the working mix is relatively stable (Figure 6.2) with dampened fluctuations occurring primarily

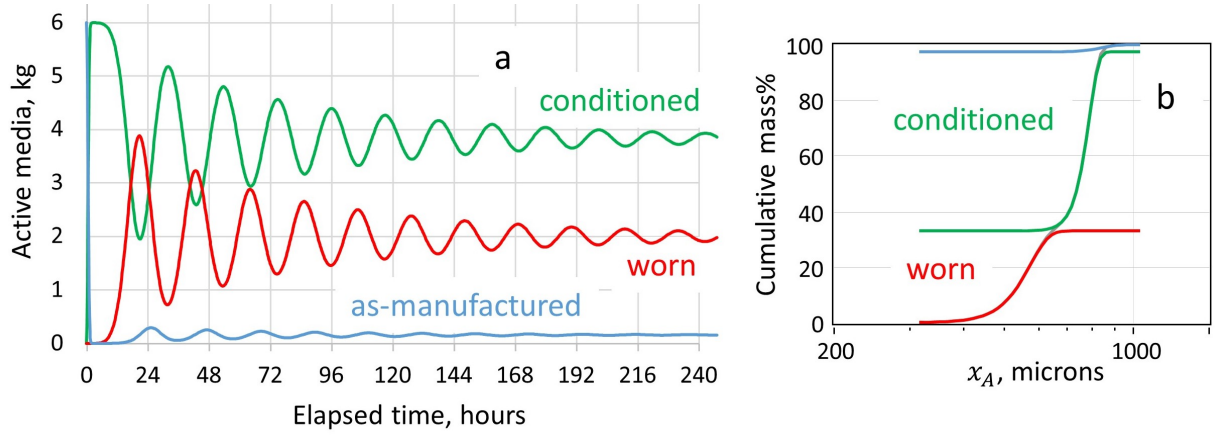

Figure 6.2. Working mix trend based on a lean operating strategy having minimal media inventory with frequent and small recharge quantities: a) time series of flowsheet simulation; b) steady-state convergence.

between the conditioned and worn modes. If the recharge is large and less frequent, the working mix will fluctuate substantially among all three modes. Note, the current flowsheet assumes stable operation of the classifier, i.e., there are no parameters for screening efficiency in the current model.

Archetypal Models for Peening Media

Shape archetypes were used to translate measured shape distributions into effective curvature of peening impacts. Archetypes describe the peening media in terms of their method of manufacture (e.g., cast versus cut wire steel) and level of conditioning. The current work employs an elliptical archetype model for conditioned cut wire, having effective curvature defined by major and minor axes. Note that unconditioned cut wire has sharper curvature at cut-corners, yet these features are relatively short-lived in a steady-state peening process. While quantitative descriptions of detailed curvature features have been enabled in image analysis [6], the simpler elliptical archetype shape model was used for the purpose of flowsheet demonstration [54].

Peening media size and shape effects are selected using a two-step process: (1) random selection of a peening media mass based on the number distribution of the measured area-

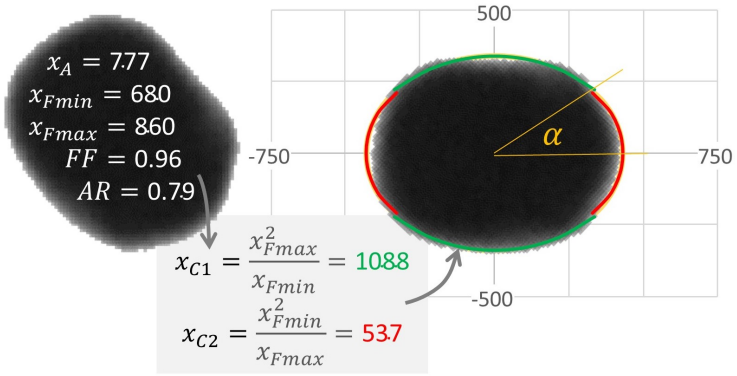

Figure 6.3. Translation from image analysis data to distributed characteristics (x_A, AR) to simplified elliptical archetype having contact curvature. Example is a 2D DIA image of a worn CW32 shot.

equivalent size, $x_A = \sqrt{4A/\pi}$, and (2) random selection of an elliptical curvature based on an archetypal shape model. In this example, the measured aspect ratio distribution, $AR = x_{F\,\min}/x_{F\,\max}$, is used to estimate the curvature of an elliptical archetype. Empirically, we found x_A and AR to be uncorrelated within each mode, allowing independent sampling.

To estimate contact curvature, we approximate each particle as an ellipse with semi-major axis a and semi-minor axis b, related to the area-equivalent size and aspect ratio by:

$$x_A = \sqrt{ab}, \quad AR = \frac{b}{a}, \quad \Rightarrow \quad a = \frac{x_A}{AR^{1/2}}, \quad b = x_A \cdot AR^{1/2}.$$

The principal radii of curvature at the tips of the ellipse are given by:

$$R_a = \frac{b^2}{a} = x_A \cdot AR^{1.5}, \quad R_b = \frac{a^2}{b} = \frac{x_A}{AR^{1.5}},$$

which define the elliptical curvatures used in the model:

$$x_{C1} = \frac{x_A}{AR^{1.5}}, \qquad x_{C2} = x_A \cdot AR^{1.5},$$

corresponding to the sharper (minor-axis tip) and flatter (major-axis tip) regions of the particle, respectively.

The relative probability of a peening contact occurring at x_{C1} versus x_{C2} depends on the ray length from the center of mass to the point of curvature:

$$P_1 = \frac{x_{F\,\min}}{x_{F\,\min} + x_{F\,\max}}, \qquad P_2 = \frac{x_{F\,\max}}{x_{F\,\min} + x_{F\,\max}}.$$

The selection of x_{C1} versus x_{C2} is made by an additional random number call based on these probabilities. Overall, the flowsheet integrates size and shape distributions using a Monte Carlo statistical approach involving three random choices: (1) selection of x_A, (2) selection of AR, and (3) selection of x_C from the directional curvatures. This provides a distribution of discrete peening events, each having an impact energy and contact curvature. When considered as contacts, the curvature model has the effect of broadening the media distribution (Figure 6.4).

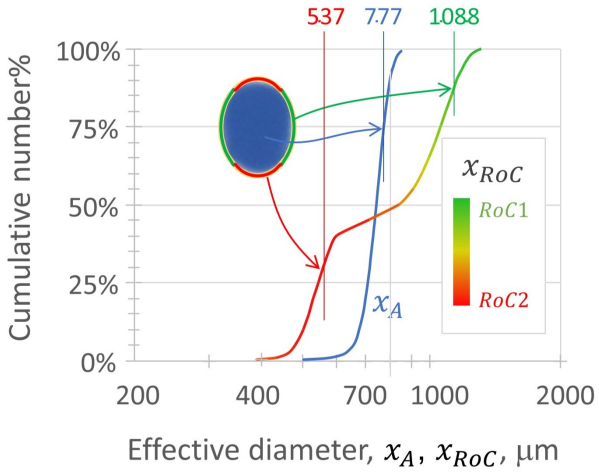

Figure 6.4. Effective contact curvature distribution obtained by applying the elliptical shape archetype to CW32 peening media, x_C, compared with the area-equivalent distribution, x_A.

Effective Peening Impact

Each media-substrate impact is modeled as an effective impact between a spherical shot particle having a radius that is equal to the selected radius of curvature, yet having a mass that is consistent with the actual shot size. The actual mass is based on the material density, e.g., $7.8 g/mL$ for CW32 media, multiplied by the volume of the shot particle obtained from its projected area, A, measured by DIA, $V = (4/3) \cdot A^{1.5}/\sqrt{\pi}$. To maintain this mass with a sphere that was adjusted to a different radius of curvature, an effective density ratio is applied, $DR = \rho_{eff}/\rho_{shot} = (x_A/x_C)^3$. When $x_C > x_A$, the effective density ratio < 1; when $x_C < x_A$, the effective density ratio > 1 (Figure 6.5). This suggests a broadening of the impact stress distribution, with large-curvature impacts having relatively broader contact area and lower impact stress compared to small-curvature impacts.

Peening Coverage

The flowsheet simulation generates periodic snapshots of peening coverage based on the prescribed media mass flow rate, treated surface area, and a defined coverage time interval.

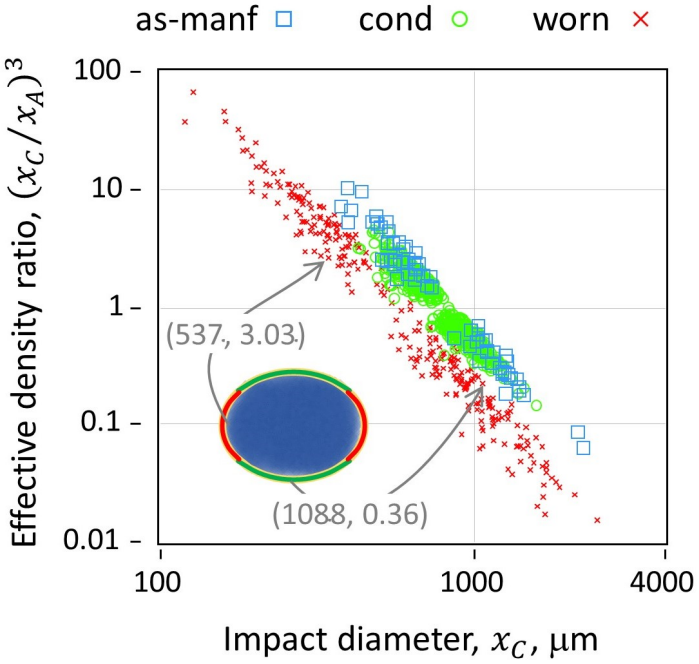

Figure 6.5. Effective density ratio used to maintain the effective kinetic energy (i.e., mass) of media impacting with adjusted curvature (i.e., shape.), using same snapshot as Figure 6.1. Inset is an example of the elliptical shape archetype.

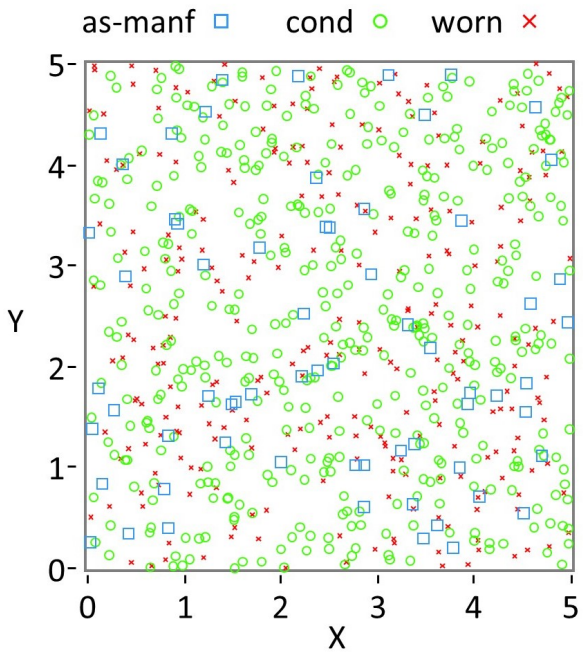

Figure 6.6. Coverage map of a representative volume element by media type, using same snapshot as Figure 6.1.

Impacts contributing to the average areal mass density are sampled over a representative surface element, with impact locations modeled using randomized (x, y) coordinates.

The coverage map is displayed as point contacts by mode within the work mix distribution (Figure 6.6). The data shown in Figure 6.5 provide initial conditions for more detailed residual stress calculations via Finite Element Modeling (FEM) and reductions thereof, essentially correlating the distribution of paired input parameters (x_A, x_C, DR) to a resultant stress field induced by the random coverage (Figure 6.6) of said impacts.

6.2.2 FEM-Based Convolutional Neural Network

RVE Finite Element Analysis

Snapshots of peening coverage generated by the flowsheet (Figure 6.6) were used as initial conditions for finite element simulations. These coverage maps, defined by sam-

Table 6.3. Fixed operational constants used in the peening simulation framework. A_{part} denotes the peened surface area, t_c is the duration of a full peening cycle, and θ is the angle of incidence between the particles and RVE.

Parameter	Value
A_{part} (mm^2)	49100
t_c (s)	30
θ (°)	90

Table 6.4. Range of operational parameters used to generate impact conditions for RVE simulations. The mass flow rate governs cumulative areal mass density, while the impact velocity influences particle kinetic energy.

Parameter	Lower Bound	Mean Value	Upper Bound
Mass Flow Rate (kg/s)	0.04725	0.0945	0.189
Impact Velocity (m/s)	45	65	85

pled impact positions and media descriptors (x_A, x_C, DR), provide the basis for correlating stochastic impact fields with resultant residual stress states.

Each FEM simulation drew coverage maps from the flowsheet while varying mass flow rate and impact velocity within the ranges given in Table 6.4, with fixed constants summarized in Table 6.3. The full factorial design yielded 9 simulations. Radii of curvature were assigned from elliptical archetypes based on measured aspect ratios. Shots were treated as rigid, impacts were temporally staggered, and a node-to-surface contact model without friction was applied.

Table 6.5. Elasto-plastic material properties for Johnson–Cook hardening model of SAE 1070 Almen strip steel [27].

Param.	E (MPa)	ν	A (MPa)	B (MPa)	n	C
Value	210000	0.31	1408	600	0.234	0.0134

Param.	m	$\dot{\varepsilon}_0$	T_0 (K)	T_M (K)
Value	1	1	298	1793

Johnson–Cook isotropic hardening was used to model the elasto-plastic response of the SAE 1070 Almen strip material, as described by Ghanbari *et al.* [27] (Table 6.5). Thermal effects were not simulated; peening was treated purely as a cold-working process.

ABAQUS Explicit 2019 [55] was used to run the peening simulations. A rectilinear mesh of C3D8R elements made up the bulk of the RVE. The simulated RVE was $5mm \times 5mm \times 2mm$ in size, with a layer of infinite (CIN3D8) elements at its boundary and base. Grid independence on the basis of total strain energy was observed across all combinations of impact kinetics with a surface element size of $20\mu m \times 20\mu m \times 20\mu m$, in-line with guidance by Wang et al. [34], who observed grid independence with a surface element size of 1/10-th the dimple diameter. For computational efficiency, a biased mesh was employed such that elements farther from the impact surface were larger, with a maximum element size of $20\,\mu\text{m} \times 20\,\mu\text{m} \times 100\,\mu\text{m}$ at the base of the substrate.

For this report, we focus on the mean in-plane residual stress, defined as

$$\sigma_{\text{mean}} = \tfrac{1}{2}(\sigma_{11} + \sigma_{22}),$$

because it is translationally and rotationally invariant relative to the measurement plane and directly related to the pressure holding a surface crack closed. Future work may also consider the normal Cauchy stress in the X or 11-direction (σ_{11}), given its direct analogy to stresses measured with X-ray diffraction [56, 57], which remains a common quality control metric in industrial shot peening practice. In this work we restrict attention to normal impacts, where the stress state is approximately isotropic within the surface plane; however, off-angle cases may introduce anisotropy into the residual stress field and necessitate directionally dependent descriptors.

LSTM Convolutional Neural Network FEM Surrogate

In our previous work [2], we used spectral correction methods to describe residual stress field structure based on reduced-order micromechanical solutions. That approach did not account for impact order, instead relying on linear superposition of impacts. At low impact densities, where overlaps are rare, the model successfully reproduced both the

pointwise stress field and its spatial correlation structure. At high impact densities, however, the reduced-order model simplified to a stochastic field with the same mean, variance, and correlation structure as the FEM predictions, but without the ability to resolve pointwise details. To address this limitation, the present work treats the evolution of stresses and surface topography in the shot peening system as a history-dependent process.

We developed an impact-orderaware ConvLSTM surrogate model trained on a set of representative finite element simulations, enabling fast prediction of residual stress fields under arbitrary peening conditions. Training inputs were constructed as spatial energy maps using an Eshelby inclusion analogy, as explored in our recent work [2]. Each impacting particle was represented by a 2D projection whose footprint was parameterized by the effective contact radius derived from the selected contact curvature rather than the full geometric projection. Within this footprint, the particle's kinetic energy was distributed uniformly; points outside received zero contribution. Thus, each impact was encoded as a localized scalar energy inclusion capturing the combined effects of particle size, shape, and velocity:

$$E_{\mathrm{i}}(x,y) = \begin{cases} \dfrac{1}{\pi r_{\mathrm{i}}^2}\left(\dfrac{1}{2}m_{\mathrm{i}}v_{\mathrm{i}}^2\right), & \text{if } (x-x_{\mathrm{i}})^2+(y-y_{\mathrm{i}})^2 \le r_{\mathrm{i}}^2, \\ 0, & \text{otherwise,} \end{cases}$$

where m_{i} and v_{i} are the mass and velocity of the i^{th} particle, and r_{i} is the effective contact radius used for input construction.

FEM-predicted stress fields were decomposed into local prediction windows to provide training targets for the surrogate model. Each target was defined as a 16×16 pixel patch of the in-plane residual stress field, corresponding to a neighborhood of approximately 320×320 $\mu\mathrm{m}^2$ at the FEM mesh resolution. Predicting continuous patches simultaneously, rather than individual points, improved the model's ability to reproduce coherent structures associated with surface plasticity and reduced the numerical model's tendency to minimize variance across the field. This window size was chosen to balance spatial resolution with computational efficiency, while remaining large enough to capture the stress gradients and local interactions among multiple adjacent impacts.

The corresponding model input was an ordered sequence of impact "frames," each of size 36×36 pixels, encoding the spatial distribution of particle energy deposition across successive timesteps. The larger input frame ensured that the receptive field encompassed the surrounding impact environment beyond the target window, allowing the network to capture influential impacts just outside the prediction region.

Table 6.6. Neural network architecture mapping $T\times36\times36\times1$ input frames to a $16\times16\times1$ stress patch.

Layer	**Output Shape**	**Act.**	**Params**
Input	$(T, 36, 36, 1)$	–	0
TD Conv2D (3×3,16,s2)	$(T, 18, 18, 16)$	gelu	160
TD Conv2D (3×3,32,s2)	$(T, 9, 9, 32)$	gelu	4,640
ConvLSTM2D (48,3×3,seq)	$(T, 9, 9, 48)$	tanh/sig.	138,432
ConvLSTM2D (64,3×3)	$(9, 9, 64)$	tanh/sig.	258,304
Conv2D (3×3,64)	$(9, 9, 64)$	gelu	36,928
UpSample (2×)	$(18, 18, 64)$	–	0
Conv2D (3×3,64)	$(18, 18, 64)$	gelu	36,928
Conv2D (3×3,32)	$(18, 18, 32)$	gelu	18,464
Conv2D (3×3,32,valid)	$(16, 16, 32)$	gelu	9,248
Conv2D (1×1,1)	$(16, 16, 1)$	linear	33
Total	–	–	**503,137**

Our network was implemented in TensorFlow [58]. The architecture, summarized in Table 6.6, was designed to balance temporalspatial modeling capacity with computational efficiency. A per-frame encoder reduced each 36×36 impact frame to progressively compressed feature maps (18×18 and 9×9), using `gelu` activations to enhance convergence stability without explicit normalization. These encoded sequences were passed to stacked ConvLSTM layers, which captured both intra-frame spatial correlations and inter-frame temporal dependencies. The decoder then upsampled the 9×9 latent representation back to a 16×16 output window, using bilinear interpolation followed by convolutional refinement to reconstruct fine-scale detail. A final 1×1 convolution produced the predicted residual stress field. This encoderConvLSTMdecoder formulation enabled mappings from evolving impact fields to localized stress responses without the computational burden of full-field predictions.

We employed a custom loss function that combined the mean squared error (MSE) of the 16×16 pixel^2 stress patches with the difference in variance between the ML predictions

and the FEM targets. This formulation rewarded point-wise accuracy while penalizing the model's tendency to underestimate field-level variance. Both components of the loss are dimensionally consistent (GPa^2). The dataset was partitioned into a 75:25 trainingtest split. Training used the AdamW optimizer with an initial learning rate of 6×10^{-4}, progressively reduced to 1.5×10^{-4} as losses plateaued. After 42 epochs, the model achieved a final MSE of 0.0443 GPa^2 and an average variance difference of 0.0113 GPa^2 on the test set.

6.3 Results

6.3.1 Patch-Level Accuracy

Figure 6.7a summarizes parity statistics for 200,000 randomly sampled pixels from the test set. Relative to an overall mean stress magnitude of 0.818 GPa, the model achieved a mean absolute error (MAE) of 0.1453 GPa. The fitted regression slope ($a = 0.837$) and intercept ($b = -0.124$ GPa) indicate a tendency to overpredict the magnitude of low-stress regions. Nevertheless, the model generalizes well to the test data and successfully reproduces FEM-predicted stress concentrations with magnitude greater than 2 GPa, which occur in 0.1% of sampled pixels.

Figure 6.7b further examines performance at the per-pixel level. Although all pixels exhibited a mean absolute error below 0.200 GPa, those located on the edges of the prediction window performed worse than those at the center. Overall, there was little variation in accuracy within the central 12×12 region of the prediction window.

6.3.2 Structural Accuracy and Generalization Across Conditions

We used the central 12×12 region of the prediction window to tile 5×5 mm^2 RVE stress fields and assess the model's ability to reproduce correlation structures across scales larger than a single tile. Figure 6.8 compares stress fields for the baseline case and two extreme conditions of the full factorial design (low flow rate with low velocity, and high flow rate with high velocity). While portions of these fields contributed patches during training, the model never observed complete fields; tiling therefore provides a test of generalization

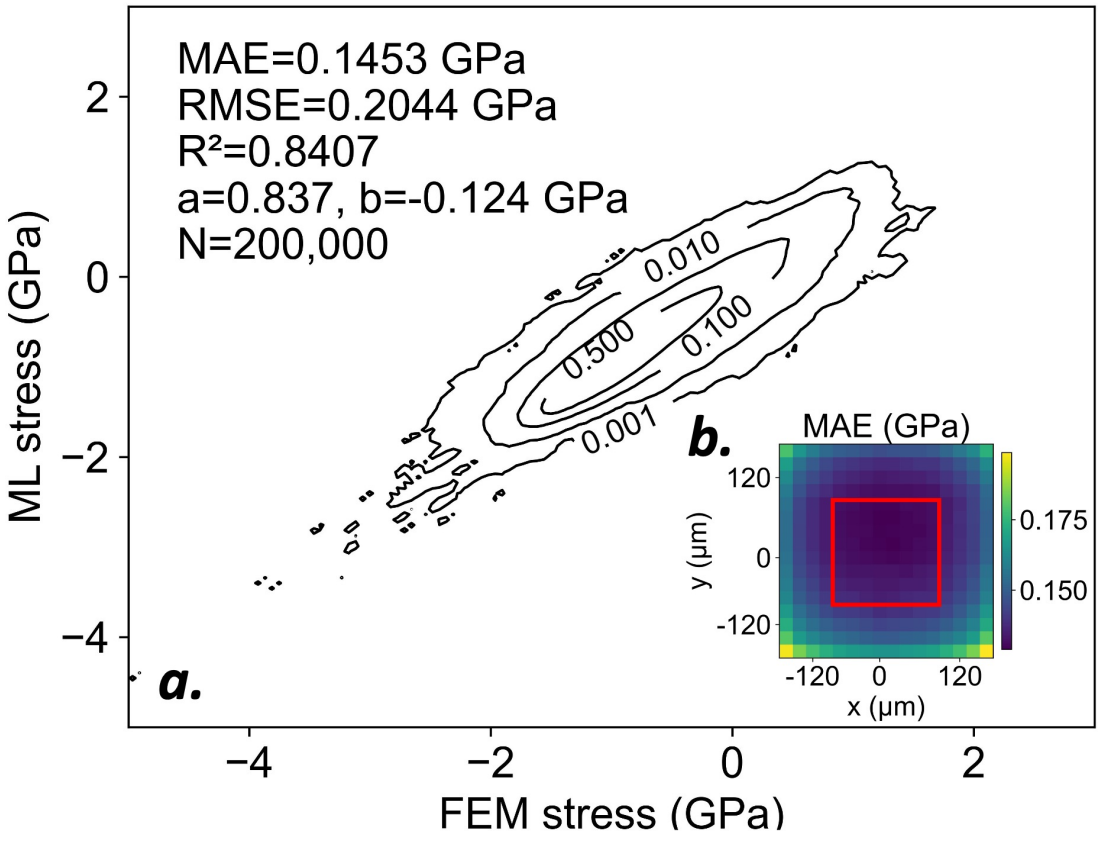

Figure 6.7. a) Contour parity plot comparing FEM-computed and ML-predicted stresses at the pixel level. b) Per-pixel mean absolute error (MAE) evaluated across the prediction window. Central 12 × 12 region marked in red.

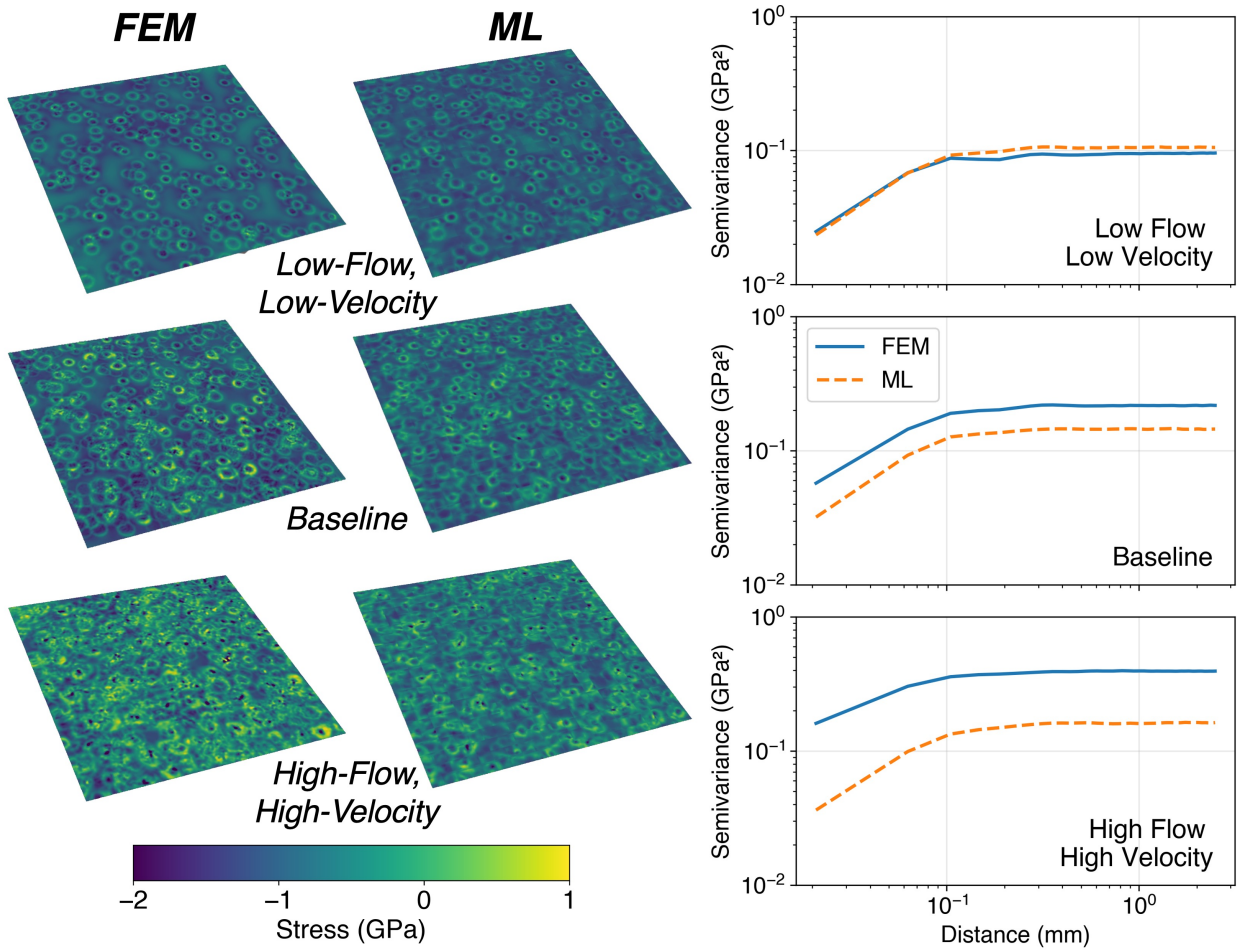

Figure 6.8. Comparison of FEM and ML-predicted stress fields tiled from 12×12 patches to form 5×5 mm^2 RVEs. Left: representative stress fields for baseline and extreme cases. Right: corresponding variograms showing semi-variance as a function of separation distance.

beyond patch-level memorization. These visualizations demonstrate that the model captures field-level organization under contrasting process conditions.

Variograms on the right of Figure 6.8 depict the expected squared difference (semi-variance) of stress values separated by a given distance. The plasticized region beneath an impact forms a coherent structure within the stress field, where nearby elements exhibit similar stresses. Consequently, semi-variance increases with separation distance until reaching a plateau that reflects the characteristic extent of the plasticized zone. Beyond this range,

stress fluctuations appear largely stochastic and spatial organization decays. The horizontal asymptote approached at large separations corresponds to the variance of the stress field.

Table 6.7. Mean and standard deviation (STD) of ML-predicted and FEM-computed residual stresses.

Condition	Mean [GPa]		STD [GPa]	
	ML	FEM	ML	FEM
Low flow / low velocity	-0.953	-0.964	0.325	0.309
Baseline	-0.824	-0.853	0.381	0.466
High flow / high velocity	-0.622	-0.509	0.403	0.628

Table 6.7 directly compares field-level means and standard deviations across the three tested operating conditions. Increasing flow rate and impact velocity intensifies surface plasticity and penetration depth, which in turn decreases the mean compressive stress magnitude at the surface while increasing variability. Similar phenomena have been reported separately by Klump et al. [59] and Wang et al. [60].

The ML model best reproduces the low-flow rate case, accurately capturing the mean stress, variance scaling, and correlation structure. In this regime, impact dimples form a network of connected tensile rings due to localized upheaval of the surface. The relatively sparse coverage allows these features to remain intact, and they are well reproduced by the ML model. Accounting for impact sequence is critical here, since the most recent impact deforms and reorganizes the surface beneath.

In the high-flow rate case, overlapping impacts severely deform portions of the surface, pushing the limits of both FEM and ML predictions. The network of impact dimples is largely diminished, and—as reflected by the shallower slope of the variograms in the correlated region—both fields begin to resemble random stress distributions.

The baseline case represents an intermediate condition, with impact structures that are partially preserved but also subject to overlap and smoothing. The ML model closely matches the FEM-predicted mean value (-0.824 GPa vs. -0.853 GPa). While the ML model tends to underestimate variance at higher impact coverages, it retains 82% of the FEM-predicted standard deviation in the baseline condition.

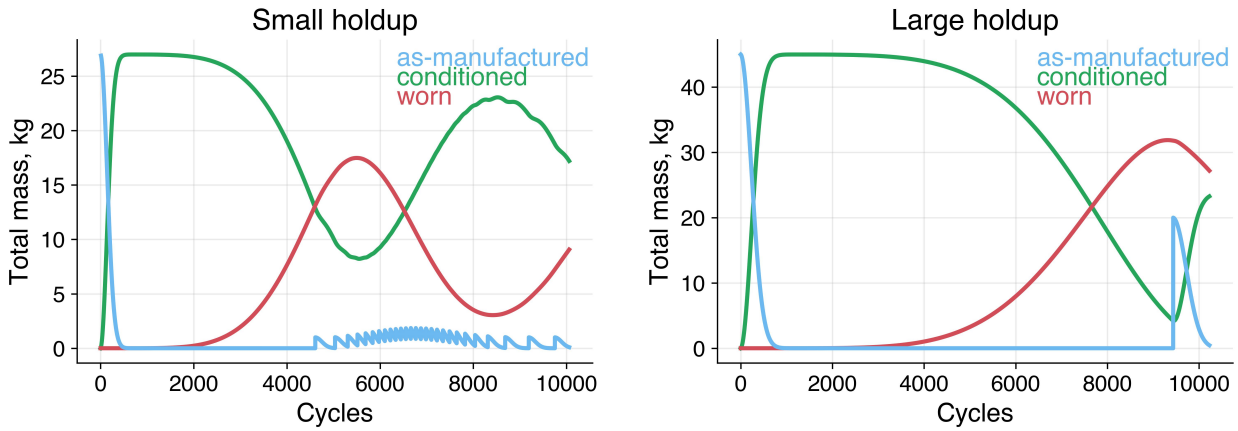

Figure 6.9. Media recharge strategies for small (20 kg heel, 1 kg recharge) and large (30 kg heel, 20 kg recharge) holdup cases.

Overall, the ML model consistently preserves correlation length scales, indicating that it captures the essential spatial organization of the stress field. Combined with the strong parity performance against FEM data, this fidelity is sufficient for the model to serve as a reduced-order process monitoring tool. In particular, it enables exploration of stress field dynamics under baseline conditions, where cycles of media recharge and breakdown drive temporal evolution of surface morphology and residual stress distributions.

6.3.3 Temporal Dynamics

Consider two media recharge strategies shown in Figure 6.9. In both cases, approximately 5 kg of media circulate through the blast loop each cycle, while the remainder resides in the holdup hopper. In the small-holdup case, the process is initialized with 26 kg of media in total. The holdup is maintained at a 20 kg threshold, with 1 kg of new media added whenever the holdup mass falls below this limit, resulting in frequent, gradual renewals after an initial conditioning period. In the large-holdup case, the process begins with 45 kg of as-manufactured media in total. Here, the holdup is maintained at 30 kg, and 20 kg are added once that threshold is reached, producing less frequent but more substantial renewal events.

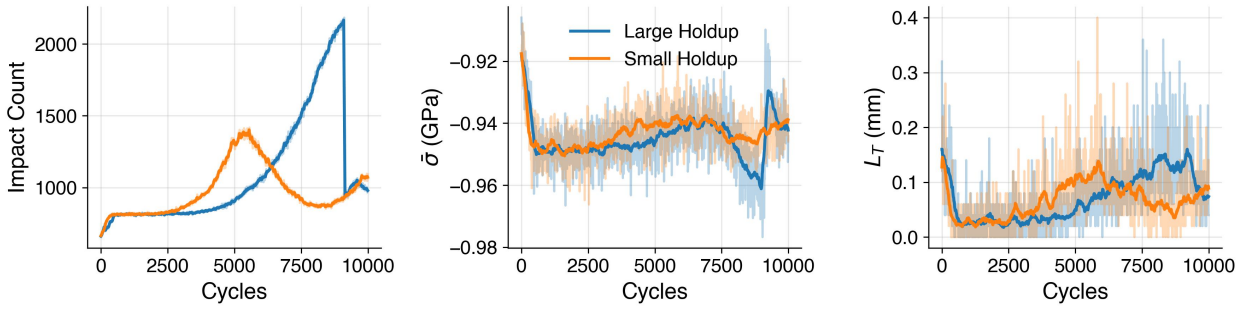

Figure 6.10. Evolution of average stress ($\bar{\sigma}$), maximum tensile path length (L_T), and impact count over 10,000 cycles for small and large holdup cases. Transparent traces show raw simulation outputs recorded every 10 cycles, while dark lines indicate 25-point rolling averages for clarity.

We simulated 10,000 peening cycles, taking RVE impact map samples every 10 cycles and passing them through the ML model. Figure 6.10 summarizes trends in average stress ($\bar{\sigma}$), maximum tensile path length (L_T), and impact count. The tensile path length, L_T, quantifies the spatial continuity of tensile regions within the predicted surface stress field. It is computed using an 8-connected flood-fill search [61] with periodic boundary conditions, which systematically traces the longest contiguous cluster of tensile elements ($\sigma > 0$) across the surface. This approach captures not only the magnitude but also the geometric persistence of tensile features–analogous to flaw-like regions that can facilitate crack initiation or locally reduce compressive effectiveness. Stable, confined tensile paths reflect uniform and well-contained plastic deformation, whereas sporadic increases in L_T mark rare events in which extended tensile bands emerge, signaling potential degradation in peening quality and increased susceptibility to crack growth.

At startup, both strategies are identical: as-manufactured media transition into the more resilient conditioned state, accompanied by a ~ 30 MPa shift toward more compressive surface stress. Higher impact counts and smaller, more uniform dimples from the reduced particle size shorten the maximum tensile path length (L_T), indicating a more homogeneous and spatially confined stress field.

The smaller media mass in the small holdup case accelerates the onset of the worn state–around 2000 cycles versus 3000 in the large holdup case. Impact counts continue to rise, but increased shape anisotropy in the worn mode promotes the formation of extended tensile features, causing the maximum tensile path length (L_T) to increase even as $\bar{\sigma}$ remains relatively stable.

In the small holdup trial, the worn mode dominates at 4500 cycles, coinciding with the start of frequent recharges. Each recharge of as-manufactured media replenishes the conditioned mode, establishing a relatively stable renewal cycle and reducing both impact count and L_T.

In the large-holdup case, worn media is predominant prior to recharge. Impact counts more than double relative to the early conditioned state, and L_T rises accordingly. Upon replenishment, 20 kg of fresh media is added to 30 kg of worn, sharply reducing the impact count. For approximately 200 cycles, the combination of worn and as-manufactured particles–both exhibiting high shape anisotropy–drives L_T to a maximum and induces a ~ 25 MPa shift toward less compressive $\bar{\sigma}$. In some instances, L_T values exceeding 0.3 mm were observed–on the order of a particle radius. Such events represent measurable drops in peening process quality, increasing the likelihood of flaw formation and localized tensile persistence at the surface.

6.4 Conclusions

These scenarios serve as a proof of concept for how the model can capture the coupled evolution of media states, impact statistics, and stress variability under different operational strategies. Beyond reproducing qualitative trends, the framework demonstrates potential as a tool for evaluating alternative recharge policies and linking them directly to surface integrity outcomes.

The high-resolution stress fields produced by the ML model provide a basis for alternative quality control metrics beyond mean-field diffraction-based experiments. In particular, future work investigating relative variability and characteristic correlation length effects on crack propagation dynamics could seek to establish quantitative relationships between stress

field heterogeneity and fatigue performance. Such relationships would enable the model to serve not only as a predictive tool but as a foundation for performance-based process qualification.

When coupled with in-process sensing of media condition and impact statistics, this framework could bridge model prediction and experiment to form the foundation of a full digital twin for shot peening. A key next step lies in informing media wear and velocity dynamics through direct measurement. Dynamic image analysis (DIA) can provide real-time distributions of particle size and shape to constrain media evolution, while high-speed velocimetry can characterize the temporal dynamics of impact energy. Integrating these data streams into the flowsheet would enable a continuously calibrated model capable of adaptive process control and predictive maintenance in industrial operation.

6.5 Data Availability

The simulation codes used in this study are openly available on GitHub at: https://github.com/feltner515/ML_Flowsheet. Due to the large size of the raw finite element and machine learning datasets, these data are not publicly archived but are available from the corresponding author upon reasonable request.

7. Summary and Future Work

7.1 Summary of Contributions

This dissertation explores stochasticity in the context of industrial shot peening, positing a quantifiable structure underlying the apparent randomness of stress fields and surface finishes. We describe that structure through theory, experimental analysis, and process simulation. Additionally, when treated statistically rather than empirically, it reveals a clear link between process parameters, material response, and surface integrity.

Across the chapters, the work follows a continuous thread:

1. Establish a statistical description of impact coverage and material input to the surface.
2. Connect those stochastic inputs to spatially heterogeneous residual stress fields using micromechanics and spectral analysis.
3. Demonstrate that the same organization appears experimentally in measured surface topography.
4. Integrate analytical, numerical, and experimental components into a process flowsheet and surrogate model suitable for digital twin applications.

Collectively, these results describe shot peening as a structured stochastic process. Coverage, media evolution, and residual stress formation denote statistically coupled subsystems governed by measurable distributions.

In practical terms:

- Coverage follows Poisson scaling with process time and media flux.
- Residual stress fields exhibit reproducible spectral organization tied to inclusion-scale mechanics.
- Surface morphology reflects the same organization in measurable frequency bands.
- Media degradation drives much of the process variability but follows quantifiable lifecycle statistics.

- Reduced-order models map stochastic impact histories to interpretable process-quality indicators.

7.2 Future Work

7.2.1 Closed-Loop Sensing and Control

Integrating DIA and high-speed velocimetry into the flowsheet would allow direct measurement of media condition and impact velocity in real time. Those measurements could update the model state continuously, closing the loop between sensing and prediction. Adaptive control of blast parameters and recharge strategy could then maintain target residual stress and correlation length, enabling process qualification to move from post-process verification to in-process control.

7.2.2 Geometry, Angle, and Anisotropy

Extending the framework to oblique impacts and complex geometries remains an open challenge. Incorporating ellipsoidal inclusion analogies and vector-valued surrogates will allow prediction of directional stress anisotropy–critical for components such as gears, turbine blades, and splines where surface curvature and angle strongly influence the stress field.

7.2.3 Constitutive Links Between Spectral Fabric and Material Response

The observed scaling between spectral invariants (J_2, J_1) suggests that the spectral fabric may encode material-specific plastic response. Correlating these invariants with constitutive parameters such as hardening coefficients or strain-rate sensitivity could yield material fingerprints measurable directly from spectral data, bridging deformation mechanics and process metrology.

7.2.4 Process Qualification and Fatigue Metrics

The digital twin architecture enables new qualification metrics beyond arc height or near-surface stress. Quantities such as correlation length, field variance, or maximum tensile

path continuity (L_T) offer early indicators of process drift and potential fatigue risk. Defining statistical thresholds for these metrics would enable predictive maintenance and process audits based on physics-informed indicators rather than scalar summaries.

REFERENCES

[1] L. Feltner and P. Mort, "Probabilistic Assessment of Shot Peening Impact Coverage," *The Shot Peener magazine*, vol. 39, no. 2, 2025. [Online]. Available: https://www.shotpeener.com/library/detail.php?anc=2025011.

[2] L. Feltner and P. Mort, *Spectral Fabric of Stochastic Residual Stress Fields*, Sep. 10, 2025. DOI: 10.21203/rs.3.rs-7466816/v1. [Online]. Available: https://doi.org/10.21203/rs.3.rs-7466816/v1.

[3] L. Feltner, M. Gruninger, T. Canty, and P. Mort, "Characterization of Particle Size and Shape Distributions for Shot Peening Media," *The Shot Peener*, vol. Spring, 2024.

[4] L. Feltner and P. Mort, "Neural network enabled process flowsheet for industrial shot peening," *Preprints*, 2025, Posted Date: 17 October 2025. DOI: 10.20944/preprints202510.1315.v1.

[5] L. Feltner, E. Korte, D. F. Bahr, and P. Mort, "Particle size and shape analyses for powder bed additive manufacturing," *Particuology*, 2023.

[6] L. Feltner, D. Stumpf, and P. Mort, "On the use of the Fourier transform to determine contact curvature distributions in additive manufacturing powders," *Powder Technology*, vol. 453, p. 120 618, 2025, ISSN: 0032-5910. DOI: 10.1016/j.powtec.2025.120618. [Online]. Available: https://www.sciencedirect.com/science/article/pii/S0032591025000130.

[7] A. Wald, "On cumulative sums of random variables," *The Annals of Mathematical Statistics*, vol. 15, no. 3, pp. 283–296, 1944.

[8] S. M. Ross, *Stochastic Processes*. New York: Wiley, 1996.

[9] D. A. Blackwell and M. A. Girshick, *Theory of games and statistical decisions*. Courier Corporation, 1979.

[10] B. Kelly, B. Keuneke, G. McLaughlin, and H. Schroader, *Shot Media Characterization and Finite Element Modeling of Peening Operations for Automotive Driveline System Components*, May 2021.

[11] T. Mura, *Micromechanics of Defects in Solids*. Springer Science & Business Media, 2013.

[12] T. Mori and K. Tanaka, "Average stress in matrix and average elastic energy of materials with misfitting inclusions," *Acta metallurgica*, vol. 21, no. 5, pp. 571–574, 1973.

[13] Y. Benveniste, "A new approach to the application of Mori-Tanaka's theory in composite materials," *Mechanics of materials*, vol. 6, no. 2, pp. 147–157, 1987.

[14] Y. Huang, K. X. Hu, X. Wei, and A. Chandra, "A generalized self-consistent mechanics method for composite materials with multiphase inclusions," *Journal of the Mechanics and Physics of Solids*, vol. 42, no. 3, pp. 491–504, 1994.

[15] K. Ken-Ichi, "Distribution of directional data and fabric tensors," *International journal of engineering science*, vol. 22, no. 2, pp. 149–164, 1984.

[16] M. A. S. Torres and H. J. C. Voorwald, "An evaluation of shot peening, residual stress and stress relaxation on the fatigue life of AISI 4340 steel," *International Journal of Fatigue*, vol. 24, no. 8, pp. 877–886, 2002.

[17] D. Gallitelli *et al.*, "Simulation of shot peening: From process parameters to residual stress fields in a structure," *Comptes Rendus. Mécanique*, vol. 344, no. 4–5, pp. 355–374, 2016.

[18] K. L. Johnson, "One hundred years of Hertz contact," *Proceedings of the Institution of Mechanical Engineers*, vol. 196, no. 1, pp. 363–378, 1982.

[19] H. Hertz, "Über die Berührung fester elastischer Körper," *Journal für die reine und angewandte Mathematik*, vol. 92, pp. 156–171, 1881.

[20] A. S. Franchim, V. S. de Campos, D. N. Travessa, and C. de Moura Neto, "Analytical modelling for residual stresses produced by shot peening," *Materials & Design*, vol. 30, no. 5, pp. 1556–1560, 2009.

[21] H. Y. Miao, S. Larose, C. Perron, and M. Lévesque, "An analytical approach to relate shot peening parameters to Almen intensity," *Surface and Coatings Technology*, vol. 205, no. 7, pp. 2055–2066, 2010.

[22] A. Poozesh and B. Arezoo, "An analytical model for predicting residual stress in shot peening with strain energy method," *Scientific Reports*, vol. 14, no. 1, p. 19 826, 2024.

[23] S. M. Hassani-Gangaraj, K. S. Cho, H.-J. Voigt, M. Guagliano, and C. A. Schuh, "Experimental assessment and simulation of surface nanocrystallization by severe shot peening," *Acta Materialia*, vol. 97, pp. 105–115, 2015.

[24] H. Y. Miao, S. Larose, C. Perron, and M. Lévesque, "On the potential applications of a 3D random finite element model for the simulation of shot peening," *Advances in engineering software*, vol. 40, no. 10, pp. 1023–1038, 2009.

[25] J. D. Eshelby, "The determination of the elastic field of an ellipsoidal inclusion, and related problems," *Proceedings of the royal society of London. Series A. Mathematical and physical sciences*, vol. 241, no. 1226, pp. 376–396, 1957.

[26] J. N. Goodier, "Concentration of stress around spherical and cylindrical inclusions and flaws," *Journal of Applied Mechanics*, vol. 55, no. 1, pp. 39–44, 1933.

[27] S. Ghanbari and D. F. Bahr, "Predictions of decreased surface roughness after shot peening using controlled media dimensions," *Journal of Materials Science and Technology*, vol. 58, pp. 120–129, 2020. DOI: 10.1016/j.jmst.2020.03.075. [Online]. Available: https://doi.org/10.1016/j.jmst.2020.03.075.

[28] SAE International, *SAE J442: Test Strip, Holder, and Gage for Shot Peening*, SAE International, 2017. [Online]. Available: https://www.sae.org/standards/content/j442_201710/.

[29] SAE International, *SAE J443: Procedures for Using Standard Shot Peening Test Strip*, SAE International, 2010. [Online]. Available: https://www.sae.org/standards/content/j443_201005/.

[30] M. Shinozuka and G. Deodatis, "Simulation of stochastic processes by spectral representation," 1991.

[31] C. Villani *et al.*, *Optimal Transport: Old and New*. Springer, 2008, vol. 338.

[32] Dassault Systèmes Simulia Corp., *Abaqus User's Manual*, 2021st ed. Providence, RI: Dassault Systèmes, 2021.

[33] S. N. Chiu, D. Stoyan, W. S. Kendall, and J. Mecke, *Stochastic Geometry and Its Applications*. John Wiley & Sons, 2013.

[34] Z. Wang, M. Shi, J. Gan, X. Wang, Y. Yang, and X. Ren, "The effects of shot distance and impact sequence on the residual stress field in shot peening finite element model," *Metals*, vol. 11, no. 3, p. 462, 2021.

[35] E. Maleki, S. Bagherifard, M. Bandini, and M. Guagliano, "Surface post-treatments for metal additive manufacturing: Progress, challenges, and opportunities," *Additive Manufacturing*, vol. 37, p. 101 619, 2021, ISSN: 2214-8604. DOI: https://doi.org/10.1016/j.addma.2020.101619. [Online]. Available: https://www.sciencedirect.com/science/article/pii/S221486042030991X.

[36] B. Zhao, J. Song, L. Xie, Z. Hu, and J. Chen, "Surface roughness effect on fatigue strength of aluminum alloy using revised stress field intensity approach," *Scientific Reports*, vol. 11, p. 19 279, 2021. DOI: 10.1038/s41598-021-98858-0. [Online]. Available: https://doi.org/10.1038/s41598-021-98858-0.

[37] B. Zhmud, M. Najjari, and B. Brodmann, "The effects of the lubricant properties and surface finish characteristics on the tribology of high-speed gears for ev transmissions," *Lubricants*, vol. 12, no. 4, p. 112, 2024. DOI: 10.3390/lubricants12040112. [Online]. Available: https://www.mdpi.com/2075-4442/12/4/112.

[38] O. Rodríguez, B. N. J. Persson, and B. Lorenz, "On how to determine surface roughness power spectra," *Tribology Letters*, vol. 72, no. 3, p. 92, 2024. DOI: 10.1007/s11249-024-01933-6. [Online]. Available: https://doi.org/10.1007/s11249-024-01933-6.

[39] Y. Gong, S. T. Misture, P. Gao, and N. P. Mellott, "Surface roughness measurements using power spectrum density analysis with enhanced spatial correlation length," *The Journal of Physical Chemistry C*, vol. 120, no. 39, pp. 22 358–22 364, 2016.

[40] P. Podulka, W. Macek, M. Szala, A. Kubit, K. C. Das, and G. Królczyk, "Evaluation of high-frequency roughness measurement errors for composite and ceramic surfaces after machining," *Journal of Manufacturing Processes*, vol. 121, pp. 150–171, 2024.

[41] P. Podulka, W. Macek, B. Zima, G. Lesiuk, R. Branco, and G. Królczyk, "Roughness evaluation of turned composite surfaces by analysis of the shape of autocorrelation function," *Measurement*, vol. 222, p. 113 640, 2023.

[42] A. V. Oppenheim and R. W. Schafer, *Discrete-Time Signal Processing*, 3rd. Upper Saddle River, NJ: Pearson Education, 2014, ISBN: 978-0131988422.

[43] B. Jähne, H. Haußecker, and P. Geißler, *Handbook of Computer Vision and Applications: Volume 2, Signal Processing and Pattern Recognition*. San Diego, CA: Academic Press, 1999, ISBN: 978-0123797723.

[44] J. N. Reddy, *An introduction to continuum mechanics*. Cambridge university press, 2013.

[45] P. Mort, "Analysis and graphical representation of particle size distributions," *Powder Technology*, vol. 420, p. 118 100, 2023.

[46] P. Mort and L. Feltner, "Characterization Of Shot Size And Shape Distribution," *Metal Finishing News*, vol. 23, 2022.

[47] International Standards Organization 9276-6, *ISO 9276-6:2008(en), Representation of results of particle size analysis — Part 6: Descriptive and quantitative representation of particle shape and morphology*, 2008. [Online]. Available: https://www.iso.org/obp/ui/#iso:std:iso:9276:-6:ed-1:v1:en.

[48] SAE International, *Shot peening, SAE standard J2441*, SAE J2441, Warrendale, PA: Society of Automotive Engineers (SAE) International, 2015.

[49] SAE International, *Peening media general requirements, AMS2431*, SAE AMS2431, Warrendale, PA: Society of Automotive Engineers (SAE) International, 2017.

[50] D. Jones, C. Snider, A. Nassehi, J. Yon, and B. Hicks, "Characterising the Digital Twin: A systematic literature review," *CIRP journal of manufacturing science and technology*, vol. 29, pp. 36–52, 2020.

[51] B. Palotai, G. Kis, J. Abonyi, and Á. Bárkányi, "Surrogate-based flowsheet model maintenance for Digital Twins," *Digital Chemical Engineering*, vol. 15, p. 100 228, 2025.

[52] A. Świetlicki, M. Szala, and M. Walczak, "Effects of shot peening and cavitation peening on properties of surface layer of metallic materials—a short review," *Materials*, vol. 15, no. 7, p. 2476, 2022.

[53] K. Balan, "Are You Still Using MIL-S-13165," *The Shot Peener*, vol. Summer, 2020.

[54] L. Feltner and P. Mort, "CSEE Project Update: ISP Flowsheet model v1," Purdue University, Center for Surface Engineering and Enhancement, 2023.

[55] Dassault Systèmes, *Abaqus/Explicit User's Manual, Version 2019*. Providence, RI, USA: Dassault Systèmes Simulia Corp., 2019.

[56] K. TANAKA, "The cosalpha method for X-ray residual stress measurement using two-dimensional detector," *Mechanical Engineering Reviews*, vol. 6, no. 1, pp. 18-00378-18–00 378, 2019. DOI: 10.1299/MER.18-00378. [Online]. Available: https://www.researchgate.net/publication/328417354_The_cosa_method_for_X-ray_residual_stress_measurement_using_two-dimensional_detector.

[57] A. Kohri, Y. Takaku, and M. Nakashiro, "Comparison of X-ray residual stress measurement values by cos method and sin2 method," *Residual Stresses 2016*, p. 103, 2016.

[58] M. Abadi *et al.*, *TensorFlow: Large-Scale Machine Learning on Heterogeneous Systems*, 2016. [Online]. Available: https://www.tensorflow.org/.

[59] A. Klump, S. Klaus, V. Dietrich, and V. Schulze, "Prediction of Residual Stress States after modified Shot Peening Treatments using Strain-Rate and Temperature-dependent Material Data," in *Proceedings of the 14th International Conference on Shot Peening, Milan, Italy*, 2022, pp. 13–16.

[60] C. Wang, J. Hu, Z. Gu, Y. Xu, and X. Wang, "Simulation on residual stress of shot peening based on a symmetrical cell model," *Chinese Journal of Mechanical Engineering*, vol. 30, no. 2, pp. 344–351, 2017.

[61] A. Rosenfeld and J. L. Pfaltz, "Sequential operations in digital picture processing," *Journal of the ACM (JACM)*, vol. 13, no. 4, pp. 471–494, 1966.

[62] J. A. Slotwinski, E. J. Garboczi, and K. M. Hebenstreit, "Porosity measurements and analysis for metal additive manufacturing process control," *Journal of research of the National Institute of Standards and Technology*, vol. 119, p. 494, 2014.

[63] I. E. Anderson, E. M. White, and R. Dehoff, "Feedstock powder processing research needs for additive manufacturing development," *Current Opinion in Solid State and Materials Science*, vol. 22, no. 1, pp. 8–15, 2018.

[64] M. Y. Shaheen, A. R. Thornton, S. Luding, and T. Weinhart, "The influence of material and process parameters on powder spreading in additive manufacturing," *Powder technology*, vol. 383, pp. 564–583, 2021.

[65] M.-N. Pons and J. Dodds, "Particle shape characterization by image analysis," in *Progress in filtration and separation*, Elsevier, 2015, pp. 609–636.

[66] W. C. Krumbein and L. L. Sloss, *Stratigraphy and sedimentation*. LWW, 1951, vol. 71.

[67] J. Zheng and R. D. Hryciw, "Traditional soil particle sphericity, roundness and surface roughness by computational geometry," *Géotechnique*, vol. 65, no. 6, pp. 494–506, 2015.

[68] Y. Kim, H. S. Suh, and T. S. Yun, "Reliability and applicability of the krumbein-sloss chart for estimating geomechanical properties in sands," *Engineering Geology*, vol. 248, pp. 117–123, 2019.

[69] A. B. Spierings, N. Herres, and G. Levy, "Influence of the particle size distribution on surface quality and mechanical properties in am steel parts," *Rapid Prototyping Journal*, vol. 17, no. 3, pp. 195–202, 2011.

[70] J. S. Weaver *et al.*, "The effects of particle size distribution on the rheological properties of the powder and the mechanical properties of additively manufactured 17-4 ph stainless steel," *Additive manufacturing*, vol. 39, p. 101 851, 2021.

[71] J. A. Muñiz-Lerma, A. Nommeots-Nomm, K. E. Waters, and M. Brochu, "A comprehensive approach to powder feedstock characterization for powder bed fusion additive manufacturing: A case study on alsi7mg," *Materials*, vol. 11, no. 12, p. 2386, 2018.

[72] J. H. Martin *et al.*, "Additive manufacturing of a high-performance aluminum alloy from cold mechanically derived non-spherical powder," *Communications Materials*, vol. 4, no. 1, p. 39, 2023.

[73] M. Đuriš, Z. Arsenijević, D. Jaćimovski, and T. K. Radoičić, "Optimal pixel resolution for sand particles size and shape analysis," *Powder Technology*, vol. 302, pp. 177–186, 2016.

[74] S. Kröner and M. T. D. Carbó, "Determination of minimum pixel resolution for shape analysis: Proposal of a new data validation method for computerized images," *Powder technology*, vol. 245, pp. 297–313, 2013.

[75] R. Bitter, T. Mohiuddin, and M. Nawrocki, *LabVIEW: Advanced Programming Techniques*. Crc Press, 2006.

[76] M. Matlab, *Computer vision toolbox*.

[77] D. Legland, I. Arganda-Carreras, and P. Andrey, "Morpholibj," *Integrated library and plugins for mathematical morphology with ImageJ*, vol. 3532, doi, 2014.

[78] E. Pirard and P. Francus, "Image Measurements," in *Image Analysis, Sediments and Paleoenvironments*, ser. Developments in Paleoenvironmental Research, Dordrecht: Springer Netherlands, 2004, pp. 59–86, ISBN: 1-4020-2061-9.

[79] J. V. Daugmaudis, A. Laurynėnas, and F. Ivanauskas, "The influence of bounding surface on the precision of the cauchy–crofton method," *Lietuvos matematikos rinkinys*, vol. 51, pp. 250–255, 2010.

[80] V. Vilhelm, "Some formulae (areas, circumferences, volumes, surfaces, centroids, moments of inertia)," in *Survey of Applicable Mathematics*, K. Rektorys, Ed., Cambridge: MIT Press, 1969, ch. 3.

[81] F. Cao, K. Yao, and J. Liang, "Deconvolutional neural network for image super-resolution," *Neural Networks*, vol. 132, pp. 394–404, 2020.

[82] Y. Wang, L. Wang, H. Wang, P. Li, and H. Lu, "Blind single image super-resolution with a mixture of deep networks," *Pattern Recognition*, vol. 102, p. 107 169, 2020.

[83] L. Xu, J. S. Ren, C. Liu, and J. Jia, "Deep convolutional neural network for image deconvolution," *Advances in neural information processing systems*, vol. 27, 2014.

[84] P. Mort *et al.*, "Dense granular flow—a collaborative study," *Powder Technology*, vol. 284, pp. 571–584, 2015.

[85] J. J. Beaman, D. L. Bourell, C. C. Seepersad, and D. J. J. O. M. S. Kovar, "Additive manufacturing review: Early past to current practice," *Journal of Manufacturing Science and Engineering*, vol. 142, no. 11, p. 110 812, 2020.

[86] T. DebRoy *et al.*, "Additive manufacturing of metallic components–process, structure and properties," *Progress in materials science*, vol. 92, pp. 112–224, 2018.

[87] J. Liu *et al.*, "Current and future trends in topology optimization for additive manufacturing," *Structural and multidisciplinary optimization*, vol. 57, no. 6, pp. 2457–2483, 2018.

[88] Z. Zhu, N. Anwer, and L. Mathieu, "Statistical modal analysis for out-of-plane deviation prediction in additive manufacturing based on finite element simulation," *Journal of Manufacturing Science and Engineering*, vol. 141, no. 11, p. 111 011, 2019.

[89] A. Averardi, C. Cola, S. E. Zeltmann, and N. Gupta, "Effect of particle size distribution on the packing of powder beds: A critical discussion relevant to additive manufacturing," *Materials today communications*, vol. 24, p. 100 964, 2020.

[90] J. P. Oliveira, A. D. LaLonde, and J. Ma, "Processing parameters in laser powder bed fusion metal additive manufacturing," *Materials & Design*, vol. 193, p. 108 762, 2020.

[91] X. Fu, D. Huck, L. Makein, B. Armstrong, U. Willen, and T. Freeman, "Effect of particle shape and size on flow properties of lactose powders," *Particuology*, vol. 10, no. 2, pp. 203–208, 2012.

[92] S. Yim, H. Bian, K. Aoyagi, K. Yamanaka, and A. Chiba, "Effect of powder morphology on flowability and spreading behavior in powder bed fusion additive manufacturing process: A particle-scale modeling study," *Additive Manufacturing*, vol. 72, p. 103 612, 2023.

[93] E. J. Parteli and T. Pöschel, "Particle-based simulation of powder application in additive manufacturing," *Powder Technology*, vol. 288, pp. 96–102, 2016.

[94] L. Feltner, E. Korte, D. F. Bahr, and P. Mort, "Particle size and shape analyses for powder bed additive manufacturing," *Particuology*, 2023. DOI: 10.1016/j.partic.2023.09.001.

[95] B. Mandelbrot, "How long is the coast of Britain? Statistical self-similarity and fractional dimension," *science*, vol. 156, no. 3775, pp. 636–638, 1967.

[96] T. Allen, *Particle Size Measurement* (Powder Technology Series), Fourth edition. Springer Dordrecht, 1990, ISBN: 978-94-009-0417-0.

[97] H. P. Schwarcz and K. C. Shane, "Measurement of particle shape by Fourier analysis," *Sedimentology*, vol. 13, no. 3–4, pp. 213–231, 1969.

[98] J. K. Beddow and G. Philip, "ON THE USE OF A FOURIER ANALYSIS TECHNIQUE FOR DESCRIBING THE SHAPE OF INDIVIDUAL PARTICLES.," *Planseeber*, vol. 23, pp. 3–14, 1975.

[99] R. Ehrlich and B. Weinberg, "An exact method for characterization of grain shape," *Journal of sedimentary research*, vol. 40, no. 1, pp. 205–212, 1970.

[100] T. P. Meloy, "Fast Fourier transforms applied to shape analysis of particle silhouettes to obtain morphological data," *Powder Technology*, vol. 17, no. 1, pp. 27–35, 1977.

[101] R. Davies, "A simple feature-space representation of particle shape," *Powder Technology*, vol. 12, no. 2, pp. 111–124, 1975, ISSN: 0032-5910. DOI: 10.1016/0032-5910(75)80003-9.

[102] G. M. Chávez, F. Castillo-Rivera, J. A. Montenegro-Ríos, L. Borselli, L. A. Rodríguez-Sedano, and D. Sarocchi, "Fourier Shape Analysis, FSA: Freeware for quantitative study of particle morphology," *Journal of Volcanology and Geothermal Research*, vol. 404, p. 107 008, 2020.

[103] J. Fonseca and C. O'Sullivan, "A re-evaluation of the Fourier descriptor approach to quantifying sand particle geometry," in *4th International Symposium on Deformation Characteristics of Geomaterials*, 2008, pp. 687–690.

[104] M. Diepenbroek, A. Bartholomä, and H. Ibbeken, "How round is round? A new approach to the topic 'roundness' by Fourier grain shape analysis," *Sedimentology*, vol. 39, no. 3, pp. 411–422, 1992.

[105] H. Nyquist, "Certain topics in telegraph transmission theory," *Transactions of the American Institute of Electrical Engineers*, vol. 47, no. 2, pp. 617–644, 1928.

[106] X. Liu, E. J. Garboczi, M. Grigoriu, Y. Lu, and S. T. Erdoğan, "Spherical harmonic-based random fields based on real particle 3D data: Improved numerical algorithm and quantitative comparison to real particles," *Powder Technology*, vol. 207, no. 1–3, pp. 78–86, 2011.

[107] D. Su and W. M. Yan, "3D characterization of general-shape sand particles using microfocus X-ray computed tomography and spherical harmonic functions, and particle regeneration using multivariate random vector," *Powder Technology*, vol. 323, pp. 8–23, 2018.

[108] J. W. Bullard and E. J. Garboczi, "Defining shape measures for 3D star-shaped particles: Sphericity, roundness, and dimensions," *Powder technology*, vol. 249, pp. 241–252, 2013.

[109] G. Hansen, I. Herburt, H. Martini, and M. Moszyńska, "Starshaped sets," *Aequationes mathematicae*, vol. 94, pp. 1001–1092, 2020.

[110] M. C. Thomas, R. J. Wiltshire, and A. T. Williams, "The use of Fourier descriptors in the classification of particle shape," *Sedimentology*, vol. 42, no. 4, pp. 635–645, 1995.

[111] H. Abdi and L. J. Williams, "Principal component analysis," *Wiley interdisciplinary reviews: computational statistics*, vol. 2, no. 4, pp. 433–459, 2010.

[112] S. R. (R. Searle, *Matrix Algebra Useful for Statistics* (Wiley Series in Probability and Mathematical Statistics. Applied Probability and Statistics). New York: Wiley, 1982, ISBN: 0-471-86681-4.

[113] SAS Institute Inc., *JMP Pro 16*. Cary, NC: SAS Institute Inc., 2021. [Online]. Available: https://www.jmp.com/en_us/software/predictive-analytics-software.html.

[114] B. F. Apostol, "Elastic equilibrium of the half-space revisited. Mindlin and Boussinesq problems," *Journal of Elasticity*, vol. 125, no. 2, pp. 139–148, 2016.

[115] M. Tunwal, K. F. Mulchrone, and P. A. Meere, "A new approach to particle shape quantification using the curvature plot," *Powder Technology*, vol. 374, pp. 377–388, 2020.

[116] W. C. Graustein, *Differential Geometry*. Courier Corporation, 2012.

[117] B. Osgood, *Lectures on the Fourier Transform and Its Applications* (The Sally Series). Providence, Rhode Island: American Mathematical Society, 2019, ISBN: 978-1-4704-4191-3.

[118] R. M. Gray and J. W. Goodman, *Fourier Transforms: An Introduction for Engineers*. Springer Science & Business Media, 2012, vol. 322.

[119] C. E. Shannon, "Communication in the presence of noise," *Proceedings of the IRE*, vol. 37, no. 1, pp. 10–21, 1949.

[120] C. R. Harris *et al.*, "Array programming with NumPy," *Nature*, vol. 585, no. 7825, pp. 357–362, Sep. 2020. DOI: 10.1038/s41586-020-2649-2. [Online]. Available: https://doi.org/10.1038/s41586-020-2649-2.

[121] J. W. Cooley and J. W. Tukey, "An algorithm for the machine calculation of complex Fourier series," *Mathematics of computation*, vol. 19, no. 90, pp. 297–301, 1965.

A. Particle size and shape analyses for powder bed additive manufacturing

A.1 Introduction

This is a case study of particle size and shape analysis using dynamic imaging of two powdered metal samples intended for use in Powder Bed Fusion (PBF), a method of Additive Manufacturing (AM). One sample was produced by melt atomization, the other by cold mechanical processing, a precise size-reduction process. The methods of production affect the size and shape distributions. Classification of particles improves the reproducibility of PBF processes, as particle size and shape impact steps from powder flow to bed packing to optical interactions with lasers used to locally melt the material. Particle image data were collected using a commercial Dynamic Imaging Analysis (DIA) system described in Section A.2. The raw data, in the form of 8-bit grayscale digital images, were analyzed in more detail to determine the effects of pixel scale resolution (i.e., the number of pixels per particle) on shape descriptors. We compare and contrast the data for each sample, and consider the effect of pixel-scale resolution on the comparison.

A principal component analysis of shape descriptors showed that over 90% of differences within the samples used in this study were explained using two components: one indicating elongated shape (i.e., aspect ratio), and another indicating features associated with perimeter length in excess of a smooth ellipse. Subjectively, excess perimeter length can manifest as bumpiness or angularity. The ISO-standard Form Factor (ISO, 2008) captures a combination of the two effects, and can be used to indicate about 60% of the differences using a single shape factor. This study includes a detailed analysis of pixel-scale resolution on principal shape descriptors.

Characterization of porosity is important in many applications. Porosity can be associated with individual particles (intra-particle, ε_{tra}) as well as interstitial voids in an ensemble packing (inter-particle voids, ε_{ter}). Metal powder additive manufacturing can meet a range of structural objectives requiring control and manipulation of porosity [62]. Often the objective is to make fully-dense structures, i.e., the total elimination of porosity. In other cases, for example bio-medical implants, some residual porosity may be desired. While the effects

of closed intra-particle porosity, $\varepsilon_{\text{tra,closed}}$, for example as a consequence of trapped gas in an atomization process, have been traced to defects in AM parts [63], there is comparatively little work on the effects of particle shape on spreading and packing in powder-bed processes [64]. Intra-particle porosity that is related to concavity, $\varepsilon_{\text{tra,open}}$, may be a useful in correlating shape with spreading and packing. This study explores the relationship between intra-particle porosity and perimeter concavity that is detectable with 2D image analysis. Machine learning (ML) for fine-grain image reconstruction is discussed in this context.

The results and discussion of Principal Component Analysis and mapping of orthogonal shape descriptors is covered in Sections A.4.1 through A.4.3. Section A.4.4 covers the effect of pixel resolution on shape analysis, first on the basis of individual particles (Section A.4.4), and then on a distributed ensemble basis (Section A.4.4). Enhancement of shape resolution using machine learning is introduced in Section A.4.4, and discussed further in Section A.7.

A.2 Background–Image Analysis

Many studies on particle image analysis are available in the literature. With advances in digital imaging and data processing technologies, size and shape analyses are becoming more routine for many applications [65]. However, given the long history of particle image analysis and its diverse applications, there remain some contradictions on terminology and analysis. For example, shape mapping is well practiced in geo-mechanics, using KrumbeinSchloss charts [66] and variations thereof [67, 68] to correlate shape distributions with stability, packing, and flow of sands and sediments. In relation to the current work, geo-technical "sphericity" is analogous to the bounding-box aspect ratio, AR_{box}; and geo-technical "roundness" is indirectly related to an extended perimeter measure described herein as the elliptical form factor, EFF (see details in Section A.3 and Section A.6). As a starting point, this study references the guidance and terminology of the International Standards Organization [47].

Particle size distributions have been shown to have a significant effect on the mechanical properties and surface finish of additively manufactured parts [69, 70]. There is also precedence that the morphology of the powder influences the outcome of the process [71,

72]. This has been attributed to size and shape distributions affecting powder spreading performance, leading to non-uniform layer thicknesses in severe cases. It is therefore critical to be able to accurately and repeatably characterize the particle size and shape distribution of additive powders consistently across the size distribution in order to predict and control an additive manufacturing process.

The effect of digital image resolution and pixilation on shape results and the uncertainty thereof has been studied [73, 74]. These articles point out that the computation of particle perimeter, and shape factors that utilize perimeter, are especially affected by relatively coarse pixel scales. Most commonly used commercial and open source vision packages calculate a smoothed perimeter measurement, rather than summing the total length of pixel edges [75–77]. If not explicitly defined as such, this technique is analogous to CauchyCrofton smoothing [47, 78], relying on numerical integration to calculate an approximate curve length. The effect of bounding surface construction on the precision of the CauchyCrofton computation has also been explored, with the conclusion that irregular surfaces require a higher degree of detail to accurately compute the length or area [79]. The particle's area is computed as the sum of pixels below a threshold grayscale value. When this area is compared with a smoothed perimeter, inconsistencies can arise, especially at low pixel counts, leading to a smoothed perimeter that is illogical for a measured area, i.e., having an area to perimeter ratio higher than an ideal circle. This phenomenon is an artifact of inaccurate perimeter smoothing, i.e., smoothing over an insufficient number of pixels. Overall, high resolution is desired for robust imaging and analysis; this is an inherent challenge for particle distributions having significant dispersity in size and shape features. This paper seeks to illustrate and understand the effects of image analysis uncertainty across a distributed set of size and shape characteristics.

A.3 Experimental methodology

Fine metal powders comprising 7075 aluminum alloy obtained from two commercial vendors were used in this study. The gas atomized (GA) sample was made by melting-gas atomization; the other sample was made via a proprietary (US Patent No. US20210146442A1,

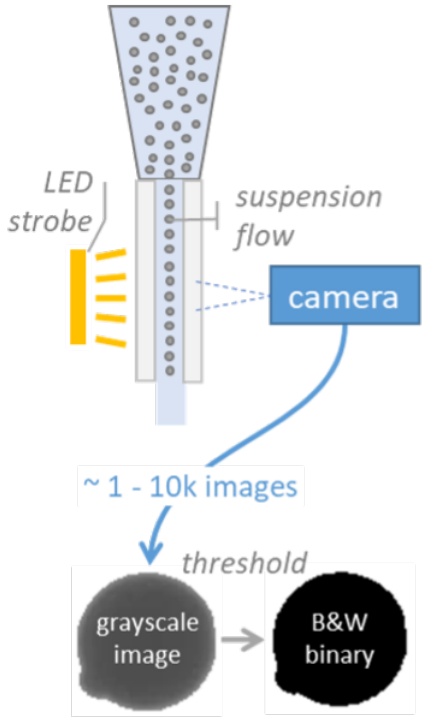

Figure A.1. Dynamic image analysis (InFlow™, JM Canty) with lab dilution controls (not shown).

2019) size-reduction process (cold mechanical processing, CMP). Both were measured in a liquid-dispersion flow-through imaging system (InFlow™, JM Canty, Lockport, NY, USA) having a back-lit strobe exposure time of (20 μs) and image resolution of 0.34 μm/pixel. The back-lit imaging captures 2D projections of particles that are randomly-oriented in a suspension flow, i.e., dynamic image analysis (Fig. A.1). The InFlow system uses NI Vision (National Instruments, Austin, TX, USA) as a foundational platform for data acquisition and analysis of size and shape features. InFlow software has an option to save 8-bit grayscale digital bitmaps of all particles; this was used for detailed analysis of the effects of pixilation on shape conducted in this study.

Samples of AM metal powders were prepared by placing ~0.5 g of metal powder in a glass vial, and then adding several drops of iso-propyl alcohol as a surface-wetting agent. The IPA has a secondary function of being an anti-foam agent. About 10 ml of an aqueous

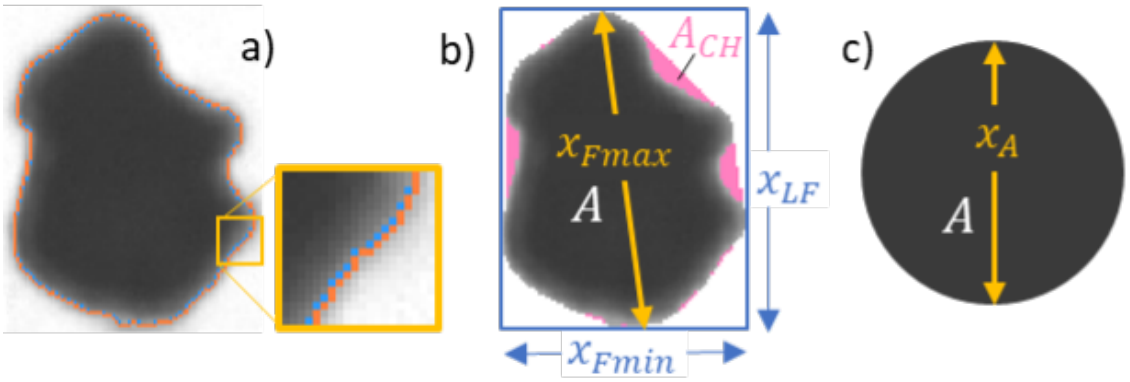

Figure A.2. Image analysis descriptors: (a) grayscale particle image with perimeter thresholding, orange = edge pixels, blue = interior corners; (b) thresholded image with minimum Feret bounding box in blue, additional convex hull area in pink; (c) area-equivalent diameter. Illustrated particle data: $x_{F\,\mathrm{min}} = 25.4$ μm, $x_{LF} = 33.1$ μm, $x_{F\,\mathrm{max}} = 33.4$ μm, $x_A = 27.7$ μm, $A = 602$ μm^2, $A_{CH} = 633$ μm^2, $P = 95.1$ μm.

diluent is added to make a suspension of the metal powder. The diluent comprised 4% hydroxypropyl cellulose (HPC Klucel, obtained from Ashland Chemical, Wilmington, DE, USA) as a thickening agent. Increasing viscosity (∼0.3 Paůs) was effective in reducing the settling speed of the particles and stabilizing the dilution control loop. The suspension was mixed by repeated syringe drawing and extraction, taking care to avoid generation of air bubbles.

At the start of the measurement, the InFlow provides a reservoir in a sample reservoir, to which the prepared suspension was added, again using the syringe to avoid generation of air bubbles. Dual peristaltic pumps are used to draw the sample suspension though the imaging cell according to a control loop objective of 0.2% screen area below the particle detection threshold. The threshold setting was 170 out of a grayscale of 0–255, i.e., pixels $\leq$ 170 were considered to be within a particle, pixels $>$ 170 were considered background. Note that metals are optically opaque materials, providing good edge contrast. The inset in Fig. A.2(a) shows edge discrimination at the 170 threshold; orange pixels have at least one edge and blue pixels have at least one corner crossing the threshold.

Size and shape analyses conducted in this study are based on the following image features, illustrated in Fig. A.2:

- Area and convex-hull area: A and A_{CH}, respectively;
- Perimeter, P, based on smoothing of the pixelated edge, shown by the orange pixels in Fig. A.2(a);
- Feret lengths: minimum, orthogonal to the minimum, and maximum, $x_{F\,\mathrm{min}}$, x_{LF}, and $x_{F\,\mathrm{max}}$ respectively;
- Area-equivalent size, $x_A = \sqrt{4A/\pi}$, derived from the area A;
- Particle volume is based on area, $V = \frac{4A^{1.5}}{3\sqrt{\pi}}$.

Data filtering was done on the basis of grayscale intensity (100-threshold) averaged over the particle area. Shape descriptors include the following:

Aspect ratios:

$$AR_{\mathrm{box}} = \frac{x_{F\,\mathrm{min}}}{x_{LF}}, \qquad AR_{\mathrm{ISO}} = \frac{x_{F\,\mathrm{min}}}{x_{F\,\mathrm{max}}}$$

Form factors: standard (ISO) and elliptical (see Section A.6 for derivation):

$$FF = \frac{4\pi A}{P^2}, \qquad EFF = \frac{\beta\pi A}{P^2}, \quad \beta = \left(\frac{1.5(1+AR_{\mathrm{box}})}{\sqrt{AR_{\mathrm{box}}}} - 1\right)^2$$

Area ratios per ISO guidance: Box area, Extent, and Solidity:

$$BAR = \frac{A}{x_{F\,\mathrm{min}} \cdot x_{LF}}, \qquad Ext = \frac{A}{x_{F\,\mathrm{min}} \cdot x_{F\,\mathrm{max}}}, \qquad S = \frac{A}{A_{\mathrm{CH}}}$$

An estimate of intra-particle porosity, $\varepsilon_{\mathrm{tra}}$, was derived using a 2D to 3D transformation of solidity. It is an estimate of concave porosity that is visually open in a 2D projection of a 3D particle, i.e., $\varepsilon_{\mathrm{tra,open}}$, and may affect ensemble packing. It does not account for porosity that is not visible, e.g., internal pores that are effectively closed, $\varepsilon_{\mathrm{tra,closed}}$. Going forward

in this paper, all references to ε_{tra} imply $\varepsilon_{\text{tra,open}}$. Note that from a distribution analysis perspective, ε_{tra} provides a more sensitive metric than solidity:

$$\varepsilon_{\text{tra}} = 1 - S^{1.5}.$$

A.4 Results and discussion

A.4.1 Principal component analysis of particle shape

Principal component analysis (PCA) of shape descriptors was used to identify clusters and rank individual shape descriptors in terms of their effectiveness in shape differentiation (JMP, SAS Institute, Cary, NC, USA). The volume-weighted PCA included the combined data of GA ($N = 5629$) and CMP ($N = 1086$) particle samples, each having equivalent total particle volumes of 7.81×10^{-2} mm^3. The results showed that over 90% of shape effects can be described with two principal components (Fig. A.3). Clustering of shape descriptors by principal component (Table A.1) indicates characteristic features for orthogonal components, EFF and AR_{box}, respectively. Characteristic features are defined as having the highest correlation (R^2) within a given cluster, and the lowest correlation with other clusters. The characteristic features, EFF and AR_{box}, are used as orthogonal factors in shape mapping, Section A.4.3.

When shape descriptors are constrained to a single cluster, FF becomes the most representative feature; essentially, FF is a combination of EFF and AR_{box}. However, clustering all effects within a single component describes only about 65% of the shape variance. Hence, the deconstruction of the form factor into elongation and perimeter effects provides a substantial improvement in the statistical description of particle shape.

A.4.2 Size and shape distributions

Size distribution analysis was done using weighted regression method [45]. The log-normal fits reveal significant differences in size distributions of the two samples (Fig. A.4), where the fit parameters relate to cumulative distribution functions (cdf_{LN}) per Equation A.1. Compared to the GA sample, CMP is larger in size and narrower in distribution

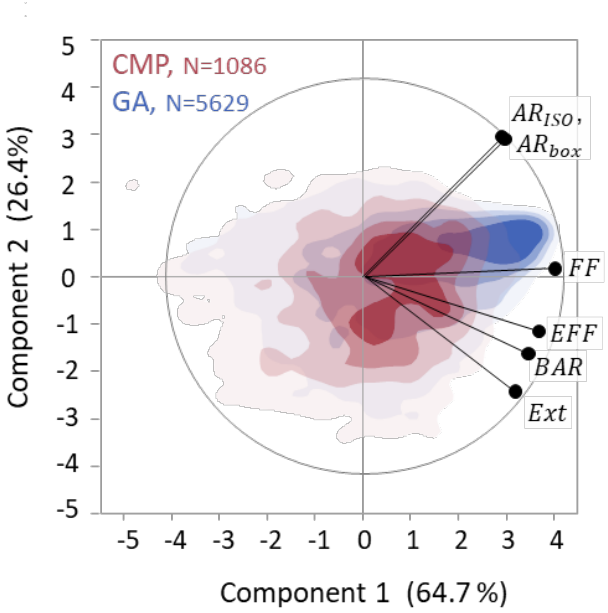

Figure A.3. Principal component analysis of shape descriptors for combined samples: gas-atomized (GA), cold mechanical processed (CMP). Color hue contours represent the data density of each sample; number of data points in legend.

Table A.1. PCA cluster summary.

Cluster	Members	R^2 within cluster	R^2 w/ other cluster
1	EFF	0.864	0.141
	Ext	0.810	0.018
	BAR	0.807	0.100
	FF	0.799	0.438
2	AR_{box}	0.991	0.164
	AR_{ISO}	0.991	0.169

when viewed as a volume-basis distribution (Fig. A.4(a)). The number basis distribution has a bimodal fines tail in the CMP sample, but not in GA. While the CMP processing and any subsequent classification step is apparently highly efficient on a volume basis, the number distribution reveals a trace residue of fines; this is typical of a milling-classification process.

$$cdf_{LN}(x) = \tfrac{1}{2} \cdot \left(1 + \operatorname{erf}\left(\frac{\ln(x/x_g)}{\sqrt{2}\,\ln(\sigma_g)}\right)\right) \tag{A.1}$$

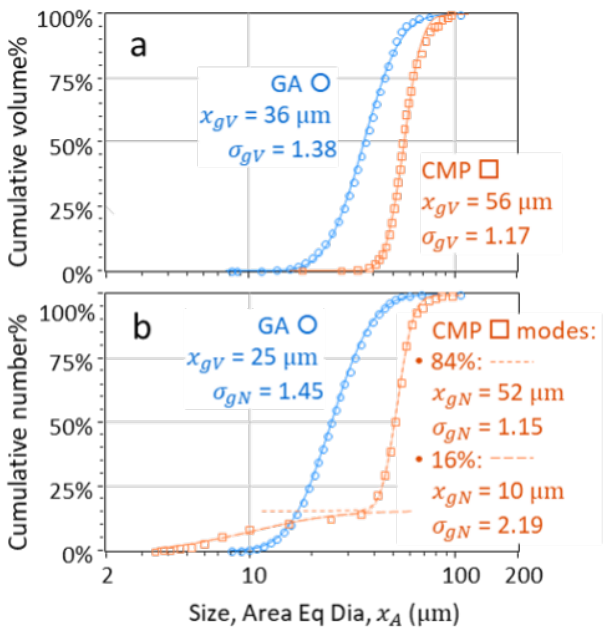

Figure A.4. Size distributions with log-normal fitting parameters for gas-atomized (GA) and cold mechanical processed (CMP) samples: (a) volume; (b) number basis.

The weighted regression method was also used to analyze shape distributions. Shape factors are dimensionless, and bounded between 0 and 1, $(0, 1]$. Bimodal stretched-exponential distribution (i.e., Weibull) functions were used to model the shape data. Fit parameters in Table A.2 describe the shape distributions according to Equation A.2, where the modes are summed to describe stretched-exponential cumulative distribution functions (cdf_{SE}) on a volume basis. The density plots (Fig. A.5) are the derivatives of the cumulative data with respect to $\ln(x)$.

$$cdf_{SE}(x) = 1 - \exp\left[-\left(\frac{x}{x^*}\right)^n\right] \tag{A.2}$$

Comparing the two samples, the GA sample has marginally higher mode values (x^*) for all three features indicating more rounded morphology; however, there is broad overlap over the full distributions. The CMP sample has discernably sharper peaks (higher weighted n) within the density distributions, suggesting the process creates a tight distribution.

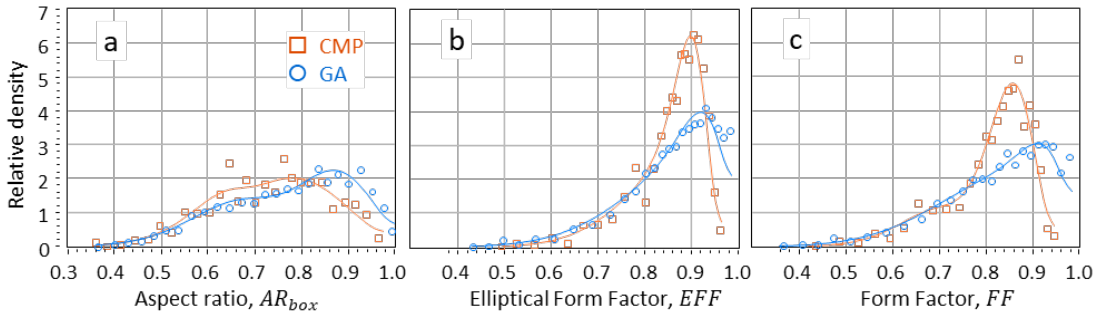

Figure A.5. Volume-basis shape distributions: (a) Aspect Ratio, (b) Elliptical Form Factor, (c) Form Factor.

Table A.2. Fit parameters for bimodal stretched-exponential shape distributions shown in Fig. A.5; gas-atomized (GA) or cold mechanical processed (CMP) samples.

		AR_{box}			EFF			FF		
Sample	Mode	vol%	x^*	n	vol%	x^*	n	vol%	x^*	n
GA	1	63%	0.87	9.7	47%	0.93	18.6	33%	0.93	18.2
	2	37%	0.64	7.3	53%	0.82	7.9	67%	0.80	6.8
CMP	1	86%	0.78	6.4	60%	0.90	26.3	77%	0.86	17.3
	2	14%	0.62	10.7	40%	0.81	10.2	23%	0.67	10.2

A.4.3 Shape mapping

The orthogonal relationship between Aspect Ratio and the Elliptical Form Factor enables graphical mapping of shape factors using contours (Fig. A.6). A value of (1,1) is a circle, i.e., a 2D projection of a spherical particle. Decreasing values along the ordinate correspond to shape elongation, i.e., reduced aspect ratio. Decreasing abscissa values indicate perimeter length in excess of a smooth ellipse; reduction in EFF can manifest as subjective features such as bumpiness or angularity. Grayscale contours (z-axis) indicate sample density (darker is higher density), weighted according to a distribution basis or moment, e.g., the volume bases shown in Fig. A.6 were calculated from the accumulated volume of particles in each sample's (x, y) domain.

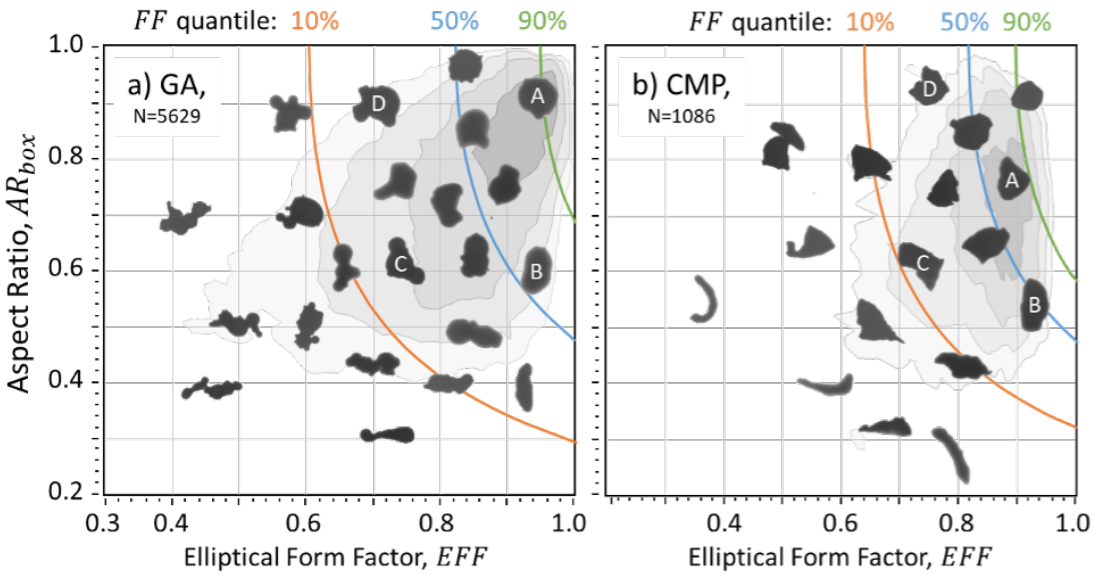

Figure A.6. Shape feature mapping: (a) gas-atomized (GA), (b) cold mechanical processed (CMP) particles. Volume-basis density indicated by grayscale contours. Tagged particles (A, B, C, D) are used for detailed analysis of pixel resolution shown in Fig. A.8.

Colored contour lines show selected Form Factor quantiles for each sample. Recall, the Form Factor shows the effect of having a perimeter length in excess of a circle of the same area. It combines both perimeter irregularity and elongation into a single shape descriptor, but does not distinguish between each effect. For example, in Fig. A.6(b), particles labeled B and D are both close to the median form factor, FF_{50}, yet B is elongated and relatively smooth, and D is equiaxed and comparatively bumpy.

Each map is illustrated by thresholded grayscale images showing differences and trends for each sample. Objectively, shape factors in and of themselves do not necessary differentiate between samples, i.e., GA versus CMP. Visual imaging adds value to the analysis, in this case offering visual evidence of the effects of different manufacturing processes.

A.4.4 Pixel-scale resolution

In the above analysis, particles have relatively high pixel resolution, i.e., per ISO guidance (ISO, 2008) of at least 5000 pixels/particle for robust shape analysis with factors requiring perimeter measurement. In the GA sample, the number and volume-weighted geometric averages were 4300 and 8800 pixels/particle, respectively. In the CMP sample, it was 11,800 and 22,400 respectively. High-resolution imaging provides confidence in shape analysis. In this part of the study, we investigate the effect of pixel resolution on shape analysis. Taking the high-resolution data as a reference, systematic coarse-graining was done to reduce linear pixel-scale resolution, following a Fibonacci sequence: 2, 3, 5, 8, 13, 21, resulting in areal reduction of pixel resolution by factors of 4, 9, 25, 64, 169, and 441+, to a limit of about 10 pixels/particle. Coarse graining is illustrated in Fig. A.7 using two example particles from the CMP sample; these examples were chosen according to modes of the shape distribution described in Table A.2.

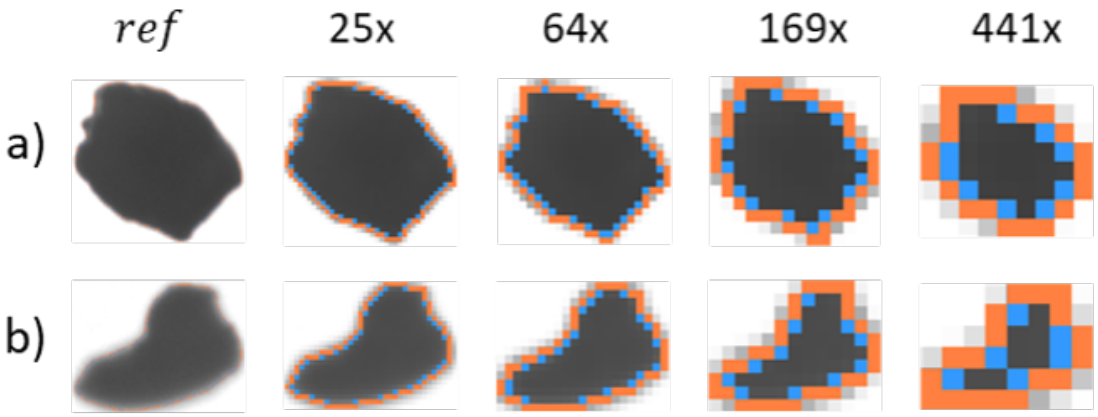

Figure A.7. Coarse-graining by area of gray-scale images with perimeter threshold pixels in color (orange edges, blue interior corners), representing CMP shape distribution modes: (a) $AR_{\text{box}} = 0.78$, $EFF = 0.90$; (b) $AR_{\text{box}} = 0.62$, $EFF = 0.81$.

Pixel-scale resolution of individual particles

Individual reference particles were selected for each sample, covering the shape distribution map (particles AD in Fig. A.6). In Fig. A.8, thresholded grayscale images are shown for each reference (AD) along with additional convex hull area in pink. Examples of coarse graining by area (25x, 169x) illustrate the effect of pixel scale resolution on the convex hull. In reference cases having only small amounts of concavity (i.e., A, B; having high EFF on the map), convex hull area was eliminated by coarse graining. In cases having more concavity (i.e., C, D; low EFF), convex hull persisted, but was eventually eliminated by extreme coarse-graining.

In an effort to improve precision of shape descriptors, a fine-graining method was developed using machine learning; details are provided in Section A.7. Selected fine-graining results are shown in Fig. A.8, essentially reconstructing the reference from coarsened states. The effects of coarse graining and numerical reconstruction by fine-graining on shape descriptors are summarized in Tables A.3 and A.4.

Ensemble effects

Ensemble results for selected shape factors are shown as contour plots, Figs. 911. The reference data set had ∼7,600 particles; the coarse-grained set had ∼40,000, combining both GA and CMP samples. The reference line at 1.0 on the ordinate indicates consistency with the raw data; deviation from the 1.0 reference shows the effect of reduced pixel scale resolution on shape analysis. Coarse grained data are shown as contour maps, where color hue corresponds to data density.

Note the vertical dashed line at 5000 (5k) particles indicates the ISO guidance for robust perimeter-based shape measures. Below this, shape analyses inherit uncertainties related to perimeter smoothing and particle orientation. Under-estimation of the perimeter results in over-estimation of Form Factors; in some cases, illogical Form Factors (i.e., > 1) may result.

Fig. A.9 confirms uncertainty related to perimeter smoothing. With NI-Vision, uncertainty is reasonably balanced as low as about 300 pixels; at lower resolution, a significant

Table A.3. Summary of coarse- and fine-graining shape effects for selected (ref A–D, Fig. A.6a) gas-atomized (GA) particles.

	A			B		
	EFF	AR_{box}	ε_{tra}	EFF	AR_{box}	ε_{tra}
ref	0.95	0.91	1.7%	0.96	0.59	1.2%
25x	0.94	0.99	0.0%	0.95	0.60	0.3%
64x	0.90	0.97	1.4%	0.98	0.61	0.0%
169x	0.97	0.85	0.0%	0.97	0.64	0.0%
441x	1.10	0.85	0.0%	1.01	0.57	0.0%
25x FG	0.92	0.90	3.0%	0.93	0.58	3.6%
64x FG	0.90	0.88	4.4%	0.95	0.58	3.3%
169x FG	0.92	0.86	3.7%	0.95	0.59	4.8%
441x FG	0.89	1.00	1.7%	0.97	0.57	2.7%

	C			D		
	EFF	AR_{box}	ε_{tra}	EFF	AR_{box}	ε_{tra}
ref	0.77	0.61	14.5%	0.72	0.89	15.9%
25x	0.76	0.62	13.4%	0.75	0.92	14.5%
64x	0.82	0.58	7.8%	0.80	0.86	10.9%
169x	0.76	0.60	3.1%	0.75	0.89	5.4%
441x	1.00	0.63	0.0%	0.89	0.73	0.0%
25x FG	0.74	0.62	16.2%	0.69	0.90	18.4%
64x FG	0.75	0.61	15.1%	0.70	0.88	18.9%
169x FG	0.77	0.62	14.0%	0.72	0.89	17.9%
441x FG	0.81	0.62	11.2%	0.83	0.90	10.1%

skew toward under-estimated perimeters (i.e., over-estimated Form Factors) is observed. Pixel-scale uncertainty also affected Aspect Ratios (Fig. A.10). While the bounding box ratio was reasonably balanced (Fig. A.10(b)), the ISO-defined aspect ratio showed a significant skew with even small amounts of coarse graining. This result suggests a systematic trend toward higher relative maximum Feret lengths with coarser pixilation.

The effect of pixilation on intra-particle porosity derived from Solidity is more profound (Fig. A.11). The results were bimodal, showing the porosity estimate of many particles dropping to zero with increasing pixilation i.e., loss of concavity with pixilation. This effect is most severe with particles having only small amounts of concavity in the reference

Table A.4. Summary of coarse- and fine-graining shape effects for selected (ref A–D, Fig. A.6b) cold mechanical processed (CMP) particles.

	A			B		
	EFF	AR_{box}	ε_{tra}	EFF	AR_{box}	ε_{tra}
ref	0.88	0.77	3.4%	0.93	0.55	2.2%
25x	0.87	0.77	2.0%	0.91	0.58	2.0%
64x	0.86	0.75	0.0%	0.89	0.59	1.2%
169x	0.84	0.83	0.0%	0.94	0.56	0.0%
441x	1.01	0.75	0.0%	0.98	0.55	0.0%
25x FG	0.85	0.76	4.7%	0.90	0.55	3.8%
64x FG	0.86	0.73	3.6%	0.92	0.55	3.5%
169x FG	0.87	0.77	5.2%	0.94	0.55	3.6%
441x FG	0.90	0.88	2.8%	0.95	0.55	2.1%

	C			D		
	EFF	AR_{box}	ε_{tra}	EFF	AR_{box}	ε_{tra}
ref	0.77	0.61	13.2%	0.77	0.96	11.0%
25x	0.74	0.62	11.5%	0.76	0.97	9.9%
64x	0.76	0.63	11.1%	0.79	1.00	9.6%
169x	0.83	0.62	5.7%	0.81	0.99	5.6%
441x	0.73	0.67	9.7%	0.87	0.99	2.5%
25x FG	0.74	0.61	14.4%	0.74	0.94	12.2%
64x FG	0.75	0.61	14.3%	0.76	0.93	11.6%
169x FG	0.77	0.60	13.2%	0.80	0.92	10.6%
441x FG	0.78	0.62	14.4%	0.82	0.91	8.4%

condition. Concavity was more persistent in reference particles that have more significant reference porosity.

Considering total pore volume, the results in Table A.5 represent the summed-up ε_{tra} pore volume over the volume-weighted size distributions of each sample. These results show bulk intra-particle porosity derived from concavity having a gradual reduction in the estimated bulk porosity with coarse graining. It means that the bimodal appearance of Fig. A.11, while interesting from the perspective of concavity associated with a distribution of individual particles, may be less important to the estimation of cumulative bulk porosity.

Table A.5. Bulk intraparticle density as a function of coarse graining.

Coarse grain	GA Bulk ε_{tra}	CMP Bulk ε_{tra}
ref	8.58%	7.26%
4	7.89%	6.72%
9	7.29%	6.26%
25	6.49%	5.67%
64	5.44%	4.81%
169	4.07%	3.63%
441	3.29%	2.40%

An ensemble summary of pixilation uncertainty was evaluated using the standard deviation of each shape factor as a function of the degree of coarse graining in Fig. A.12. The relative standard deviation was calculated by normalizing the volume-weighted standard deviation to the reference. A power law trend is generally followed in Fig. A.12, showing RSD uncertainty in the range of about 5–6% at 300 pixels/particle. Note the confidence limits are tightest for the bounding box Aspect Ratio, AR_{box}, and marginally looser for the Form Factors. On one hand, this is consistent with ISO guidance regarding uncertainty of perimeter measures; on the other, it suggests opportunities for improved perimeter-measurement algorithms. Results suggest that ML fine-graining can recover porosity and convexity from low-resolution data, and enables more consistent perimeter and shape factor calculations.

A.5 Conclusion

Shape descriptor uncertainty depends on pixilation. For shape distribution statistics, resolution as low as about 300 pixels/particle can provide reasonable accuracy, within a relative standard deviation of about 5%. The primary limitation is robust calculation of particle perimeters; at low pixel resolution, perimeter calculations are both skewed and variable, resulting in the possibility of illogical form factor values, i.e., FF or EFF > 1.0. Applying fine-graining via machine learning can address this problem, maintaining logical form factors and enabling statistically-robust shape mapping across broader size ranges.

Shape mapping using Aspect Ratios and Elliptical Form Factors is consistent with principal component analysis of AM powder datasets, i.e., the Elliptical Form Factor is orthogonal to the Aspect Ratio. Mapping particles on an AR versus EFF plane decouples perimeter-related irregularities such as bumpiness or angularity from elongation. Superposing particle images on the map is a useful way to visualize differences between samples, for example the effects of their manufacturing process.

Intra-particle porosity estimates, computed by way of convex hull, are severely impacted with limited pixel counts. Hence, correlation with solidity under-represents intra-particle porosity at coarse pixel scales. While much of the concavity detail lost in coarse particle images can be recovered through image fine-graining, there is a possibility to over-correct compared to reference training data. This begs the question about the need for even higher-resolution reference data in context of correlating imaging descriptors with porosity. Selective implementation of ML-based image enhancement is a potential way forward toward consistency of shape analysis over broader ranges of particle size.

A.6 Derivation of Elliptical Form Factor

The Elliptical Form Factor is analogous to the ISO-defined Form Factor (ISO, 2008), with the difference that it compares the measured perimeter to an area-equivalent *ellipse* instead of a circle. The standard definition of the Form Factor is

$$FF = \frac{4\pi A}{P^2}, \tag{A.3}$$

where A is the measured area and P is the measured perimeter (e.g. by the Cauchy–Crofton method).

The Elliptical Form Factor uses an approximation for the perimeter of an ellipse [80], shown in Eq. A.4, where a and b are the (orthogonal) semi-axes of the ellipse. This simple approximation is accurate for particles that are not severely elongated, i.e. $AR_{\text{box}} > 0.1$ (see Fig. A.13):

$$P_{\text{ellipse}} \approx \pi\Big[1.5(a+b) - \sqrt{ab}\Big]. \tag{A.4}$$

We now rewrite the elliptical perimeter in terms of the particle area A and aspect ratio

$$AR = \frac{b}{a}. \tag{A.5}$$

For an area-equivalent ellipse,

$$A = \pi ab = \pi a^2 AR, \tag{A.6}$$

so we can solve for a and b as

$$a = \sqrt{\frac{A}{\pi\, AR}}, \tag{A.7}$$

$$b = a\, AR. \tag{A.8}$$

Substituting Eqs. A.7A.8 into Eq. A.4 gives

$$\begin{aligned} P_{\text{ellipse}} &\approx \pi \left[1.5 \left(\sqrt{\frac{A}{\pi AR}}(1 + AR) \right) - \sqrt{\frac{A}{\pi}} \right] \\ &= \sqrt{\pi A} \left[\frac{1.5(1 + AR)}{\sqrt{AR}} - 1 \right]. \end{aligned} \tag{A.9}$$

Define the bracketed term as

$$\beta^{1/2} = \frac{1.5(1 + AR)}{\sqrt{AR}} - 1 \quad \Longrightarrow \quad \beta = \left(\frac{1.5(1 + AR)}{\sqrt{AR}} - 1 \right)^2. \tag{A.10}$$

Then Eq. A.9 can be written compactly as

$$P_{\text{ellipse}} \approx \sqrt{\beta \pi A}. \tag{A.11}$$

Finally, the Elliptical Form Factor compares the *area-equivalent elliptical* perimeter to the measured perimeter P in the same way Eq. A.3 compares to a circle, giving

$$EFF = \frac{\beta \pi A}{P^2}. \tag{A.12}$$

Comparing the approximation in Eq. A.11 to the true elliptical perimeter shows that the relative error is negligible for $AR > 0.5$ and remains below about 4% for $AR > 0.1$,

which is within the practical domain for particle-shape characterization in this study (see Fig. A.13).

A.7 Machine Learning for Particle Image Fine-Graining

Limited pixel count has been shown to diminish the accuracy of computed shape factors critical to additive manufacturing powders, such as elliptical form factor and solidity. Regression techniques can be used to perform a baseline correction to these shape factors as a function of the number of pixels in the image. For a population of particles, this corrects the center of the distribution for a shape factor, but still maintains an artificially high amount of variability. To combat the root cause of this issue, machine learning methods can be used to "fine grain," or increase the pixel count of the images by inferring from the surrounding pixels a gradient of threshold values across each of the pixels of the original image [81–83]. This allows each pixel to be magnified, in this case by a factor of 100x.

A 3×3 convolutional window is iterated pixel by pixel across the coarse particle image. The gradient of threshold values for the center pixel is predicted by the algorithm. High resolution training images obtained from the In-Flow were coarse-grained to produce the training and test datasets. The performance of the neural network is shown in Fig. A.16 as predicted vs. actual grayscale value for each of the magnified center pixel values.

In this study, 10,000 particle images were used in the model training set and 2,500 images were used in the validation set. The characteristics of the particle size and shape distribution are critical in determining the procedures for training a deconvolutional model. When creating training data for the machine-learning (ML) model, it is important to utilize high resolution images that reflect the distribution in particle size, perimeter irregularity (EFF), and elongation (AR) of the particles. High resolution images can have been quantified as over 5000 pixels per particle, meaning that there is negligible difference in computed size and shape factors, regardless of orientation [47]. This ensures that the resulting ML model will be able to predict significant differences in the shapes across the breadth of the size distribution.

In principle, ML fine graining can be applied to any particle type and imaging system, with the recommendation of training the fine-graining model for each type of particle investigated. Particles manufactured in different ways can have different archetypal features that can be recognized and resolved by ML. A test for similarity between particle types can be in the comparison of orthogonal shape features that describe variation in sample shape, for example EFF and AR distributions.

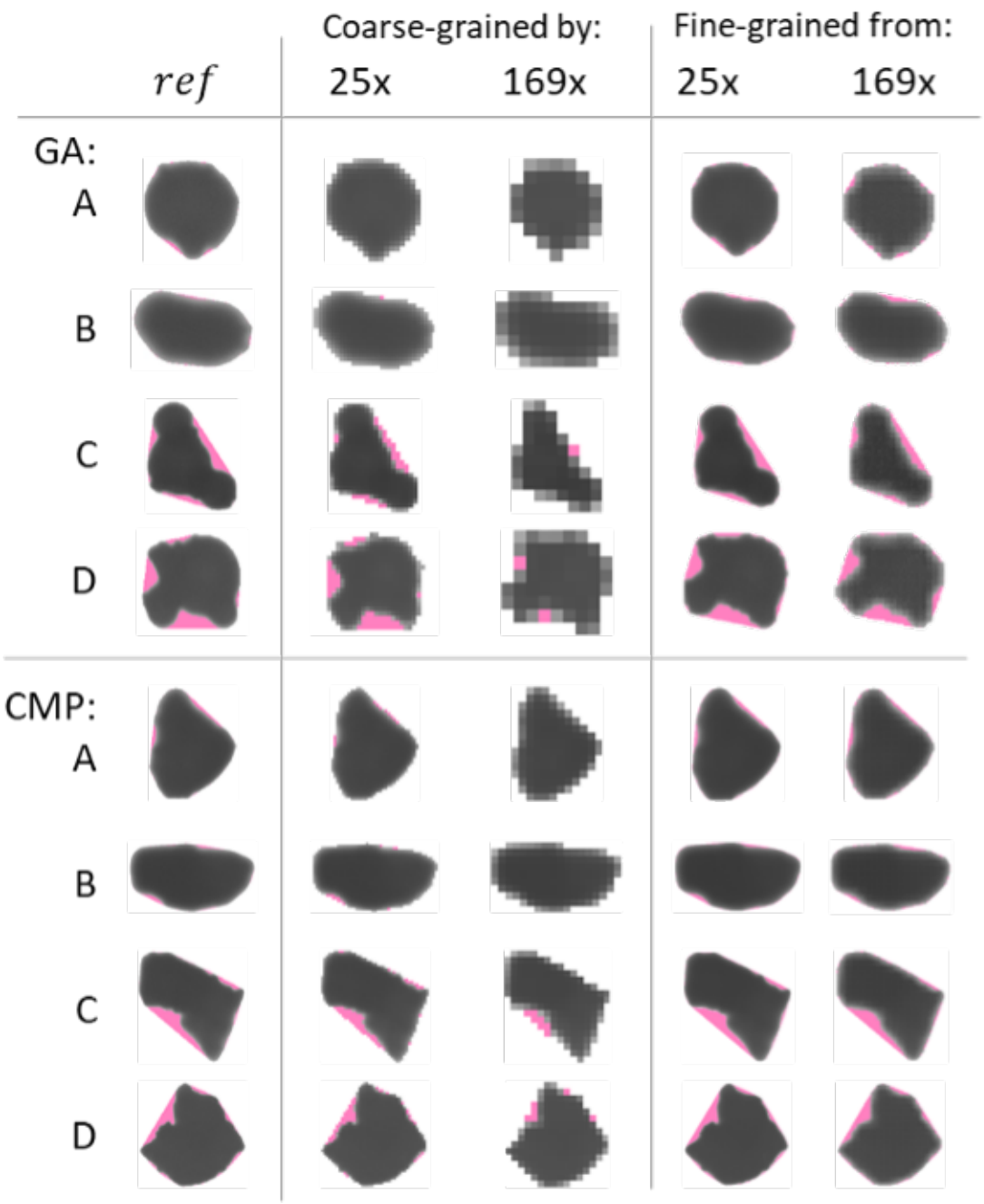

Figure A.8. Examples of coarse graining and machine-learning reconstruction (fine-graining) of thresholded images: particles A–D for each sample are represented on shape maps in Fig. A.6.

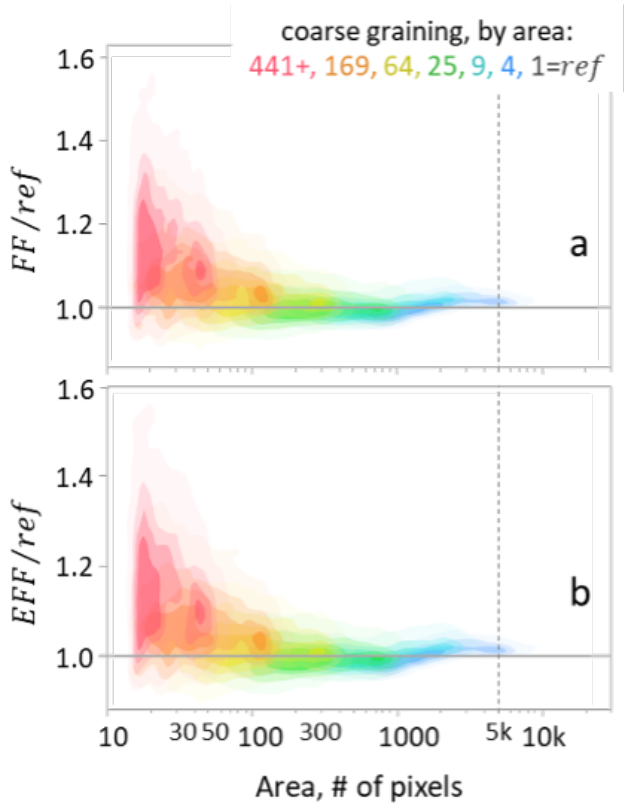

Figure A.9. Coarse graining analysis of Form Factors relative to the reference: (a) ISO definition; (b) bounding box ratio.

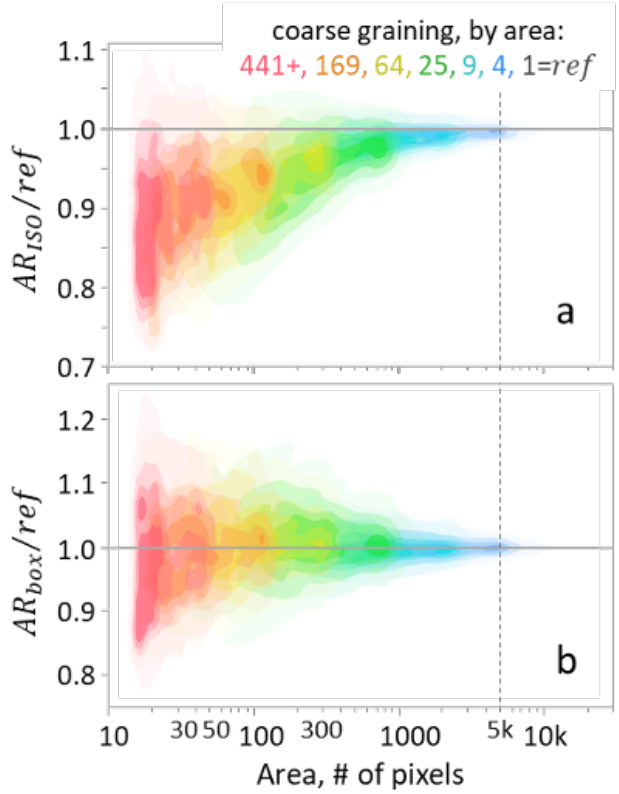

Figure A.10. Coarse graining analysis of Aspect Ratios relative to the reference: (a) ISO definition; (b) bounding box ratio.

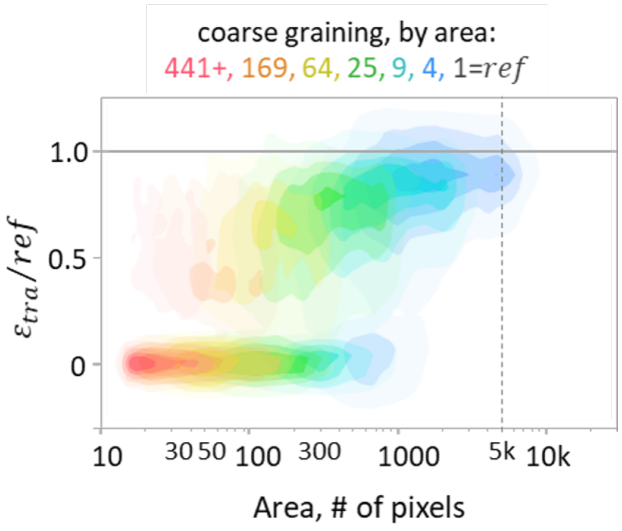

Figure A.11. Coarse graining analysis of intra-particle porosity relative to reference data.

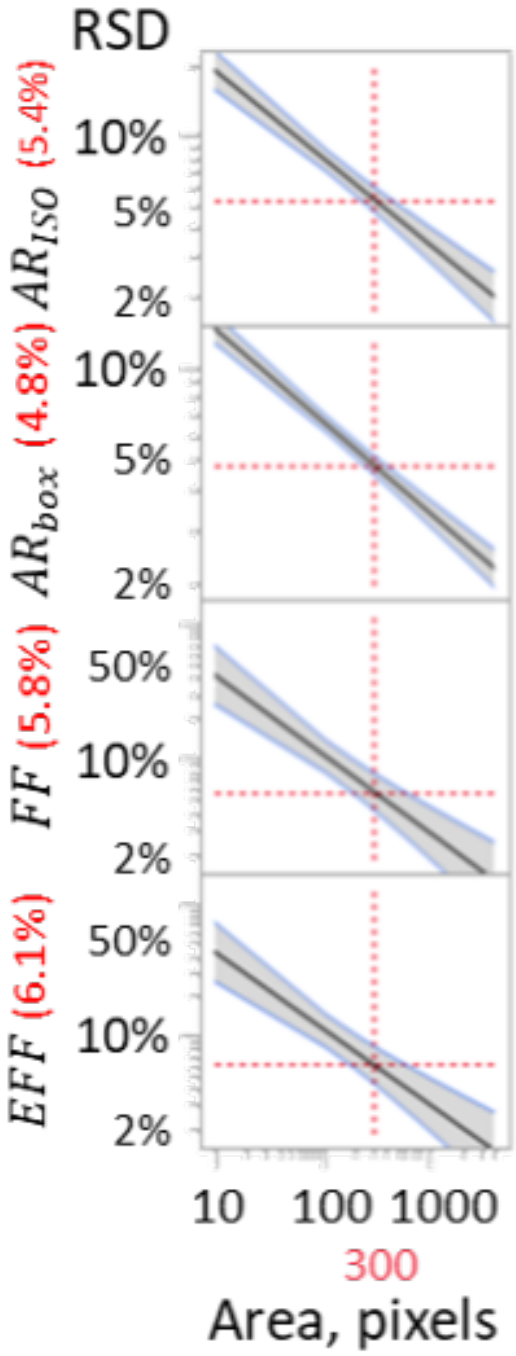

Figure A.12. Shape factor uncertainty with pixilation.

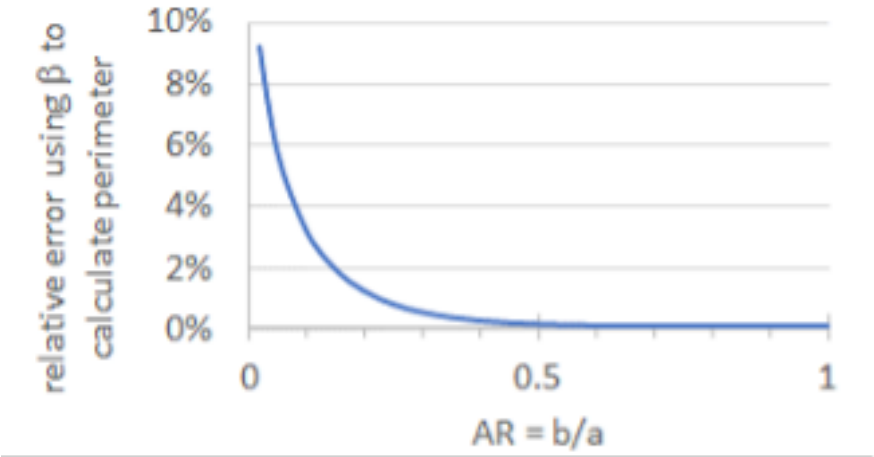

Figure A.13. Relative error of perimeter calculation used in the definition of EFF.

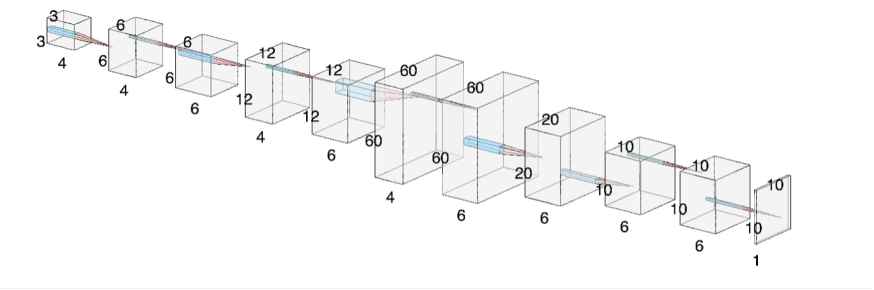

Figure A.14. Neural network architecture, composed of deconvolutional and convolutional layers.

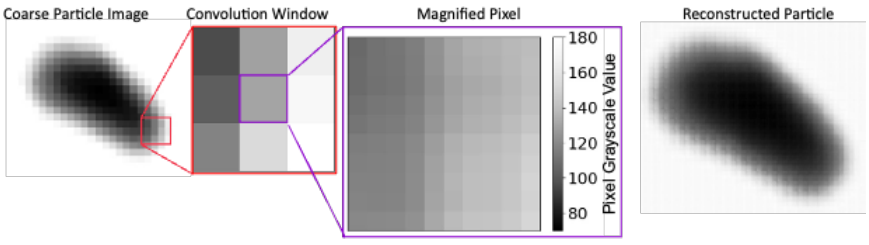

Figure A.15. Convolutional window is input to the neural network, yielding a gradient of threshold values across the center pixel.

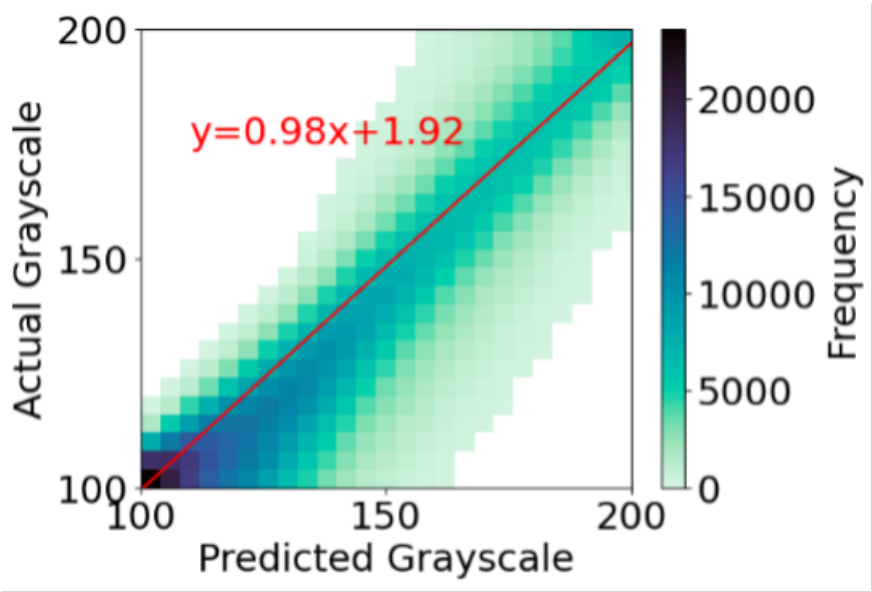

Figure A.16. Parity plot of predicted vs actual pixel gray scale.

B. On the use of the Fourier transform to determine contact curvature distributions in additive manufacturing powders

B.1 Introduction

B.1.1 Reg Davies memorial

During his industrial career, Reg Davies led the Particle Science and Technology group (PARSAT) at the DuPont Experimental Station. In addition to industrial research on particulate processing, PARSAT was well known for its support of process sensing and particulate characterization tools. Reg was a founding member of the International Fine Particle Research Institute (IFPRI) in 1978 and later served as its third president from 1999 to 2002 after his retirement from DuPont. Characterization was at the core of the IFPRI structure, and industrial members have consistently prioritized research work in powder flow, which is often difficult to control and has consequences to solids processing across production scales.

In 2002, IFPRI sponsored a workshop on Powder Flow which led to the formation of a working group, publication of a white paper [84], two IFPRI research projects, and a collaboratory that was co-sponsored by the National Science Foundation. The collaborative project engaged modelers in a challenge to simulate the flow and stress fields of two experimental systems used in the IFPRI programs: 1) a 2D hopper flow (R. Behringer and J. Tang, Duke University) and 2) a continuous Couette flow (G. Tardos and M. Kheripour-Langroudi, City University of New York). One of the lessons learned was to better engage modelers in the design of experiments, especially regarding contact mechanics in dense flows. Of course, insightful modeling relies on characterization – a core capability of the PARSAT organization. This paper reviews particle shape characterization methods relevant to contact mechanics and considers the systematic use of Fourier transforms and curvature analysis as a means of characterizing powders for additive manufacturing.

B.1.2 Challenges in powder-bed additive manufacturing

Additive manufacturing (AM) has found applications across many areas of industry, replacing traditional manufacturing processes and streamlining prototyping efforts. AM

is a hotbed for research activities across all of its unit processes [85]. Studies making, testing, and measuring additively manufactured components have filled technical journals [86]. Much of the work in additive manufacturing is focused on the flexibility of the process to build complicated structures, with work being done in topology optimization and modal analysis of these components [87, 88]. Laser powder bed fusion (LPBF) is an additive manufacturing process that utilizes a movable laser to selectively sinter a metal powder bed. From a materials science perspective, components made with powder bed fusion have a complex microstructure that is greatly affected by processing parameters as well as the original powder size and shape distribution [89, 90]. In addition, the shapes and sizes of the particles have a direct impact on the flowability of the powder. Uniform spreading of the powder bed between layers is imperative to prevent porosity and achieve full sintering of each layer. With that goal, characterization of the powder morphology is critical.

The phenomenological effects of powder size and shape on flow characteristics are well studied. [91] studied pharmaceutical powders, specifically characterizing the effect of area equivalent diameter and circularity on the compressibility and permeability of pharmaceutical tablets. [92] characterized additive manufacturing powders using dynamic image analysis and built discrete element models to test the effect of sphericity of the powder on its performance in the Hall flowmeter, rotating drum, and powder spreading tests, finding that the inclusion of irregularly shaped particles inhibited flow, increased the avalanche angle, and increased the overall roughness of the powder bed. These results point to contact interactions between adjacent particles as a crucial mechanism in modeling powder flow. In order to understand how inter-particle contact forces manifest, the geometry of both contacting particles local to the contact area is critical. Resolving a distribution in potential contact radii is not trivial. A high-resolution image of a particle can act as a vehicle for determining detailed information about its shape and contact properties.

Dynamic image analysis (DIA) is an effective method for characterization of powder size and shape distributions. In DIA, particles flow between a camera and backlight, and grayscale images are captured. The images are thresholded, and information about each particle's size and shape is extracted, often using ISO-defined metrics such as area equivalent diameter, minimum and maximum Feret lengths, form factor, and aspect ratio [47]. This

information can be used to validate manufacturing processes and can be used in physics-based simulations, such as discrete element method-based approaches, to assess process predictability [93].

In our prior work, we used DIA to examine a pair of aluminum Al7075 powders that were created by different manufacturing processes [5]; one by gas atomization (GA) and one by a cold mechanical process (CMP), also referred to as milled or cut-milled for ease of notation. We identified archetypal differences between the powders, examined the effect of pixelation on the measurements of area and perimeter, and utilized principal component analysis to create shape factor clusters that best described the differences between the two. In general, particles made by gas atomization tended to be more spherical with occasional satellites formed during the production process when a molten particle collides with a solidified one. The CMP particles tended to have more straight edges and corners, features associated with the cut-milling process. Both powders used in this study were viable for creating robust LPBF parts [94].

B.1.3 Challenges in particle shape characterization

Per ISO 9276-6 [47], the form factor compares the measured perimeter of the particle to the perimeter of a perfect circle with the same area as the particle. The minimum and maximum feret lengths measure the minimum and maximum lengths between parallel tangent lines on a particle's perimeter. Extent is defined as the area of the particle divided by the product of the minimum and maximum feret lengths. The elliptical form factor (EFF) is an auxiliary shape factor that is analogous to the ISO-defined form factor [5]. EFF compares the perimeter of the particle to the perimeter of an ellipse with the same aspect ratio and area. EFF is orthogonal to the aspect ratio. When coupled, the aspect ratio measures the elongation of a particle while EFF measures irregularity. The area is a relatively straightforward measurement, measured as the number of thresholded pixels multiplied by the per-pixel area. Perimeter is considerably more difficult to compute. To some extent, the measured perimeter depends on the resolution of the measurement camera (commonly known as the coastline paradox [95]), and if the perimeter was measured by adding the

exposed edge length of all perimeter pixels, this behavior would be prevalent. Modern DIA systems often utilize Cauchy-Crofton smoothing techniques [47, 75, 78] to extract an approximate perimeter of the particle that can be less sensitive to resolution. A mismatch is created in this case, where the area and perimeter are computed using different methods and a commensurable comparison cannot be made between the two. A consequence is that for low-resolution particles, the computed form factor often yields an illogical (> 1) value. In our previous work, we showed that decreases in image resolution lead to an artificial increase in the computed roundness of the particles. Around 300 pixels per particle was identified as a threshold to reliably measure particle shape. We circumvented this issue with the use of a deconvolutional neural network to artificially increase the resolution of images, a technique referred to as fine graining that is purely computational.

Existing shape factors provide valuable information about the shape of a particle but do not tell the whole story. They generally describe the similarity of the particle to an idealized circle or ellipsoid but provide very little information about the features of the particle's edge that could be relevant in mechanical contact. Utilizing the Fast Fourier Transform (FFT) to generate an expression for the edge of the particle can provide detailed information about particle features in a reduced-order format consistent with the ethos of DIA.

B.1.4 Fourier Transform Background

The Fourier transform is a standard tool in signal analysis, providing a means for describing the composition of a complex waveform in terms of its contributions from individual frequencies[1]. Fundamentally, the FFT leverages Euler's formula to represent a periodic function in the time domain ($f(t)$), in the frequency domain. $\hat{f}(n)$ is a complex-valued function that describes the degree to which the n-th harmonic is present in $f(t)$, where $|\hat{f}(n)|$ is the amplitude of the n-th harmonic. A detailed discussion of the mathematical background for the FFT is provided in B.7.

The concept of using FFTs to formulate a reduced-order description of particle perimeters goes back many years and was of interest during Reg Davies' collaboration with Terry

[1]↑Note that the terms "Fourier modes", "Harmonics", and "Frequencies" are used interchangeably to refer to a waveform with a period of P/n, where P is the parameterized perimeter.

Allen at Dupont [96]. At the time, there was a lot of promise in the application of FFTs toward the systematic description of perimeter outlines with respect to particles' center of mass, i.e., as relevant to contact mechanics. On the other hand, more complex shapes with re-entrant features could not be fully described using the method. Much of the prior work in using the Fourier transform to represent particles is in the field of sedimentology. The technique was originally described by [97], where the authors provided a method to determine the quality of the Fourier series reconstruction and quantified the roundness of the particles based on the difference between the area equivalent circle and the reconstructed particle. The method was also described by [98] and [99]. A later work by [100] reconstructed six types of particles, ranging from construction aggregate to steel ball bearings, and noticed a power law relationship between the magnitude of the n-th Fourier coefficient and n, while citing Reg Davies' work in particle shape characterization [101].

Recent work on applying the Fourier transform particle reconstruction method has focused largely on quantifying a particle's form, roundness, and texture from the presence of harmonics in its reconstruction. [102] developed a freeware toolkit, called FSA, to perform Fourier particle reconstruction and quantitatively represent particle morphology using the fitted Fourier modes. The authors suggested that low-frequency harmonics describe the particle's overall form, medium-frequency harmonics capture roundness and features, and high-frequency harmonics illustrate the surface texture of the particle, but noted that distinguishing a harmonic between low, medium, and high is an observational endeavor. It was noted by [103] and [104] that inferring information about surface texture from high-frequency harmonics can be highly inconsistent. As the period length of the harmonic approaches the pixel length scale, aliasing due to pixelation of the perimeter (B.7, [105] and distortion at the edges due to light diffraction can strongly affect the results of the modal analysis.

The Fourier series approach has also been extended to construct three-dimensional models of particles from X-ray microtomography measurements using spherical harmonics. For example, [106] and [107] characterized construction engineering materials such as crushed rocks, silica sand, and ground granulated blast furnace slag, while [108] proposed shape factors to quantify sphericity, roundness, and maximum dimensions based on spherical harmonic coefficients.

This report reconsiders the use of the Fourier transform for powder size and shape analyses, applying the method to LPBF AM powders and utilizing a parameterized approach that allows for the misshapen and agglomerated particles to be captured. One goal of this work is to demonstrate compatibility between the Fourier transform approach and existing ISO-defined shape factors, a critical benchmark for evaluating its potential uses. Moreover, the Fourier transform approach facilitates the semi-analytical calculation of surface curvature, an integral part of contact mechanics that is directly relevant to the spreading flows and packing environments that are prevalent in AM. A procedure for computing contact curvature will be outlined and distributions therein will be analyzed for the AM powders.

B.2 Particle reconstruction with Fourier Transforms

B.2.1 Parameterization

To apply the FFT algorithm to reconstruct two-dimensional particle projections and quantify curvature, the boundary of the particle needs to be represented as a waveform that is compatible with the Fourier transform requirements of single-valued and continuous. This requires the identification of the particle's centroid and perimeter. The centroid of a particle can be computed as the average locations of all pixels within the particle meeting the threshold criteria:[2]

$$\bar{x} = \frac{1}{N}\sum_{\mathrm{i}=1}^{N} x_{\mathrm{i}} \quad and \quad \bar{y} = \frac{1}{N}\sum_{\mathrm{i}=1}^{N} y_{\mathrm{i}} \tag{B.1}$$

The particle's perimeter is comprised of edge pixels, the details of which are described in B.8. The coordinate system of the edge can then be converted from cartesian, which comes naturally from the grid of pixels to a polar coordinate system with an origin at the centroid, creating a waveform that describes the edge of the particle, $R(\theta)$.

$$R = \sqrt{(x-\bar{x})^2 + (y-\bar{y})^2} \quad and \quad \theta = cos^{-1}(\frac{(x-\bar{x})}{R}) \tag{B.2}$$

[2]↑In the current work, the JM Canty In-Flow system was used to capture back-lit particle projections using grayscale (0-255) imaging. Pixels composing particles were in the range 0-170, and background > 170.)

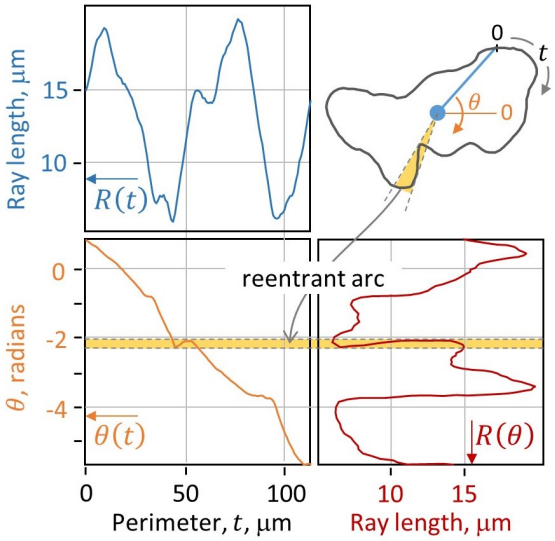

Figure B.1. Real and parameterized representations of the particle perimeter, showing re-entrant arc condition.

The simplest application of the FFT to capture particle shape is with particles fitting the star-shaped archetype. According to [108] and [109], a particle is star-shaped if there is a fixed point within that can be connected to any other point within the particle by a straight line that does not leave the domain of the particle. For reconstructing particles and curvature analyses, it is particularly salient whether the centroid satisfies the star-shaped fixed point condition. Note that the definition of a star-shaped archetype does not necessarily imply that the particles look like stars. Sphere-like particles are trivially star-shaped, where $R(\theta)$ is single-valued at all points. While the majority of particles from the milled and gas-atomized samples considered in this study fit the star-shaped archetype, there are exceptions that have re-entrant features.

Figure B.1 is an example of a reentrant particle. The blue ray connects the centroid with the perimeter at location $t = 0$;[3] subsequent rays are evaluated in a clockwise progres-

[3]↑By convention, the cartesian grid of pixels comprising the particle has an origin (0,0) at the upper left corner, and the initial position of the perimeter trace, $t = 0$, is defined as the highest, leftmost particle pixel on the particle perimeter.

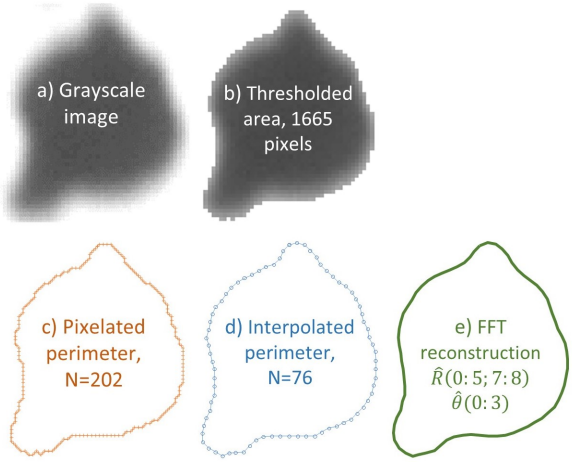

Figure B.2. Particle reconstruction procedure. Images are thresholded, then their edges are traced and interpolated. The interpolated particle edge is used for the FFT reconstruction method.

sion as a function of θ (real) or t (parameterized). A ray trace is reentrant if it passes through the boundary of the particle at multiple instances of the particle's perimeter, meaning $R(\theta)$ is multivalued in those regions. Agglomerated particles often project as complex shapes that qualify as reentrant. As was pointed out by [110], particles with reentrant features require a parameterized approach to be reconstructed with Fourier transforms. For consistency, all particles considered in this report were evaluated using the parameterized approach.

An intuition for parameterization would be to imagine that the perimeter of the particle is a race track that a runner is jogging one lap around. The runner can complete one lap around the particle at a constant pace of 1 pixel/s. To fully describe the runner's position, their location can be specified in the spatial domain (θ, R) or in the temporal domain $(\theta(t), R(t))$ by plotting how far the runner is from the centroid as a function of time. Parameterizing the radius and angle presents a projection of the particle's edge that guarantees that the single-valued condition is met and the particle can be reconstructed with the FFT analysis. For the purpose of particle imaging, parameterization on the basis of perimeter length is a logical choice. $s(t)$ is a function that fully describes the angular and

radial path of the edge of the particle according to position along the perimeter length. A discussion of this technique is included in B.8.

$$s(t) = \begin{bmatrix} \theta(t) \\ R(t) \end{bmatrix} \tag{B.3}$$

The difference between the parameterized and real projections is shown in Figure B.1, where $\theta(t)$ acts as a map between the projections of the radius that allows for any point in the parameterized domain, $R(t)$, to be mapped to its corresponding point in the real domain, $R(\theta)$.

The particle reconstruction yielded by the FFT procedure is partially determined by the way that the edge is discretized. The reference points that compose $R(t)$ and $\theta(t)$ must be equally spaced based on particle perimeter. In-kind, delineating an approximate edge of the particle is pertinent. We have chosen to use the center points of exposed edges as linear interpolation points for the perimeter (Figure B.2c). The total length of the perimeter is initially approximated as the summation of the length of the interpolated line segments defined using edge midpoints of perimeter pixels. Equidistant reference points for $R(t)$ and $\theta(t)$ can then be evaluated on the interpolated perimeter (Figure B.2d). The number of reference points also affects the quality of the reconstruction. Coarse approximations can inhibit the FFT analysis from capturing relevant features of the particle. The necessary degree of discretization depends on the resolution of the particle. For a detailed discussion of this procedure, refer to B.8.

Taking the FFT of $R(t)$ supplies a set of Fourier coefficients for harmonics ranging from $(1-N)/2$ to $(N-1)/2$, where N is the number of reference points (B.7). $\hat{R}(n)$ is the frequency domain representation of the particle's edge.

$$\hat{R}(n) = \mathcal{FFT}(R(t)) \tag{B.4}$$

$R(t)$ is naturally periodic, meaning $R(0) = R(P)$ where P is the total parameterized perimeter length, lending itself to representation with the Fourier transform. On the other hand, the linear form of $\theta(t)$ is aperiodic ($\theta(0) \neq \theta(P)$), meaning $\theta(t)$ is discontinuous at

P and is therefore incompatible with the FFT's requirements. $\theta(t)$ can be broken into two components, an average slope that is aperiodic and has a value of $\theta_a(t) = \frac{-2\pi t}{P}$, and a periodic component that encompasses all deviations from the average slope, $\theta_p(t) = \theta(t) + \frac{2\pi t}{P}$. Analogous to $\hat{R}(n)$, $\hat{\theta}_p(n)$ is the frequency domain representation of the periodic component of $\theta_p(t)$:

$$\hat{\theta}_p(n) = \mathcal{FFT}(\theta_p(t)) \tag{B.5}$$

$\hat{R}_{Total}$ and $\hat{\theta}_{Total}$ represent the total cumulative magnitudes of all Fourier coefficients. The calculation for the magnitude of a Fourier coefficient is of the general form $|\hat{f}(n)| = \sqrt{a_n^2 + b_n^2}$.

$$\hat{R}_{Total} = \sum_{n=0}^{N-1} |\hat{R}(n)| \quad \text{and} \quad \hat{\theta}_{Total} = \sum_{n=0}^{N-1} |\hat{\theta}_p(n)| \tag{B.6}$$

Aliasing of high-frequency modes (B.7, [105] and light diffraction in the DIA process can cause uncertainty in the precise location of the edge of the particle, meaning using the FFT method to precisely measure surface roughness from an image can be dubious. Rather than reconstructing the particle's edge exactly with the inverse FFT of the frequency domain representation, the particle can be reconstructed approximately by recursively adding harmonics until a threshold accuracy (T) is reached (Figure B.2e). First, the frequency domain representation of the particle edge is reindexed in a monotonically decreasing order, according to the magnitude of the Fourier coefficients. Denote this sequence n' such that: $|\hat{R}(n'_0)| > |\hat{R}(n'_1)| > ... > |\hat{R}(n'_{N-1})|$. Then, the set of Fourier modes with a magnitude greater than $T * \hat{R}_{Total}$ ($T \in (0, 1)$) can be summed to form a smoothed representation of the particle's edge. The number of Fourier modes needed for the $R(t)$ reconstruction is X_R:

$$X_R = min\{X \in [0; N-1] : |\hat{R}(n'_X)| \leq T * \hat{R}_{Total}\} \tag{B.7}$$

$\tilde{R}(t)$ is a smoothed version of the particle's edge, reconstructed to the threshold accuracy.

$$\tilde{R}(t) = \sum_{\mathrm{i}=0}^{X_R} \hat{R}(n'_\mathrm{i}) \mathrm{e}^{-2\pi \mathrm{i} n'_\mathrm{i} t} \tag{B.8}$$

$\hat{\theta}_p(n)$ can similarly be reindexed with m' such that $|\hat{\theta}_p(m'_0)| > |\hat{\theta}_p(m'_1)| > ... > |\hat{\theta}_p(m'_{N-1})|$. X_θ is the number of Fourier modes needed to reconstruct $\theta(t)$ to a threshold accuracy T:

$$X_\theta = min\{X \in [0; N-1] : |\hat{\theta}_p(m'_X)| \leq T * \hat{\theta}_{Total}\} \tag{B.9}$$

$\tilde{\theta}(t)$ is a smoothed version of $\theta(t)$. The average slope ($\theta_a(t)$) is added to the Fourier series representation of $\theta_p(t)$.

$$\tilde{\theta}(t) = \frac{-2\pi t}{P} + \sum_{i=0}^{X_\theta} \hat{\theta}_p(m'_i) e^{-2\pi i m'_i t} \tag{B.10}$$

Note that neither m' and n' nor X_θ and X_R are identically equal. In this study, the LPBF powders were reconstructed with all harmonics with a coefficient of at least 0.4% of the total magnitude of their Fourier series representation. B.8 includes a discussion of reconstruction accuracy on the basis of perimeter length.

For many applications, capturing the overall form and critical features is more important than measuring surface texture. This allows for a significant reduction in information from a full field image to a summation of a few Fourier modes that accurately represent the particle. Reconstruction examples are shown in B.8, Figures A.13 and B.11. $\tilde{s}(t)$ is the approximate FFT reconstruction of the particle.

$$\tilde{s}(t) = \begin{bmatrix} \tilde{\theta}(t) \\ \tilde{R}(t) \end{bmatrix} \tag{B.11}$$

B.2.2 Application to AM powders

Distributions in the number of modes needed for reconstruction of $R(t)$ and $\theta(t)$ are shown in Figure B.3, separated by powder type[4]. For the milled powder, the mean of X_R was 8.95, with a standard deviation of 1.55, while for the gas atomized the mean value of X_R was 8.14 with a standard deviation of 2.28. For a significant portion of gas atomized particles, $R(t)$ was reconstructed with seven or fewer harmonics, owing to their round archetypal profile which is an artifact of their manufacturing process. Relatively few CMP particles

[4]↑The volume of each particle is approximated from two-dimensional projections using area equivalent radius, assuming a spherical archetype ($V = (4A^{3/2})/(3\sqrt{\pi})$).

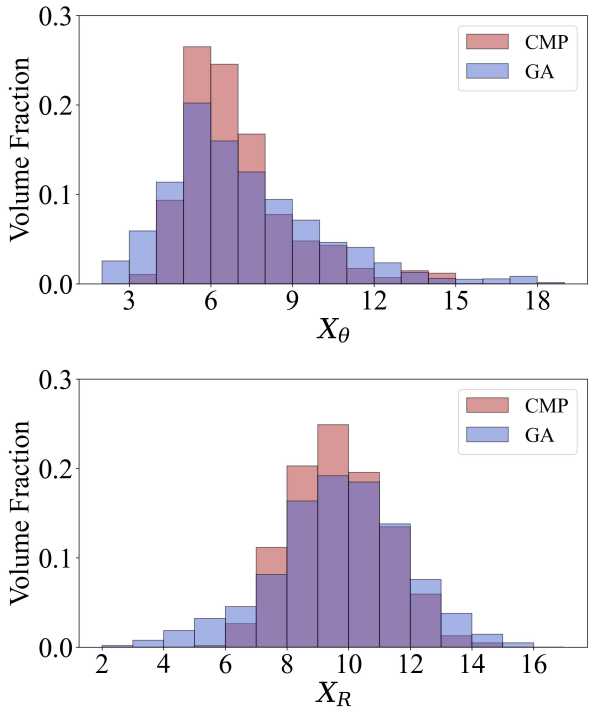

Figure B.3. Volume weighted distributions in the number of Fourier modes needed to achieve incremental tolerance of 0.4% of $\hat{R}_{Total}$ and $\hat{\theta}_{Total}$.

were reconstructed with less than seven harmonics, due to the effect of mechanical processing on shape.

Similarly, the mean value of X_θ was 6.41 for the milled powder and 5.74 for the gas-atomized population, with standard deviations of 2.11 and 2.64 respectively. Overall, the distribution in both X_R and X_θ were broader for the gas-atomized particles, with a lower mean number of harmonics.

Figure B.4 is a sample of three gas-atomized particles that conform to three archetypal profiles. Particle A is nearly spherical, particle B is aspherical but fits the generalized star-shaped archetype, while particle C is re-entrant. Mapping out the $\tilde{\theta}(t)$ parameterization of the three particles (orange line) shows that particle A is nearly linear, as it would be for a perfectly spherical particle. The star-shaped archetype is monotonically decreasing, but its rate varies with respect to position on the perimeter. The reentrant particle is neither linear

nor monotonically decreasing, which is an alternative indicator for determining if particles qualify as reentrant. The ray length plots (blue) show the parameterized radius, $\tilde{R}(t)$, of the three particles based on perimeter length. The particle perimeters are shown as $\tilde{s}(t)$ reconstructions, overlaid with area-equivalent circles (red). Curvature, κ, is plotted in green with numbered peaks corresponding to features shown on the perimeter traces; note the local curvature distribution is centered around that area-equivalent circular curvature, κ_A.

Figure B.5 is a sample of a CMP particle having about the same size and form factor as the gas-atomized particle in Figure B.4B. The CMP particle has more linear edges with periodic corners, consistent with a cutting process. This is characterized by a higher positive skew in the particle's curvature distribution.

In both the GA and CMP cases, parameterized perimeter reconstructions, $\tilde{s}(t)$, enable direct calculation of local curvature distributions, described in more detail in Sections B.4 and B.5.

B.3 Characteristic Harmonics and Shape Factors

Principal component analysis (PCA) is a data analytics technique aimed at reducing the dimensionality of a complex dataset through coordinate transformation [111].

Consider a dataset of particle shape measurements x_{ij}, where each row contains the shape factors of the i-th particle. In PCA, the data are standardized according to the mean (μ_{j}) and standard deviation (σ_{j}) of the j-th column, $z_{\mathrm{ij}} = (x_{\mathrm{ij}} - \mu_{\mathrm{j}})/\sigma_{\mathrm{j}}$. The covariance matrix $\mathbf{C}$ is computed based on the standardized data matrix $\mathbf{Z}$ and the number of samples n:

$$\mathbf{C} = \frac{1}{n-1}\mathbf{Z}^T\mathbf{Z} \tag{B.12}$$

The covariance matrix is symmetric, with size $J \times J$, where J is the number of shape factors, positive semi-definite, and has diagonal elements $C_{\mathrm{jj}} = \sigma_{\mathrm{j}}^2$. The off-diagonal values of the covariance matrix describe correlations between factors. $C_{\mathrm{ij}} > 0$ indicates that the i-th and j-th factors tend to be positively correlated, while $C_{\mathrm{ij}} < 0$ denotes negative correlation, and

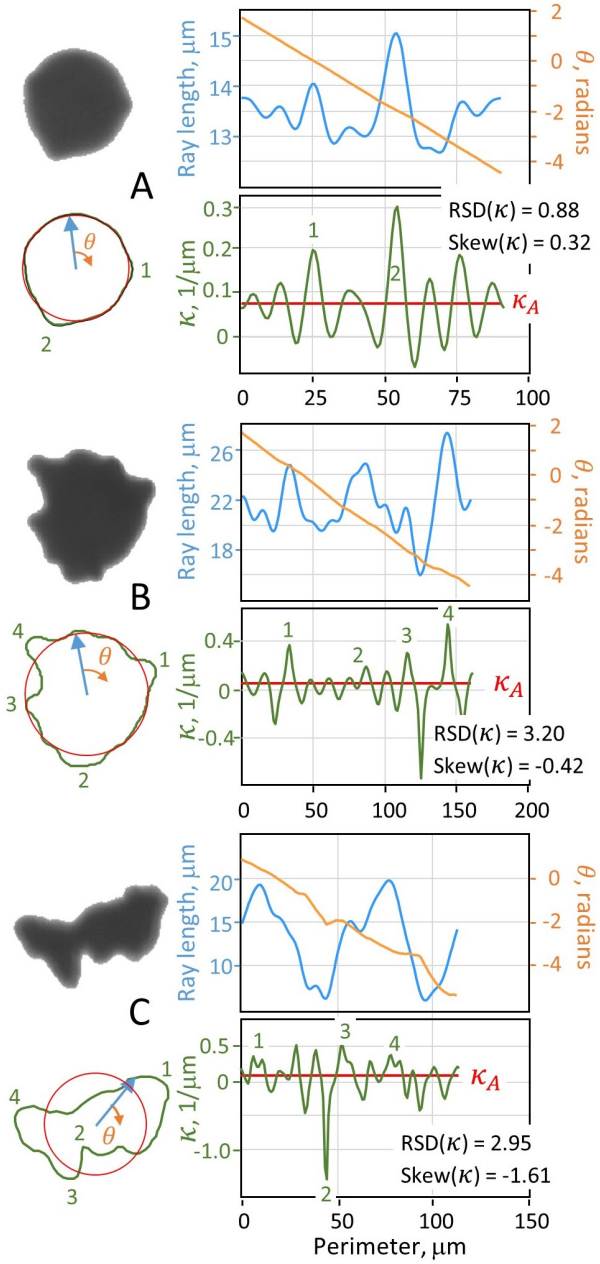

Figure B.4. Parameterized angle functions and curvature distributions for A. Nearly Spherical B. Star-shaped and C. Reentrant gas atomized particles.

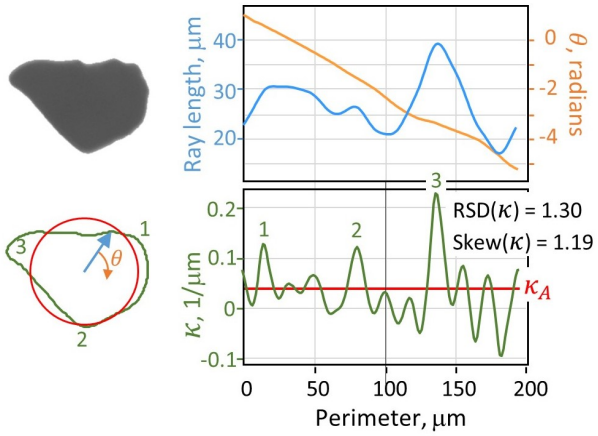

Figure B.5. Parameterization and contact curvature analyses a milled particle with a similar size and shape factor profile to Particle B in Figure B.4.

$C_{ij} \approx 0$ signifies linear[5] independence or a lack of correlation. Correlation coefficients (ρ_{ij}) between shape factors were computed from the covariance matrix using the row-wise method [112].

$$\rho_{ij} = \frac{C_{ij}}{\sqrt{C_{ii} \cdot C_{jj}}} \tag{B.13}$$

The covariance matrix's eigenvectors represent the dataset's principal directions (the directions that capture the largest amount of variability), acting as a set of orthogonal unit vectors for the construction of an orthonormal coordinate system. The corresponding eigenvalues represent the amount of variance captured in each principal direction. In PCA, a coordinate system is defined using only the principal directions with the largest eigenvalues. Each shape factor can then be projected onto the new coordinate system. As with the covariance matrix, orthogonality between the projections of two factors marks linear independence between the factors. All computations of covariance matrices, correlation coefficients, and principal component analyses were performed in JMP Pro 16 [113].

[5]↑A covariance value of zero always guarantees linear independence. If two factors are approximately Gaussian in distribution, a covariance value of zero implies complete independence.

Table B.1. Features for shape analysis. Feret lengths are distances between parallel tangents. Form factors relate area to perimeter equivalents; β adjusts perimeter from circular to elliptical equivalents [5].

Feature	Description
A	area
P	perimeter (interpolated)
x_{Fmin}	minimum Feret length
x_{LF}	Feret length orthogonal to x_{Fmin}
AR_{box}	aspect ratio, x_{Fmin}/x_{LF}
FF	form factor, $4\pi A/P^2$
EFF	elliptical form factor, $\beta\pi A/P^2$
β	$[(1.5 \times (1+AR)/\sqrt{AR}) - 1]^2$

In our previous work [5], we performed a PCA on a set of shape factors comprising ISO-defined factors and modifications thereof. The analysis provided some degree of differentiation between gas-atomized (GA) and milled (CMP) LPBF powders. While the gas atomized powder had a mode that was rounder and more equiaxed on average than the milled sample, it had a tail that overlapped the milled sample features. That PCA reduced the dimensionality of the factor space to two and showed that EFF and AR_{box} were orthogonal basis vectors sufficient to define the principal component plane. A summary of image analysis descriptors and relevant shape features is shown in Table B.1.

To illustrate the physicality of the Fourier modes, it is worth noting that the zeroth harmonic, also known as the zero offset, is a special case. As is shown in Equation B.39, when $n = 0$, the exponential term is equal to 1 for all values of t, shown in Equation B.14. The discrete approximation of the integral yields an arithmetic average of the distances of all of the reference points from the centroid. Hence, the Fourier coefficient for the zeroth harmonic only has a real component and its value converges to the area equivalent radius for star-shaped particles, but can differ due to reentrant features.

$$\hat{R}(0) = \int_0^1 (R(t))dt = \frac{1}{N}\sum_{n=0}^{N-1} R(t_n) \tag{B.14}$$

In deriving comparable shape factors from Fourier coefficients, normalization by the magnitude of the zeroth harmonic is a necessary step to ensure that the factor is dimensionless. Two such shape factors are defined in Equation B.15, $\hat{R}_2^*$ and $\hat{R}_{3:N}^*$. $\hat{R}_2^*$ aims to be an analog of aspect ratio, equating the degree of elongation of a particle to the normalized magnitude of its second Fourier coefficient.

$\hat{R}_{3:N}^*$ is designed to be related to EFF. Summing the normalized magnitude of all Fourier coefficients greater than the second harmonic captures the prominence of features present on the edge of the particle that do not contribute to elongation. $\hat{R}(1)$ is asymmetric and primarily represents translation or rotation rather than prominent shape characteristics. The omission of $\hat{R}(1)$ ensures $\hat{R}_{3:N}^*$ is not sensitive to particle orientation, and only captures meaningful geometric features on the particle's edge. As discussed in B.7, since $R(t)$ is real-valued, its Fourier coefficients for corresponding positive and negative frequencies have symmetric conjugates and identical magnitudes. Consequently, it is sufficient to consider only positive frequencies in shape factor definitions. Figure B.6 is an augmentation of that PCA, including $\hat{R}_2^*$ and $\hat{R}_{3:N}^*$.

$$\hat{R}_2^* = \frac{|\hat{R}(2)|}{|\hat{R}(0)|} \quad \text{and} \quad \hat{R}_{3:N}^* = \sum_{\substack{\mathrm{i}=0 \\ n_\mathrm{i}' \notin \{0,1,2\}}}^{X_R} \frac{|\hat{R}(n_\mathrm{i}')|}{|\hat{R}(0)|} \tag{B.15}$$

Table **??** shows the correlation coefficients between each of the shape factors. $\hat{R}(2)^*$ and AR_{box} are strongly inversely related, with a correlation factor of -0.95. The second harmonic resembles an elongated ellipsoid with two lobes. Particles with a dominant second harmonic are more elongated and, hence have a lower aspect ratio. In comparison to the aspect ratio, $\hat{R}(2)^*$ shares slightly stronger correlations with both form factor and elliptical form factor, while both AR and $\hat{R}(2)^*$ are weakly correlated with $\hat{R}_{3:N}^*$.

$\hat{R}_{3:N}^*$ is inversely proportional to the elliptical form factor (EFF) ($\rho = -0.90$), indicating that the presence of these harmonics decreases the EFF of the particle. Previous work has suggested that so-called low-frequency harmonics determine features present in the particle reconstruction [102]. The harmonics with magnitudes greater than $T \cdot \hat{R}_{Total}$ represent a sweet spot for consequential contact features because they describe relatively low-frequency

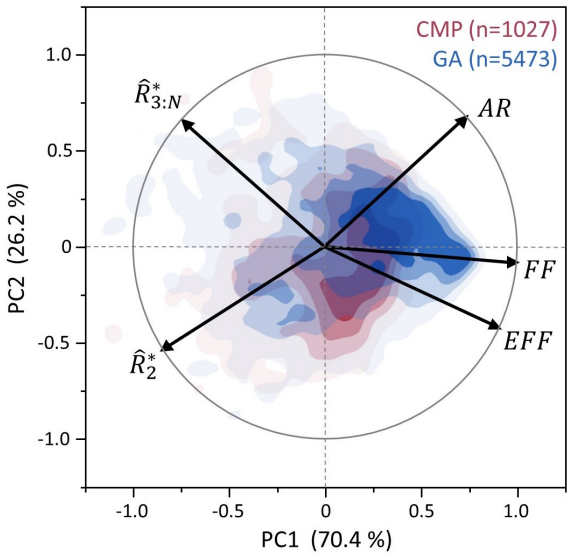

Figure B.6. Volume-weighted principal component analysis showing a comparison of commonly-used shape factors with normalized magnitudes of Fourier coefficients for gas atomized (GA) and milled (CMP) additive manufacturing powders.

Table B.2. Correlation factors between shape factors, estimated using the row-wise method. Clusters of correlated shape factors are grouped by color shading.

	AR_{box}	$\hat{R}_2^*$	FF	EFF	$\hat{R}_{3:N}^*$
AR_{box}	1.00	-0.95	0.72	0.45	-0.34
$\hat{R}_2^*$	-0.95	1.00	-0.81	-0.57	0.39
FF	0.72	-0.81	1.00	0.93	-0.80
EFF	0.45	-0.57	0.93	1.00	-0.90
$\hat{R}_{3:N}^*$	-0.34	0.39	-0.80	-0.90	1.00

departures from the area equivalent circle. These harmonics interact to depict the general form of the particle without capturing high-frequency noise at the edges.

Two clusters of highly correlated shape factors were established. The values of AR, $\hat{R}_2^*$, and FF correspond to the elongation of a particle, while EFF, $\hat{R}_{3:N}^*$, and FF vary with the irregularity of a particle. FF's presence in both clusters demonstrates its utility as a single-factor, holistic shape metric. All in all, this investigation confirms the congruity between the Fourier analysis and traditional shape factors.

B.4 Local Curvature Analysis

The PCA showed that a reduction of selected Fourier modes is consistent with legacy shape factors. In addition, the FFT approach enables more detailed analyses of particle shape and shape distributions, specifically relating to symmetry and curvature. For example, understanding contact interactions between particles is essential in modeling the movement and flow of powder beds in additive manufacturing. Force chain networks affect stress transmission and packing uniformity in spreading. The distribution and magnitude of stress

networks depend on the size and shape of particles, specifically the curvature at contact interfaces.

Analytical solutions for contact systems are commonly based on the Mindlin and Boussinesq solutions for a point force in an infinite, linear-elastic halfspace coupled with the superposition principle [114]. For basic geometries such as two spheres, the Hertz contact approach [18] offers exact solutions for displacements, stresses, and strains in both bodies. For particles that are not ellipsoidal, analytical solutions to the contact problem are often unavailable. In discrete element simulations, irregularly shaped particles are approximated as spheres of the particles' volume equivalent diameter, or formed from composite shapes such as glued spheres. These approaches allow for standard contact models such as Hertz to be used while accounting for irregular shapes.

An analogy to the glued spheres approach can be drawn for arbitrary particles measured by DIA by considering the instantaneous trajectory of $\tilde{s}(t)$ at all points on the particle's edge. This concept is illustrated intuitively in Figure B.7., where the instantaneous rate of change of the tangent vector to the perimeter ($\frac{d^2\tilde{R}(t)}{dt^2}$) at point 7 is significantly higher than at point 1. If the trajectory of the tangent ($\frac{\tilde{R}'(t)}{|\tilde{R}'(t)|}$) and its derivative ($\frac{\tilde{R}''(t)}{|\tilde{R}''(t)|}$) were extrapolated, the corresponding orange circles would be drawn, with a radius equal to the radius of curvature at that point. Curvature is defined as the reciprocal of the radius of curvature. Curvature has been previously explored in particle imaging, such as recent work by [115] that utilized a spline interpolation scheme to produce curvature plots aimed at quantifying corners and angularity. In this work, an analytical form of curvature based on the parameterized Fourier transform edge reconstruction is derived.

Table B.3. Curvature and ROC values for the annotated particle in Figure B.7.

	Radius (μm)	κ (μm^{-1})
Area Eq.	14.1	0.071
1	6.70	0.15
2	5.88	0.17
3	6.25	0.16
4	4.34	0.23
5	3.23	0.31
6	7.70	0.13
7	1.06	0.94

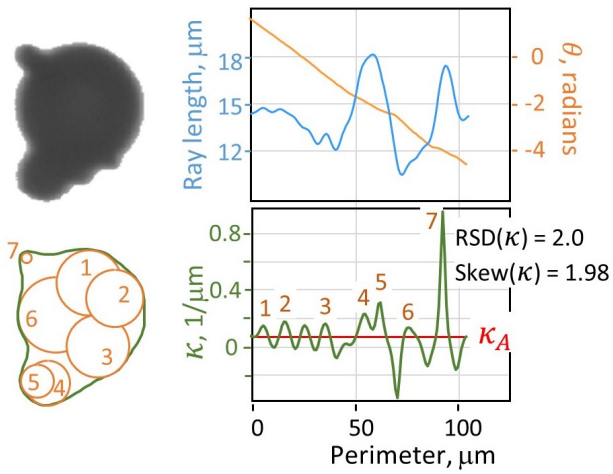

Figure B.7. The radius of curvature is a local quantity. A gas-atomized particle with local radii of curvature labeled and equivalent circles illustrated (1,2,3,4,5,6,7). Curvature and ROC values are shown in Table B.3.

In cartesian space, [116] shows that the curvature, κ, at a parameterized point t is equal to the cross product between the first and second derivatives of the function, where $'$ denotes differentiation with respect to t.

$$\kappa = s'(t) \times s''(t) = \begin{bmatrix} x'(t) \\ y'(t) \end{bmatrix} \times \begin{bmatrix} x''(t) \\ y''(t) \end{bmatrix} \tag{B.16}$$

And yields a reduced form, where ROC is the radius of curvature:

$$\kappa = \frac{1}{ROC} = \frac{x'(t)y''(t) - y'(t)x''(t)}{(x'(t)^2 + y'(t)^2)^{\frac{3}{2}}} \tag{B.17}$$

To be consistent with the parameterization of the particle in polar coordinates,

$$x(t) = R(t)cos(\theta(t)) \quad \text{and} \quad y(t) = R(t)sin(\theta(t)) \tag{B.18}$$

and applying the product rule and chain rule allows for the first and second derivatives of $x(t)$ and $y(t)$ to be found relative to the polar frame of reference:

$$\begin{aligned} y'(t) = \frac{d}{dt}(R(t))sin(\theta(t)) + \frac{d}{dt}(sin(\theta(t)))R(t) \\ = R'(t)sin(\theta(t)) + R(t)\theta'(t)cos(\theta(t)) \end{aligned} \tag{B.19}$$

$$\begin{aligned} x'(t) = \frac{d}{dt}(R(t))cos(\theta(t)) + \frac{d}{dt}(cos(\theta(t)))R(t) \\ = R'(t)cos(\theta(t)) - R(t)\theta'(t)sin(\theta(t)) \end{aligned} \tag{B.20}$$

$$\begin{aligned} y''(t) = R''(t)sin(\theta(t)) + 2R'(t)\theta'(t)cos(\theta(t)) \\ + R(t)(\theta''(t)cos(\theta(t)) - \theta'(t)^2 sin(\theta(t))) \end{aligned} \tag{B.21}$$

$$x''(t) = R''(t)cos(\theta(t)) - 2R'(t)\theta'(t)sin(\theta(t)) \\ - R(t)(\theta''(t)sin(\theta(t)) + \theta'(t)^2 cos(\theta(t))) \quad \text{(B.22)}$$

Substituting these expressions into the curvature formula yields the following reduced expressions for the curvature in the polar frame of reference:

$$x'(t)^2 + y'(t)^2 = R'(t)^2 + R(t)^2\theta'(t)^2 \quad \text{(B.23)}$$

$$x'(t)y''(t) - y'(t)x''(t) = \\ 2R'(t)^2\theta'(t) + R'(t)R(t)\theta''(t) - R''(t)R(t)\theta'(t) + R(t)^2\theta'(t)^3 \quad \text{(B.24)}$$

$$\kappa = \frac{2R'(t)^2\theta'(t) + R'(t)R(t)\theta''(t) - R''(t)R(t)\theta'(t) + R(t)^2\theta'(t)^3}{(R'(t)^2 + R(t)^2\theta'(t)^2)^{\frac{3}{2}}} \quad \text{(B.25)}$$

Parameterizing and representing the particle edge as a pair of Fourier series lends itself to analytical differentiation. Differentiating the expressions for $\tilde{R}(t)$ and $\tilde{\theta}(t)$ given in Equations B.8 and B.10 enables direct calculation of curvature from the Fourier series representation:

$$\tilde{R}'(t) = \sum_{\mathrm{i}=0}^{X_R} -2\pi \mathrm{i} n'_\mathrm{i} \hat{R}(n'_\mathrm{i}) \mathrm{e}^{-2\pi \mathrm{i} n'_\mathrm{i} t} \quad \text{(B.26)}$$

$$\tilde{R}''(t) = \sum_{\mathrm{i}=0}^{X_R} -(2\pi n'_\mathrm{i})^2 \hat{R}(n'_\mathrm{i}) \mathrm{e}^{-2\pi \mathrm{i} n'_\mathrm{i} t} \quad \text{(B.27)}$$

$$\tilde{\theta}'(t) = \frac{-2\pi}{P} + \sum_{\mathrm{i}=0}^{X_\theta} -2\pi \mathrm{i} m'_\mathrm{i} \hat{\theta}_p(m'_\mathrm{i}) \mathrm{e}^{-2\pi \mathrm{i} m'_\mathrm{i} t} \quad \text{(B.28)}$$

$$\tilde{\theta}''(t) = \sum_{\mathrm{i}=0}^{X_\theta} -(2\pi m'_\mathrm{i})^2 \hat{\theta}_p(m'_\mathrm{i}) \mathrm{e}^{-2\pi \mathrm{i} m'_\mathrm{i} t} \quad \text{(B.29)}$$

In this work, curvature was evaluated analytically for all GA and CMP particles.

For an idealized spherical particle, the radius is constant, $\theta(t)$ is linear, $\theta'(t)$ is constant, and $\theta''(t) = 0$. Equation B.25 simplifies to $\kappa = \frac{1}{R}$. At the other end of the spectrum, Particle C has multiple reentrant features and concave regions. Utilizing Equation B.25, a map of

contact curvature for the particle can be created as is shown in Figure B.4. The average contact curvature, κ_A, is equal to the reciprocal of the area equivalent radius. The contact curvature map is foundational to understanding the behavior of a particle in a flow field and its effect on the system as a whole. A contact curvature of close to 0 indicates a large ROC meaning the edge is nearly flat in that region. Positive curvature expresses convexity. Higher values of curvature suggest a smaller local radius of curvature, such as the satellite structures (1,2) on Particle A. The glued sphere approximation, or effective radius of contact, in high curvature regions is significantly smaller than the particle's area equivalent radius. A negative curvature denotes concavity, such as (2) on Particle C. Interactions between highly positive and negative regions of curvature could affect the ability of particles to move past each other in a flow field.

B.5 Curvature Distribution Analysis

The contact curvature map is an expedition around a particle's edge, chronicling the unique synergy between the harmonics that compose it. In this aspect, each particle has its own curvature distribution with a sequence that affects interactions with other objects, akin to an animate descriptor. For example, the gas atomized Particle B in Figure B.4 and the cut-milled particle shown in Figure B.5 have similar sizes, $x_A \approx 50\mu m$, and form factors, $FF \approx 0.8$; yet their curvature profiles are significantly different. While differences in AR and EFF highlight particle elongation and perimeter irregularity, curvature provides more insight in terms of archetypal descriptors: the GA particle being round, shaped like a droplet with satellite structures (1,2,3,4); the CMP particle being boxy, with flat faces and corners that are remnants of the cutting process used in its formation.

The contact curvature analysis vividly discriminates between GA and CMP powders. In Figure B.5, much of the cut-milled particle's curvature is close to 0 (indicating a flat surface), with high curvature convex peaks at the corners. In contrast, the gas-atomized particle in Figure B.4B has a curvature map that is more evenly distributed around the area equivalent radius of curvature, with the largest perturbations due to satellite structures, both concave and convex.

Per-particle contact curvature distributions can be summarized using statistical moments: mean ($\bar{\kappa} = \kappa_A$), standard deviation, and skew. For each particle, the relative standard deviation, κ_{RSD}, normalizes the standard deviation of contact curvature by the mean; it describes the relative breadth of the particle's curvature distribution. The skew of the curvature, κ_{skew} depicts the degree of each particle's curvature asymmetry, where σ is the standard deviation of the set of curvatures. A positive skew has an extended tail of convex curvature; a negative skew indicates a tail of concave curvature. For example, a shape comprising relatively flat sides with corners has a positive skew, e.g., Figure B.5, while a reentrant shape with deep concavity has a negative skew, as shown in Figure B.4C.

$$\kappa_{RSD} = \frac{1}{\kappa_A}\sqrt{\frac{\sum_{\mathrm{i}=0}^{N}(\kappa_{\mathrm{i}} - \kappa_A)}{N}} \tag{B.30}$$

$$\kappa_{skew} = \frac{\sum_{\mathrm{i}=0}^{N}(\kappa_{\mathrm{i}} - \kappa_A)^3}{(N-1)\sigma^3} \tag{B.31}$$

These statistical descriptors of individual particle curvature distributions can then be compared across populations of particles, i.e., distributions of distribution moments. Dimensionless curvature statistics augment the mean curvature obtained from the reciprocal of the area-equivalent radius. ăEach particle's summary statistics were weighted according to the ray length, providing more weight to the extremities that are more likely to be involved in the ensemble contact distribution.ă

Assessing the utility of curvature summary statistics as shape descriptors, a difference in curvature skews was observed between the GA and CMP samples, with the CMP particles having a noticeable positive mean skew relative to GA (Figure B.8).ă While both have broad secondary distributions comprising particles with negative skews, the principle modes of both samples have relatively narrow distributions. The GA particles were balanced between positive and negative skews with a principal mode having a mean of about zero; this fits a description of agglomerated features that can impart both positive and negative curvature.ă The CMP particles had an average positive skew consistent with milled-particle morphologies comprising relatively flat-sides with cut corners.ă The net difference is a shift of about 0.5 in the κ_{skew} distributions.

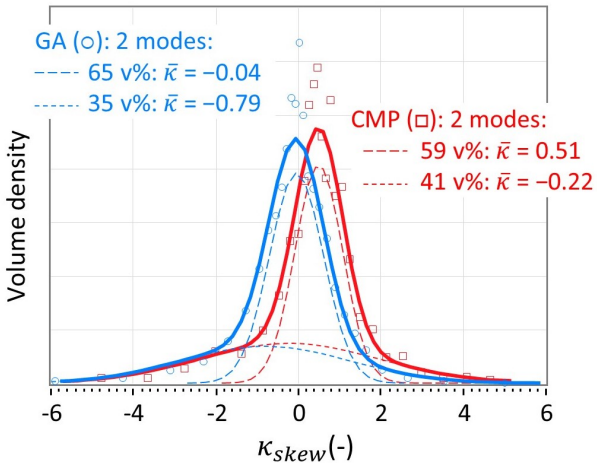

Figure B.8. Frequency distributions in κ_{skew} for gas atomized and milled LPBF powders.

Adding κ_{skew} and κ_{RSD} to the PCA elucidates their positioning within the space of shape factors. The augmented correlation matrix is shown in Table **??**. κ_{RSD} is a pseudo-member of the irregularity cluster, as it shows moderate correlations with $\hat{R}^*_{3:N}$ and EFF. κ_{RSD} is weakly coorelated with FF and is largely uncorrelated with AR and $\hat{R}^*_2$, suggesting that κ_{RSD} does not capture elongation. As a result, κ_{RSD} was not observed to be a significantly differentiating shape factor in comparison with AR and EFF when assessed over CMP and GA populations.

Table B.4. Correlation factors between shape factors and curvature statistical moments, estimated using the row-wise method. Clusters of correlated shape factors are indicated by color shading.

	κ_{skew}	κ_{RSD}	$\hat{R}^*_{3:N}$	EFF	FF	AR_{box}	$\hat{R}^*_2$
κ_{skew}	1.00	-0.31	-0.18	0.28	0.26	0.14	-0.23
κ_{RSD}	-0.31	1.00	0.63	-0.62	-0.55	-0.22	0.25
$\hat{R}^*_{3:N}$	-0.18	0.63	1.00	-0.90	-0.80	-0.34	0.39
EFF	0.28	-0.62	-0.90	1.00	0.93	0.45	-0.57
FF	0.26	-0.55	-0.80	0.93	1.00	0.72	-0.81
AR_{box}	0.14	-0.22	-0.34	0.45	0.72	1.00	-0.95
$\hat{R}^*_2$	-0.23	0.25	0.39	-0.57	-0.81	-0.95	1.00

On the other hand, κ_{skew} captured curvature progressions that were separate and distinct from the irregularity and elongation captured by EFF and AR. κ_{skew} is uncorrelated with all other shape factors, implying that κ_{skew} describes features that EFF and AR are not sensitive to. Comparing GA and CMP powders, κ_{skew} appears to reflect the powder method of formation and may tangibly affect performance in the end-use application. Including κ_{skew} in an expanded principal component analysis results in the emergence of a third principal component describing curvature, as is shown in Figure B.9.

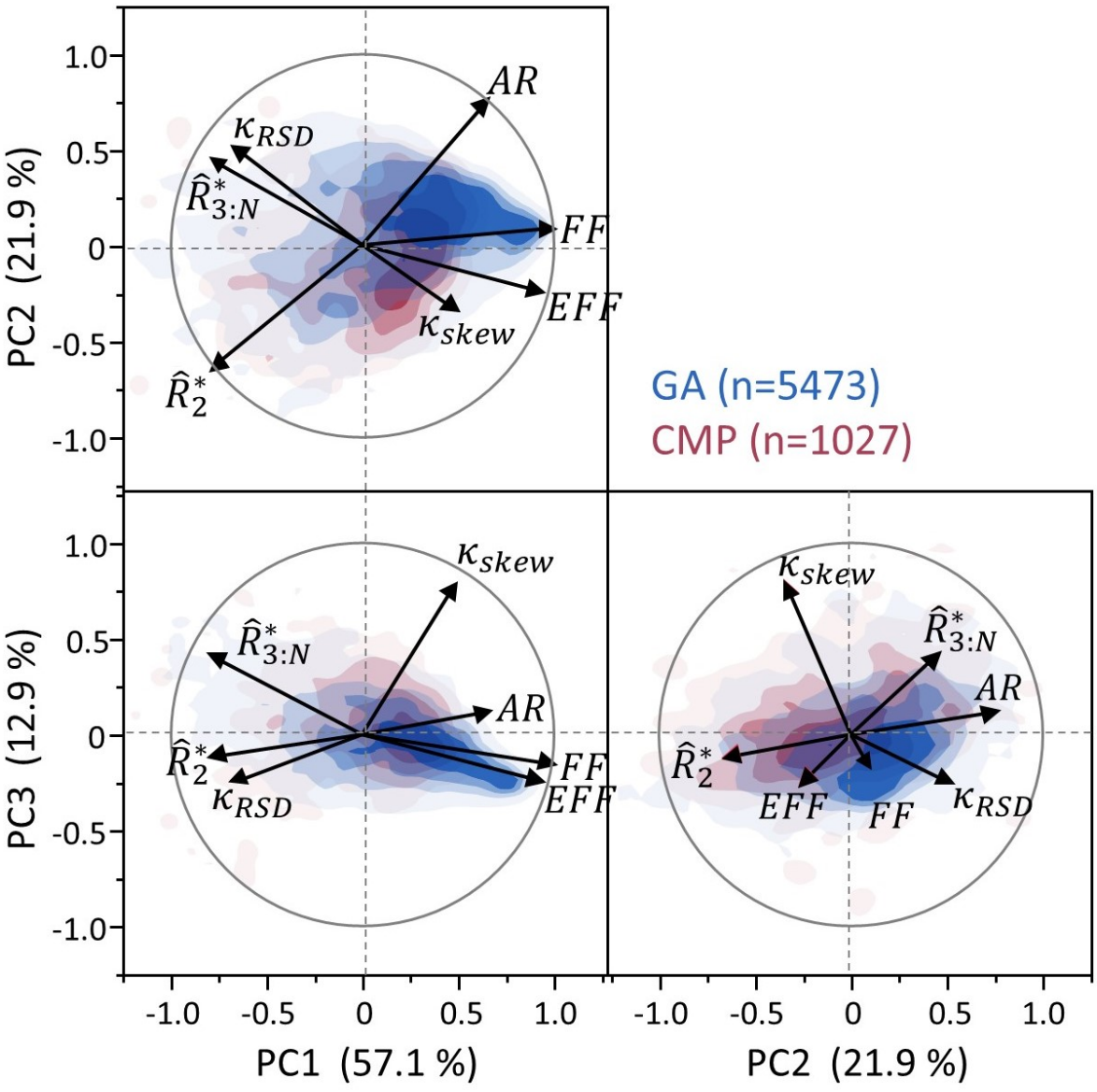

Figure B.9. Three-component principal component analysis of gas atomized (GA) and milled (MPW) additive manufacturing powders, account for distributions in contact curvature.

B.6 Conclusions and Perspective

Applications of additive manufacturing continue to grow in a variety of industries. The processing and product quality challenges associated with powder bed AM highlight the need for advancements in particulate science, engineering, and technologies. Characterization and specification of particle size and shape features is an important foundation needed to address those challenges, specifically powder spreading and packing which is paramount to throughput and part quality.

Dynamic image analysis has developed into a useful and routine tool for powder size and shape analyses. However, detailed shape analysis has been limited by ambiguity of the particle perimeter relative to thresholding and pixelation effects. The current work describes and implements a systematic approach to perimeter-dependent shape characterization over distributed data sets. The use of Fourier transforms for shape analysis was revisited, transforming pixelated perimeters into continuous functions. Fourier reconstruction with a subset of frequencies resulted in smoothed and continuous perimeters. Differentiation of continuous perimeters enabled the calculation of curvature at all points on the particle's edge, statistical characterization of curvature on a per-particle basis, and the comparison of those statistical descriptors across distributed populations.

Implementation of Fourier analysis and reconstruction was done using a parameterized approach, mapping both ray length and angle as a function of perimeter length. FFT analysis required each particle perimeter to be divided into equal-length segments. Segmentation criteria were scaled to particle size, i.e., pixel-scale resolution, and showed consistent results across the breadth of the particle size distribution. Parameterized FFT enabled analysis of complex particle shapes, including shapes having re-entrant features, and was compatible with curvature calculations.

The current work includes a case study of two metal powders, both suitable for LPBF additive manufacturing, and made using different production methods. The method of production affected particle size and shape. While there was overlap in the distributions, the samples were discernible based on several archetypal shape features. Principal component analysis revealed trends and clustering relations between ISO-defined and Fourier-derived

shape factors. Shape factors derived from the magnitudes of Fourier transforms were analogous to ISO-defined shape factors or modifications thereof. The 2nd mode of the Fourier series, $\hat{R}^*_2$, correlates with the aspect ratio; and the sum of higher-order modes, $\hat{R}^*_{(3:n}$, correlates with the elliptical form factor. Additionally, a curvature summary statistic, κ_{skew}, helps to differentiate shapes based on the predominance of convex and concave features.

More broadly, we anticipate that systemic and programmatic characterization of particle distributions using Fourier transforms and curvature analyses can better inform models requiring multi-body contact mechanics. Models are needed to describe ensemble behaviors including powder flow, packing, compaction, granulation, and dispersion of particles; all of which are critical for various industries including pharmaceuticals, chemicals, and materials engineering. Reg Davies contributed to these areas, pushing the boundaries of what was possible in particle technology, a legacy that we hope to continue through advances in the distributed characterization of powders.

B.7 Fourier Transform Background

The Fourier transform is a mathematical tool for representing single-valued and continuous periodic functions as the summation of an infinite series of trigonometric functions. This is done by breaking a convoluted waveform, $f(t)$ in Equation B.32, into individual frequencies and describing the degree to which each is present in the combined waveform[6]. The n-th harmonic refers to the waveform of frequency n.

$$f(t) = \frac{a_0}{2} + (\sum_{n=1}^{N} a_n cos(2\pi nt) + b_n \mathrm{i} sin(2\pi nt)) \tag{B.32}$$

Euler's formula, Equation B.33, allows this relationship to be rewritten as a sum of imaginary exponentials, as shown in Equation B.34.

$$\mathrm{e}^{\mathrm{i}t} = cos(t) + \mathrm{i} sin(t) \tag{B.33}$$

$$f(t) = \sum_{n=-\infty}^{\infty} C_n \mathrm{e}^{2\pi \mathrm{i} nt} \tag{B.34}$$

[6]↑In this formulation, $t \in [0, 1]$. Replacing t with t/t_{max} means that t can have an arbitrary upper bound.

Fourier coefficients (C_n) are complex numbers of the form $a+b\mathrm{i}$. Positive and negative frequencies have symmetric conjugates and identical magnitudes. When the function is reconstructed as the summation of waveforms, the Fourier coefficients C_n determine the contribution of each harmonic to the overall shape. The real and imaginary components of the Fourier coefficient scale the amplitude of the cosine wave and sine wave respectively. Sine and cosine waves of the same harmonic are orthogonal to each other, meaning the magnitude of the real and imaginary components of the Fourier coefficient determines the amplitude of the harmonic and the relative difference between them determines the orientation of the harmonic.

Following a derivation in [117] and [118], to solve for the Fourier coefficients, Equation B.34 is modified by multiplying both sides by a factor of $\mathrm{e}^{-2\pi\mathrm{i}kt}$ and rearranging to isolate individual Fourier coefficients shown as the k-th Fourier coefficient C_k:

$$C_k = \mathrm{e}^{-2\pi\mathrm{i}kt} f(t) - \sum_{\substack{n=-\infty \\ n\neq k}}^{\infty} C_n \mathrm{e}^{-2\pi\mathrm{i}kt} \mathrm{e}^{2\pi\mathrm{i}nt} = \mathrm{e}^{-2\pi\mathrm{i}kt} f(t) - \sum_{\substack{n=-\infty \\ n\neq k}}^{\infty} C_n \mathrm{e}^{2\pi\mathrm{i}(n-k)t} \tag{B.35}$$

Integrating both sides from 0 to 1 with respect to t simplifies the expression, leveraging the identity shown in Equation B.37 (for all $n \neq k$). This leaves Equation B.38 as an exact expression for C_k, given $f(t)$ for all real k values in $[-\infty, \infty]$. The equation for the Fourier transform is shown in Equation B.39, where the value of the Fourier transform for any mode (n) is a complex number. This is known as the frequency domain representation of the function, as it describes the prominence of each harmonic in the original function.

$$\int_0^1 C_k dt = \int_0^1 (\mathrm{e}^{-2\pi\mathrm{i}kt} f(t) - \sum_{\substack{n=-\infty \\ n\neq k}}^{\infty} C_n \mathrm{e}^{2\pi\mathrm{i}(n-k)t}) dt \tag{B.36}$$

$$\int_0^1 \mathrm{e}^{2\pi\mathrm{i}(n-k)t} dt = \frac{\mathrm{e}^{2\pi\mathrm{i}(n-k)t}}{2\pi\mathrm{i}(n-k)t}\Big|_{t=0}^{t=1} = 0 \tag{B.37}$$

$$C_k = \int_0^1 (\mathrm{e}^{-2\pi\mathrm{i}kt} f(t)) dt \tag{B.38}$$

$$\hat{f}(n) = \int_0^1 (\mathrm{e}^{-2\pi\mathrm{i}nt} f(t)) dt \tag{B.39}$$

The inverse Fourier transform allows the time domain function to be reconstructed by summing the contributions of the individual Fourier modes, shown in Equation B.40. A constrained form of this technique is leveraged in the particle reconstruction procedure.

$$f(t) = \sum_{n=-\infty}^{\infty} \hat{f}(n) \mathrm{e}^{-2\pi i n t} \tag{B.40}$$

The preceding derivation assumes that $f(t)$ is continuous, however, images of particles are composed of discrete pixels. The Nyquist-Shannon sampling theorem states that a function can be reconstructed completely from a series of points spaced $1/2W$ units apart if it contains no frequencies greater than w units^{-1}[119]. Aliasing refers to distortion in the measured signal due to the sampling rate being too low to accurately represent high-frequency modes[105]. The Nyquist criterion affirms that the sampling rate must be at least twice the maximum frequency to avoid aliasing [105]. These results lead to a necessary truncation of high-frequency modes from the Fourier series representations of a digital signal.

The fast Fourier transform (FFT) is an algorithm designed to perform the Fourier transform on discrete datasets, such as images of particles. There are numerous implementations, leveraged in this work are the NumPy [120, 121] and National Instruments LabVIEW [75] libraries. The LabVIEW implementation was used for large dataset processing while NumPy was used for developing and testing the particle reconstruction algorithms. The NumPy implementation of the FFT and inverse FFT is shown in Equations B.41 and B.42, where N is the number of measurement points. Both implementations produced equivalent results.

$$\hat{f}(n) = \mathcal{FFT}(f(t)) = \sum_{m=0}^{N-1} f(t_m) \exp\{\frac{-2\pi i t_m n}{N}\} \tag{B.41}$$

$$f(t_m) = \mathcal{IFFT}(\hat{f}(n)) = \frac{1}{N} \sum_{n=0}^{N-1} \hat{f}(n) \exp\{\frac{2\pi i t_m n}{N}\} \tag{B.42}$$

B.8 Pixelation

The raw data obtained from image analysis comprises 8-bit grayscale (0-255; 0=black, 255=white) digital images of individual particles flowing through an imaging cell (InFlow, JM

Canty, Lockport, NY). Pixels were calibrated to 0.334 $\frac{\mu m}{pixel}$ length. Images were thresholded at a grayscale value of 170. Challenges with perimeter uncertainty in relation to pixelation and robustness of shape features have been discussed in the literature and were addressed in an earlier publication [5]. The following describes the methodology for extracting perimeter data from pixelated images, as implemented in LabVIEW (National Instruments, Austin, TX).

On one hand, Fourier reconstruction overcomes pixelation by providing a continuous perimeter trace; on the other hand, the initial Fourier transform requires a parameterized description of the pixelated perimeter, wherein both ray length and angle are functionally mapped to the perimeter trace, and the trace is numerically divided in equal increments. The current procedure includes pixelation, interpolation, FFT fitting/smoothing of the perimeter, and local curvature calculation using derivatives of the parameterized FFT functions.

Perimeter edges were identified on a per-pixel basis as threshold transition along 1, 2, or 3 contiguous edges, and placing a segment endpoint at the midpoint of each edge. Depending on the edge pattern, incremental segments have a length of either 1 pixel or $\sqrt{2}/2$ pixels and must be either horizontal, vertical, or diagonal on the pixelated Cartesian plane. Segments were connected sequentially in a clockwise trace (Figure B.10). Note that the area enclosed by the pixelated trace is equal to the sum minus 1/2 pixel area.

Parameter	**Description**
N	Number of equally-spaced interpolation points
A_x	Particle area, in number of pixels
$m = 1.4$	Exponent in the empirical equation
$N_{\min} = 34$	Minimum number of interpolation points
$N_{\max} = 180$	Maximum number of interpolation points

Table B.5. Summary of parameters for the updated interpolation points function.

Interpolation is scale-dependent. For smaller particles having coarse-grained shapes (i.e., less than about 100 pixels/particle), interpolation is done with more increments than the pixels on the perimeter. This enables more continuous smoothing in the FFT fitting step. On the other hand, fine-grained particle shapes (i.e., greater than about 1000 pixels/particle) are smoothed by interpolating with increments larger than about two pixel-lengths. This

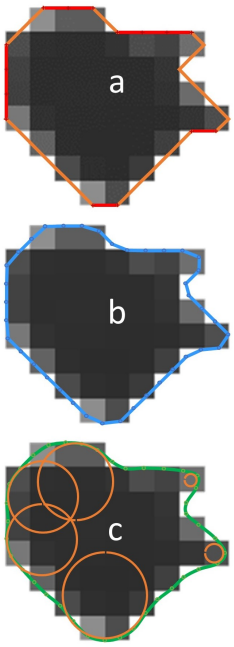

Figure B.10. Pixelation procedure of a particle comprised of 47 pixels: a) initial perimeter pixelation using 36 contiguous midpoints of pixel edges (red segment = 1 pixel; orange segments = $\sqrt{2}/2$ pixels; b) perimeter interpolation divided into 38 equal increments; c) FFT fitting with selected curvatures (orange circles).

Table B.6. Effect of coarse-graining (Figure B.11) on computed shape factors. Form factors (FF and EFF) are based on FFT-smoothed perimeters; curvature (κ) is based on differentiation with respect to the perimeter.

CG area	A_{pxl}	P_{pxl}	N_{interp}	AR_{ISO}	AR_{box}	FF	EFF	RSD(κ)	skew(κ)
a) 1x	7954.5	374	133	0.78	0.796	0.715	0.729	3.91	-3.29
b) 9x	886.5	124	66	0.766	0.776	0.719	0.736	3.77	-2.71
c) 169x	46.5	28	38	0.7	0.89	0.771	0.774	2.70	1.75

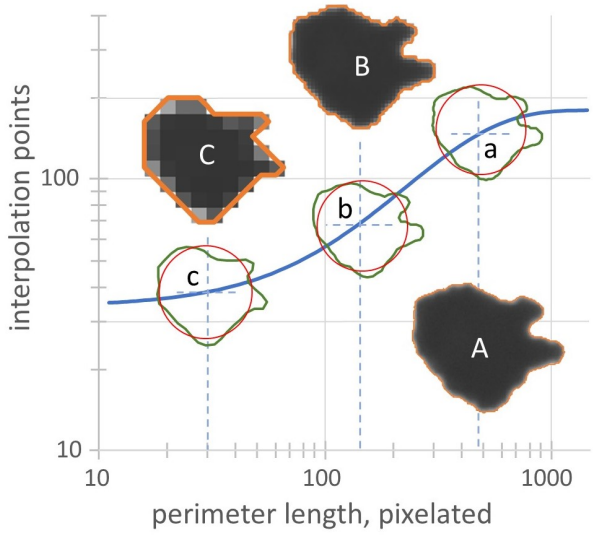

Figure B.11. Scale-dependent interpolation based on pixelation scale (blue curve, defined by equation B.1). Illustrations show the effect of coarse-graining pixelated images with initial pixelation trace in orange: A) as-measured particle; B) 9x area coarse-graining; C) 169x area coarse-graining. Small-case overlays are the results of FFT fitting (green perimeter outline) with superposed area-equivalent circles (red). Details are shown in Table B.6.

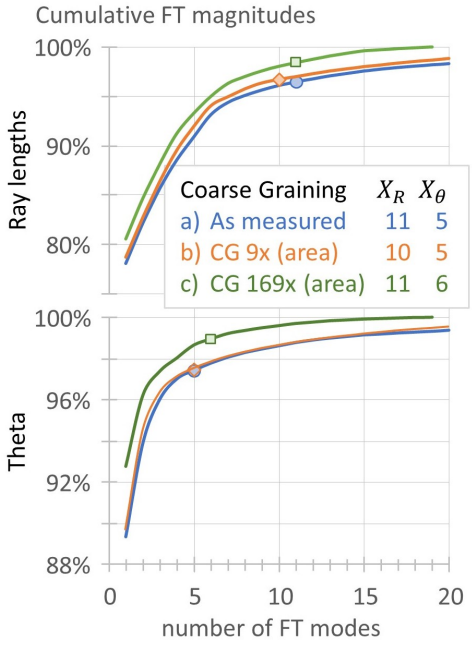

Figure B.12. Example of thresholding used to select Fourier transform modes used in curvature calculations. Three cases (a, b, c) correspond to the coarse-grained images shown in Figure B.10.

scale-dependent smoothing is shown graphically in Figure B.11, using a gas-atomized particle that was coarse-grained to show the range of scale effects; the same coarse-grained particle image is shown in Figure B.10.C.

$$N = N_{\min} + (N_{\max} - N_{\min}) \cdot \left(1 - \exp\left(-\left(\frac{A_x}{2N_{\max}}\right)^m\right)\right) \tag{B.43}$$

Interpolated perimeters, i.e., comprising segments having equal pixelated length increments, δt, were used to create parameterized functions, $R(t)$ and $\theta(t)$, for FFT analysis. Smoothed perimeters were then reconstructed using the inverse transform with n largest FFT frequencies, where n was evaluated in relation to thresholding criteria whereby modes were selected from lists sorted by mode magnitude normalized to total cumulative magnitude at an incremental threshold of 0.4%, as illustrated in Figure B.11. Thresholding was done independently for ray length and theta modes. In addition, high-frequency modes, defined as having a frequency greater than the number of modes plus 7 were eliminated; excessively high-frequency modes are associated with the uncertainty of edge detection, e.g., caused by poor focus, and contribute to noise in curvature calculations.